

THE UNIVERSITY OF NOTTINGHAM  
SIR PETER MANSFIELD IMAGING CENTRE  
SCHOOL OF PHYSICS AND ASTRONOMY

---

**Developing Techniques for Quantitative Renal Magnetic  
Resonance Imaging**

---

*Author:* Alexander James DANIEL MSci      *Supervisor:* Prof. Susan FRANCIS

6<sup>th</sup> March, 2021



Thesis submitted to the University of Nottingham for the degree of Doctor of Philosophy

It's very hard to talk quantum using a language originally designed to tell other monkeys where the ripe fruit is.

---

Terry Pratchett, *Night Watch*

## **Abstract**

Science will happen, but this bit can be read by muggles on ‘tinterweb.

# Contents

<b>Abstract</b>	ii
<b>Contents</b>	iii
<b>Acknowledgments</b>	viii
<b>Abbreviations</b>	ix
<b>1 Introduction</b>	1
1.1 Imaging in the Clinic . . . . .	1
1.2 Clinical Motivation . . . . .	2
1.3 Thesis Overview . . . . .	6
1.4 References . . . . .	8
<b>2 Principles of Nuclear Magnetic Resonance Imaging</b>	11
2.1 Source of the NMR Signal . . . . .	13
2.1.1 Nuclear Spin . . . . .	13
2.1.2 Application of an External Magnetic Field . . . . .	14
2.1.3 Precession . . . . .	15
2.1.4 Resonance . . . . .	16
2.2 Relaxation and Contrast Mechanisms . . . . .	18
2.2.1 Longitudinal Relaxation ( $T_1$ ) . . . . .	18
2.2.2 Transverse Relaxation ( $T_2$ and $T_2^*$ ) . . . . .	20
2.2.3 Dipole-Dipole Interactions . . . . .	25
2.2.4 Diffusion Imaging . . . . .	27
2.2.5 Optimisation of Tissue Contrast . . . . .	29

2.3	Forming an Image . . . . .	31
2.3.1	Signal Localisation . . . . .	31
2.3.2	Image Acquisition Acceleration . . . . .	38
2.3.3	Image Acquisition Schemes . . . . .	40
2.4	Conclusion . . . . .	46
2.5	References . . . . .	47
<b>3</b>	<b>Assessment of Renal <math>T_2</math> Mapping Methods</b>	<b>48</b>
3.1	Introduction . . . . .	50
3.2	Methods . . . . .	52
3.2.1	Data Acquisition . . . . .	52
3.2.2	Post Processing . . . . .	59
3.2.3	Assessment of Data . . . . .	60
3.3	Results . . . . .	66
3.3.1	Fitting Methods . . . . .	66
3.3.2	Phantom Verification . . . . .	68
3.3.3	In-Vivo . . . . .	73
3.4	Discussion . . . . .	77
3.5	Conclusion . . . . .	82
3.6	Acknowledgements . . . . .	82
3.7	References . . . . .	83
<b>4</b>	<b>Quantitative Methods to Measure Renal Oxygenation</b>	<b>89</b>
4.1	Introduction . . . . .	91
4.2	Methods . . . . .	94
4.2.1	Susceptibility-Based Oximetry . . . . .	94
4.2.2	$T_2$ Relaxation Under Spin Tagging . . . . .	96
4.2.3	Inducing Changes in Oxygenation of Blood in the Renal Vein . . . . .	102
4.3	Results and Discussion . . . . .	104
4.3.1	Susceptibility-Based Oximetry . . . . .	104
4.3.2	$T_2$ Relaxation Under Spin Tagging . . . . .	106
4.4	Conclusions and Future Work . . . . .	114

4.5	Acknowledgements . . . . .	114
4.6	References . . . . .	115
<b>5</b>	<b>Automated Segmentation of Kidneys using Machine Learning</b>	<b>120</b>
5.1	Introduction . . . . .	122
5.2	Neural Networks for Image Segmentation . . . . .	125
5.2.1	Artificial Neural Networks . . . . .	125
5.2.2	Convolutional Neural Networks . . . . .	128
5.3	Methods . . . . .	131
5.3.1	MRI Data Acquisition . . . . .	131
5.3.2	Manual Segmentation . . . . .	132
5.3.3	Automated Segmentation Using a CNN Architecture .	132
5.3.4	Statistical Analysis . . . . .	135
5.4	Results . . . . .	137
5.4.1	Characteristics of the Training Cohort . . . . .	137
5.4.2	Reducing Acquisition Time . . . . .	138
5.4.3	Accuracy of Manual Segmentation . . . . .	139
5.4.4	Network Testing . . . . .	142
5.5	Discussion . . . . .	149
5.5.1	Evaluation of Methodology . . . . .	150
5.5.2	Future Directions . . . . .	152
5.6	Conclusions . . . . .	155
5.7	Acknowledgements . . . . .	155
5.8	References . . . . .	156
<b>6</b>	<b>Ex-Vivo Renal MRI</b>	<b>162</b>
6.1	Introduction . . . . .	163
6.1.1	Validation of Multiparametric MRI via a Nephrectomy Model . . . . .	163
6.1.2	Assessment of Allograft Viability . . . . .	166
6.1.3	Ex-Vivo Protocol Aims . . . . .	166
6.2	MRI Protocol Development . . . . .	167
6.2.1	Anatomical Scans . . . . .	169

6.2.2	$T_1$ Mapping . . . . .	170
6.2.3	$T_2$ Mapping . . . . .	173
6.2.4	$T_2^*$ Mapping . . . . .	175
6.2.5	Apparent Diffusion Coefficient Mapping . . . . .	178
6.2.6	Diffusion Tensor Imaging . . . . .	182
6.3	Monitoring Changes in MR Parameters Post Fixation . . . . .	191
6.4	Layer Based Analysis of Renal Data . . . . .	193
6.5	Correlating MRI Measures with Histopathology in Aged Kidneys . . . . .	194
6.6	Conclusion . . . . .	195
6.7	Acknowledgements . . . . .	195
6.8	References . . . . .	196
<b>7</b>	<b>Conclusion</b>	<b>202</b>
<b>A</b>	<b>Tractography Pipeline</b>	<b>203</b>

# **Todo list**

■ Make sure these are in the correct order . . . . .	6
■ Due to stimulate echoes? . . . . .	57
■ Would a 2D example of applying a Gaussian blur to an image be helpful here too? . . . . .	63
Figure: Individual b-values . . . . .	181

# Acknowledgements

Finally thank you to covid-19 for removing enough distractions to motivate me to write this thesis.

# Abbreviations

<b>ADC</b>	Apparent Diffusion Coefficient
<b>ADPKD</b>	Autosomal Dominant Polycystic Kidney Disease
<b>AKI</b>	Acute Kidney Injury
<b>ANN</b>	Artificial Neural Network
<b>ASL</b>	Arterial Spin Labelling
<b>BOLD</b>	Blood Oxygen Level Dependent
<b>CBF</b>	Cerebral Blood Flow
<b>CKD</b>	Chronic Kidney Disease
<b>CMRO<sub>2</sub></b>	Cerebral Metabolic Rate of Oxygen
<b>CNN</b>	Convolutional Neural Network
<b>CoV</b>	Coefficient of Variation
<b>CPMG</b>	Carr-Purcell-Meiboom-Gill
<b>CSF</b>	Cerebrospinal Fluid
<b>CT</b>	Computed Tomography

<b>DTI</b>	Diffusion Tensor Imaging
<b>DWI</b>	Diffusion Weighted Imaging
<b>eGFR</b>	Estimated Glomerular Filtration Rate
<b>EPI</b>	Echo Planar Imaging
<b>eTE</b>	Effective Echo Time
<b>ETL</b>	Echo Train Length
<b>EuDX</b>	Euler Delta Crossings
<b>FA</b>	Fractional Anisotropy
<b>FAIR</b>	Flow-sensitive Alternating Inversion Recovery
<b>FFE</b>	Fast Field Echo
<b>FID</b>	Free Induction Decay
<b>FOV</b>	Field Of View
<b>FSE</b>	Fast Spin Echo
<b>FSL</b>	fMRI Software Library
<b>FWHM</b>	Full Width Half Maximum
<b>GE</b>	Gradient Echo
<b>GFR</b>	Glomerular Filtration Rate
<b>GPU</b>	Graphical Processing Unit
<b>GraSE</b>	Gradient Spin Echo
<b>GUI</b>	Graphical User Interface

<b>H and E</b>	Haematoxylin and Eosin
<b>HASTE</b>	Half-Fourier Single-shot Turbo spin Echo
<b>HC</b>	Healthy Control
<b>ICC</b>	Intraclass Correlation
<b>ISMRM</b>	International Society of Magnetic Resonance in Medicine
<b>IVIM</b>	Intravoxel Incoherent Motion
<b>LSTM</b>	Long Short-Term Memory
<b>MD</b>	Mean Diffusivity
<b>ME-TSE</b>	Multi-Echo Turbo Spin Echo
<b>MRE</b>	Mean Relativel Error
<b>MRI</b>	Magnetic Resonance Imaging
<b>NBF</b>	Neutral Buffered Formalin
<b>NHS</b>	National Health Service
<b>NMR</b>	Nuclear Magnetic Resonance
<b>ODF</b>	Orientation Distribution Fuction
<b>PBS</b>	Phosphate-buffered Saline
<b>PC</b>	Phase Contrast
<b>PET</b>	Positron Emission Tomography
<b>PLD</b>	Post Label Delay
<b>PSD</b>	Pulse Sequence Diagram

<b>PSF</b>	Point Spread Function
<b>PRELUDE</b> Phase Region Expanding Labeller for Unwrapping Discrete Estimates	
<b>QASPER</b>	Quantitative Arterial Spin Labelling Perfusion Reference
<b>QSM</b>	Quantitative Susceptibility Mapping
<b>RARE</b>	Rapid Acquisition with Relaxation Enhancement
<b>RBF</b>	Renal Blood Flow
<b>RNN</b>	Recursive Neural Network
<b>ReLU</b>	Rectified Linear Unit
<b>RF</b>	Radio Frequency
<b>RMRO<sub>2</sub></b>	Renal Metabolic Rate of Oxygen
<b>ROI</b>	Region Of Interest
<b>SAR</b>	Specific Absorption Rate
<b>SBO</b>	Susceptibility Based Oximetry
<b>SD</b>	Standard Deviation
<b>SE</b>	Spin Echo
<b>SENSE</b>	Sensitivity Encoding
<b>SNR</b>	Signal to Noise Ratio
<b>SPMIC</b>	Sir Peter Mansfield Imaging Centre
<b>TE</b>	Echo Time

<b>TFE</b>	Turbo Field Echo
<b>TI</b>	Inversion Time
<b>TILT</b>	Transfer Insensitive Labelling Technique
<b>TKV</b>	Total Kidney Volume
<b>TR</b>	Repetition Time
<b>TRUST</b>	$T_2$ Relaxation Under Spin Tagging
<b>TSE</b>	Turbo Spin Echo
<b>UKAT</b>	United Kingdom Renal Imaging Network (UKRIN) Kidney Analysis Toolbox
<b>UKKW</b>	United Kingdom Kidney Week
<b>UKRIN</b>	United Kingdom Renal Imaging Network
<b>WET</b>	Water suppression Enhanced through $T_1$ effects

# Chapter 1

## Introduction

### 1.1 Imaging in the Clinic

From April 2019 to March 2020, the United Kingdom's National Health Service (NHS) performed 45 million medical imaging procedures, of these 4 million were Magnetic Resonance Imaging (MRI) [1]. This technique can be used to produce high resolution volumetric images of the body with exquisite soft tissue contrast. Unlike other modalities, such as Computed Tomography (CT) and Positron Emission Tomography (PET), MRI uses non-ionising radiation, making it more suitable for longitudinal analysis of patient progression and research involving healthy volunteers.

The superior soft tissue contrast of MRI compared to CT meant it first found widespread clinical adoption in the field of neuroimaging. Here MRI has been used for diagnosis of neurological disorders, monitoring treatment progression and research into cognition. Many of the techniques honed in the brain, can be applied to the abdomen, where similar tissue properties can exploit the same techniques; albeit in a somewhat more challenging environment due to respiratory motion and a more inhomogeneous tissue structure. The kidneys are ideally suited to this translation as they have similar tissue properties to the brain and are highly dynamic organs.

## 1.2. Clinical Motivation

---

In addition to the acquisition of basic structural images, MRI can be used to collect quantitative information about the tissues being imaged. In this situation the numerical voxel values have physical significance, rather than simply representing signal intensity in arbitrary units [2]. Using quantitative MRI properties such as an organs oxygen consumption [3], perfusion [4], stiffness [5] and temperature [6] can be measured. Although many quantitative MRI techniques have been developed for the kidneys, there is still many methods where development, translation from the brain or standardisation with the wider renal community would be highly desirable.

## 1.2 Clinical Motivation

The kidneys are two bean shaped organs found in the abdomen, just below the rib cage, symmetrical about the spine, Figure 1.1. They participate in the control of bodily fluids by regulating the balance of electrolytes, excreting waste product of metabolism and excess water from blood into urine [7].

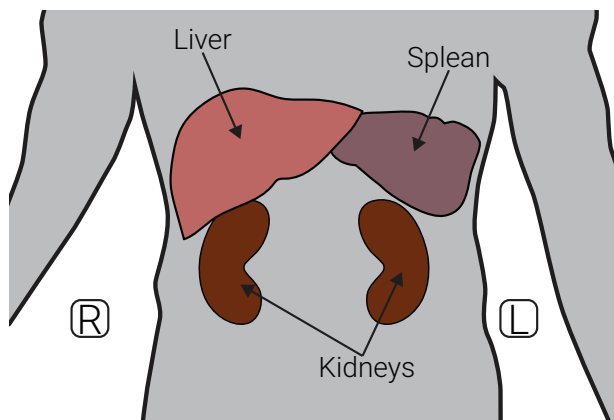


Figure 1.1: Lower abdominal organs.

Kidneys are made up of units called nephrons, Figure 1.2, each of which contains a renal corpuscle and a tubule. The renal corpuscle itself is made up of a glomerulus and a Bowman capsule. The glomerulus is a cluster of capillaries that allow wastes and fluid to pass out of the blood stream into the Bowman capsule, while larger structures such as blood cells and proteins

## 1.2. Clinical Motivation

---

remain in the blood. The substances that passed through the glomerulus are moved to the tubules, each of which has blood vessels running alongside; these vessels reabsorb many of the important components of the blood such as the majority of the water, minerals and nutrients. The remaining fluids and waste in the tubules are collected in the ureter and removed from the body [8].



Figure 1.2: A schematic of the anatomy of a nephron.

Tissue in the kidney is separated into renal cortex, the outer portion of the kidney and renal medulla, the inner portion. The cortex contains the corpuscles with the tubules passing from the cortex to the medulla. Medullary tissue is compartmentalised into renal pyramids. Blood is supplied to the kidney via the renal artery, this branches into smaller vessels until it reaches the glomeruli then flows out via the renal vein. An overview of the gross anatomy of the kidney is shown in Figure 1.3.

## 1.2. Clinical Motivation

---



Figure 1.3: The gross anatomy of the kidney.

Due to their vital function in the body and the toxins they encounter as they perform their role, the kidneys are susceptible to problems. Chronic Kidney Disease (CKD) is the progressive destruction of the kidneys and therefore decrease in renal function. More quantitatively, CKD can be assessed clinically by Glomerular Filtration Rate (GFR), the rate at which fluid is filtered through the kidneys, with a value below  $60 \text{ ml/min}/1.73\text{m}^2$  of body surface area being diagnostic or the presence of albumin, the main protein in blood plasma, in the patients urine [9–11]. Common causes of CKD are high blood pressure and diabetes as these damage the nephrons with high blood pressure also posing a risk to the blood vessels within the kidney. Renal tissue is highly vascularised and as such, the risks associated with high blood pressure are especially prevalent in the kidneys. An estimated 5–11% of the global population suffer from CKD [12–16] making it a significant public health concern. Late referral of renal disorders results in an increase in mortality rate and treatment costs [17–19]. Given that in 2013/2014 renal services cost the NHS £586 million [20] there are clear health and economic advantages to an early diagnosis and improved treatment of CKD. This can either be achieved via directly aiding diagnosis i.e. developing tools used on to assess patients condition and tailor treatment, or via improving understanding of CKD leading

## 1.2. Clinical Motivation

---

to an earlier, more accurate diagnosis using existing techniques and thus more personalised medicine.

The current methods available to study CKD are not ideal for a variety of reasons. Histological samples are the gold standard for studying renal tissue however collecting them is an invasive process and as such they are not suitable for monitoring the progress of a patient's condition on a regular basis. This coupled with the fact that a small sample is not representative of the entirety of both kidneys means that this method has large drawbacks. Ultrasound can be used to gather structural information about the kidneys non-invasively, however, it suffers from low spatial resolution and the images being difficult to interpret [21]. The most common method of diagnosis is to estimate GFR from the creatinine content in a blood sample however this measure does not allow for the individual assessment of each kidney and is an indirect measure of kidney tissue damage.

MRI is an ideal modality for the study of kidney disease due to its non-ionising, non-invasive and quantitative nature. A current research interest at the Sir Peter Mansfield Imaging Centre (SPMIC) is the use of a multi-parametric quantitative renal MRI protocol to assess and predict CKD [22, 23]. This protocol is used to measure multiple quantitative properties of the kidneys with relative increases/decreases between measurements functioning as biomarkers and therefore indications of CKD progression. The implementation of new quantitative renal imaging methods can improve this protocol, thus increasing its clinical application. In addition to the CKD paradigm, we wish to apply these methods ex-vivo, both to allow a more direct comparison with current gold standards, such as histopathology, and to aid with assessment of renal allograft viability.

## 1.3 Thesis Overview

**Chapter 2** provides the theoretical framework of Nuclear Magnetic Resonance (NMR) and MRI. A detailed description is given of the origin of the measured signal, processes that give rise to contrast between tissues and the methods of image formation.

**Chapter 3** explores  $T_2$  mapping within the kidneys. There is little consensus as to which method should be used within the kidneys [24], thus leading to inconsistent values quoted between studies [25]. Here multiple methods from the literature are compared assessing their quantitative accuracy and image quality in phantoms before five subjects are scanned to assess the methods in-vivo.

**Chapter 4** aims to translate methods for measuring blood oxygenation from vessels in the brain to use within the kidneys. Focusing on Susceptibility Based Oximetry (SBO) [26] and  $T_2$  Relaxation Under Spin Tagging (TRUST) [27] this chapter optimises the methods for use in the abdomen, verifying the modifications in the brain, then carries out an oxygen challenge in-vivo to measure changes in oxygen saturation within the renal vein.

**Chapter 5** describes the development of a fully automated method to segment the kidneys from MRI data. Defining renal masks is an important, yet time consuming, aspect of many studies. The masks can be used to calculate Total Kidney Volume (TKV) or to inform downstream processing. Here a Convolutional Neural Network (CNN) is developed to segment the kidneys from  $T_2$  weighted Half-Fourier Single-shot Turbo spin Echo (HASTE) images. Software is developed to provide an executable that allows anyone to segment the kidneys in a few seconds on regular office hardware.

**Chapter 6** develops methods for scanning kidneys ex-vivo. The clinical gold standard for diagnosis of renal pathologies is biopsy followed by histolo-

Make  
sure  
these  
are  
in  
the  
cor-  
rect  
or-  
der

### **1.3. Thesis Overview**

---

gical analysis. Comparison between this gold standard and recently developed quantitative MRI techniques is vital for clinical translation. Here a pipeline for multi-parametric imaging of the same kidney in-vivo, ex-vivo followed by histology is developed.

**Chapter 7** concludes the thesis, highlighting key results and their current applications. It also provides an overview as to future research directions and how the methods developed could be applied to new paradigms or expanded upon.

## 1.4 References

1. *Diagnostic Imaging Dataset Annual Statistical Release 2019/20* <https://www.england.nhs.uk/statistics/statistical-work-areas/diagnostic-imaging-dataset/diagnostic-imaging-dataset-2019-20-data/> (2021).
2. Tofts, P. *Quantitative MRI of the Brain: Measuring Changes Caused by Disease* 688 pp. Google Books: RbFrAAAAMAAJ (Wiley, 2003).
3. Zhang, J., Liu, T., Gupta, A., Spincemaille, P., Nguyen, T. D. & Wang, Y. Quantitative Mapping of Cerebral Metabolic Rate of Oxygen (CMRO<sub>2</sub>) Using Quantitative Susceptibility Mapping (QSM). *Magnetic Resonance in Medicine* **74**, 945–952 (1st Oct. 2015).
4. Karger, N., Biederer, J., Lüsse, S., Grimm, J., Steffens, J. .-.C., Heller, M. & Glüer, C. .-.C. Quantitation of Renal Perfusion Using Arterial Spin Labeling with FAIR-UFLARE. *Magnetic Resonance Imaging* **18**, 641–647 (1st July 2000).
5. Mariappan, Y. K., Glaser, K. J. & Ehman, R. L. MAGNETIC RESONANCE ELASTOGRAPHY: A REVIEW. *Clinical anatomy (New York, N.Y.)* **23**, 497–511 (July 2010).
6. Yuan, J., Mei, C.-S., Panych, L. P., McDannold, N. J. & Madore, B. Towards Fast and Accurate Temperature Mapping with Proton Resonance Frequency-Based MR Thermometry. *Quantitative Imaging in Medicine and Surgery* **2**, 212–232 (Mar. 2012).
7. Lote, C. J. *Principles of Renal Physiology* 255 pp. Google Books: at6LBQAAQBAJ (Springer Science & Business Media, 6th Dec. 2012).
8. Hall, J. E. *Guyton and Hall Textbook of Medical Physiology* 1171 pp. Google Books: 3sWNCgAAQBAJ (Elsevier Health Sciences, 20th May 2015).
9. Stevens, L. A., Coresh, J., Greene, T. & Levey, A. S. Assessing Kidney Function — Measured and Estimated Glomerular Filtration Rate. *New England Journal of Medicine* **354**, 2473–2483 (8th June 2006).
10. Farrugia, A. Albumin Usage in Clinical Medicine: Tradition or Therapeutic? *Transfusion Medicine Reviews* **24**, 53–63 (1st Jan. 2010).

#### 1.4. References

---

11. Pruijm, M., Milani, B. & Burnier, M. Blood Oxygenation Level-Dependent MRI to Assess Renal Oxygenation in Renal Diseases: Progresses and Challenges. *Frontiers in Physiology* **7**, doi:10.3389/fphys.2016.00667. pmid: 28105019 (5th Jan. 2017).
12. Coresh, J., Astor, B. C., Greene, T., Eknayan, G. & Levey, A. S. Prevalence of Chronic Kidney Disease and Decreased Kidney Function in the Adult US Population: Third National Health and Nutrition Examination Survey. *American Journal of Kidney Diseases: The Official Journal of the National Kidney Foundation* **41**, 1–12 (Jan. 2003).
13. De Lusignan, S. *et al.* Identifying Patients with Chronic Kidney Disease from General Practice Computer Records. *Family Practice* **22**, 234–241 (1st June 2005).
14. Drey, N., Roderick, P., Mullee, M. & Rogerson, M. A Population-Based Study of the Incidence and Outcomes of Diagnosed Chronic Kidney Disease. *American Journal of Kidney Diseases* **42**, 677–684 (1st Oct. 2003).
15. Amato, D. *et al.* Prevalence of Chronic Kidney Disease in an Urban Mexican Population. *Kidney International* **68**, S11–S17 (1st Aug. 2005).
16. Chadban, S. J., Briganti, E. M., Kerr, P. G., Dunstan, D. W., Welborn, T. A., Zimmet, P. Z. & Atkins, R. C. Prevalence of Kidney Damage in Australian Adults: The AusDiab Kidney Study. *Journal of the American Society of Nephrology* **14**, S131–S138 (suppl 2 7th Jan. 2003).
17. Jungers, P., Zingraff, J., Albouze, G., Chauveau, P., Page, B., Hannedouche, T. & Man, N. K. Late Referral to Maintenance Dialysis: Detrimental Consequences. *Nephrology Dialysis Transplantation* **8**, 1089–1093 (1st Jan. 1993).
18. Sesso, R. & Belasco, A. G. Late Diagnosis of Chronic Renal Failure and Mortality on Maintenance Dialysis. *Nephrology Dialysis Transplantation* **11**, 2417–2420 (1st Dec. 1996).
19. Klebe, B. *et al.* The Cost of Implementing UK Guidelines for the Management of Chronic Kidney Disease. *Nephrology Dialysis Transplantation* **22**, 2504–2512 (1st Sept. 2007).

#### 1.4. References

---

20. Precious, K. *NHS England » Programme Budgeting* <https://www.england.nhs.uk/resources/resources-for-ccgs/prog-budgeting/> (2017).
21. Hansen, K. L., Nielsen, M. B. & Ewertsen, C. Ultrasonography of the Kidney: A Pictorial Review. *Diagnostics* **6**. doi:10.3390/diagnostics6010002. pmid: 26838799 (23rd Dec. 2015).
22. Cox, E. F., Buchanan, C. E., Bradley, C. R., Prestwich, B., Mahmoud, H., Taal, M., Selby, N. M. & Francis, S. T. Multiparametric Renal Magnetic Resonance Imaging: Validation, Interventions, and Alterations in Chronic Kidney Disease. *Frontiers in Physiology* **8**. doi:10.3389/fphys.2017.00696 (2017).
23. Buchanan, C. E., Mahmoud, H., Cox, E. F., McCulloch, T., Prestwich, B. L., Taal, M. W., Selby, N. M. & Francis, S. T. Quantitative Assessment of Renal Structural and Functional Changes in Chronic Kidney Disease Using Multi-Parametric Magnetic Resonance Imaging. *Nephrology Dialysis Transplantation*. doi:10.1093/ndt/gfz129 (29th June 2019).
24. Dekkers, I. A. *et al.* Consensus-Based Technical Recommendations for Clinical Translation of Renal T1 and T2 Mapping MRI. *Magnetic Resonance Materials in Physics, Biology and Medicine*. doi:10.1007/s10334-019-00797-5 (22nd Nov. 2019).
25. Wolf, M. *et al.* Magnetic Resonance Imaging T1- and T2-Mapping to Assess Renal Structure and Function: A Systematic Review and Statement Paper. *Nephrology Dialysis Transplantation* **33**, ii41–ii50 (suppl\_2 1st Sept. 2018).
26. Jain, V., Langham, M. C. & Wehrli, F. W. MRI Estimation of Global Brain Oxygen Consumption Rate. *Journal of Cerebral Blood Flow & Metabolism* **30**, 1598–1607 (1st Sept. 2010).
27. Lu, H. & Ge, Y. Quantitative Evaluation of Oxygenation in Venous Vessels Using T2-Relaxation-Under-Spin-Tagging MRI. *Magnetic Resonance in Medicine* **60**, 357–363 (1st Aug. 2008).

## **Chapter 2**

# **Principles of Nuclear Magnetic Resonance Imaging**

---

## Abstract

This chapter outlines the theoretical framework behind Nuclear Magnetic Resonance (NMR) and Magnetic Resonance Imaging (MRI). Beginning with an overview of nuclear spin and resonance, the origin of the signal measured in Nuclear Magnetic Resonance (NMR) is explained. The processes responsible for variations within signals such as relaxation mechanisms is then outlined in addition to techniques used to measure these different signals. Finally an overview of the process by which the signals can be used to form images is given, covering concepts such as spacial localisation, image acquisition schemes and acceleration methods.

## 2.1 Source of the NMR Signal

### 2.1.1 Nuclear Spin

The NMR signal arises from the interaction between the atomic nucleus and an external magnetic field. These atomic nuclei possess intrinsic properties, mass ( $m$ ), charge ( $q$ ) and spin ( $I$ ). Spin is a quantum mechanical property and as such, can only take values of half integers or integers. Nuclear spin is dictated by the sum of the constituent particles of the nucleus, protons and neutrons, each of which possesses their own spin of either  $1/2$  or  $-1/2$  respectively. The additive nature of nuclear spin means that pairs of nucleons can cancel out leaving the nucleus with zero net spin, this happens when the nucleus contains an even number of protons and neutrons. If the nucleus contains an odd number of both protons and neutrons, it will have a positive integer nuclear spin whereas if the nucleus has an odd number of protons or neutrons, it will have a half integer spin.

The spin angular momentum,  $\mathbf{J}$  of a nucleus of spin  $I$  is given by

$$|\mathbf{J}| = \hbar\sqrt{I(I+1)} \quad (2.1)$$

where  $\hbar$  is the reduced Plank's constant,  $h/2\pi$ . As the nucleus is charged and rotating, it gives rise to a current and therefore a magnetic moment  $\mu$ ,

$$\mu = \gamma \mathbf{J} \quad (2.2)$$

where  $\gamma$  is the gyromagnetic ratio for the nucleus, a constant which depends on the charge and mass of the nucleus. Table 2.1 shows the gyromagnetic ratio ( $\gamma$ ) and nuclear spin ( $I$ ) of common NMR sensitive isotopes [1–3]. Due to its high gyromagnetic ratio, compared to other nuclei used for NMR, and relative abundance in the body,  $^1\text{H}$ , a single proton, is most commonly used for Magnetic Resonance Imaging (MRI).

## 2.1. Source of the NMR Signal

---

Isotope	Spin	$\gamma$ (MHzT $^{-1}$ )	Sensitivity Relative to $^1\text{H}$
$^1\text{H}$	$^{1/2}$	42.58	1
$^2\text{H}$	1	6.54	0.0097
$^{13}\text{C}$	$^{1/2}$	10.71	0.016
$^{19}\text{F}$	$^{1/2}$	40.05	0.83
$^{23}\text{Na}$	$^{3/2}$	11.27	0.093
$^{31}\text{P}$	$^{1/2}$	17.25	0.066

Table 2.1: Common NMR isotopes, their nuclear spin, gyromagnetic ratio and sensitivity, relative to  $^1\text{H}$ .

### 2.1.2 Application of an External Magnetic Field

If we consider the hydrogen nuclei in a sample of tissue, the number of possible eigenstates for a nucleus of nuclear spin  $I$  is  $(2I + 1)$ . This means that for the  $^1\text{H}$  nuclei in our sample, where  $I = 1/2$ , we can observe two possible eigenstates,  $|+1/2\rangle$  and  $|{-1/2}\rangle$  often written as  $|\uparrow\rangle$  and  $|\downarrow\rangle$ . In the absence of an external magnetic field, these states are degenerate as they have the same energy, however, if we move our sample into a static external magnetic field along the  $z$ -axis,  $B_0$ , the energy levels separate.

The  $z$ -component of the magnetic moment is defined by,

$$\mu_z = \gamma \hbar m_I \quad (2.3)$$

where  $m_I$  are the possible spin quantum numbers of the nucleus. For our proton system with spin  $1/2$ ,  $\mu_z$  is given by

$$\mu_z = \pm \frac{1}{2} \gamma \hbar. \quad (2.4)$$

The spins can either be aligned parallel to the external magnetic field in the lower energy of the two eigenstates, also known as spin up; or anti-parallel to the magnetic field in the higher energy eigenstate, spin down. The energy

## 2.1. Source of the NMR Signal

---

difference between these two eigenstates is given by,

$$\Delta E = \gamma \hbar B_0. \quad (2.5)$$

For an ensemble of spins in an external magnetic field, there will be an imbalance between the populations of each state with more spins occupying the lower of the two energy states. The net magnetisation of the sample is simply the sum of the constituent spins and as such, the application of an external magnetic field leads to the sample gaining a net magnetisation vector aligned with  $B_0$ . This effect is very small, the magnitude of the imbalance between eigenstates can be derived from Boltzmann statistics and is given by,

$$\frac{N_\uparrow}{N_\downarrow} = \exp\left(\frac{\Delta E}{k_B T}\right), \quad (2.6)$$

where  $N_\downarrow$  and  $N_\uparrow$  are the the number of spins aligned with and against  $B_0$  respectively,  $k_B$  is Boltzmann's constant and  $T$  is the temperature of the system. This means that for a sample of biological tissue at body temperature in a 3T magnetic field, the population difference is very small at approximately three parts per million. Although this measurable proportion is very small, it can be detected due to the high density of protons in the tissue. The signal can also be increased by the application of a stronger  $B_0$ .

### 2.1.3 Precession

Classically, if a magnetic moment,  $M$ , is placed into an external magnetic field,  $B$ , it will experience a torque,  $\tau$ , proportional to change in angular momentum and thus induce a rotation.

$$\mathbf{M} \times \mathbf{B} = \frac{d\mathbf{J}}{dt} = \boldsymbol{\tau} \quad (2.7)$$

## 2.1. Source of the NMR Signal

---

From (2.2) the quantum equivalent of (2.7) is the standard form of the Bloch equation [4],

$$\frac{d\mu}{dt} = \gamma \mu \times \mathbf{B} \quad (2.8)$$

This equation states that if the magnetic moment,  $\mu$  is not aligned with the external magnetic field,  $\mathbf{B}$ , it will precess about  $\mathbf{B}$ . The frequency of this precession,  $\omega_0$  is known as the Larmor frequency and is given by substituting Bohr's frequency condition of the Planck relation ( $\Delta E = \hbar\omega$ ) into (2.5),

$$\omega_0 = \gamma B_0, \quad (2.9)$$

Nuclei with a positive gyromagnetic ratio precess clockwise, whereas nuclei (and the electron) with a negative gyromagnetic ratio precess anti-clockwise. For a proton in a 3T magnetic field, the Larmor frequency is 128 MHz.

### 2.1.4 Resonance

Resonance is the process of energy transfer into a system by the application of energy at the natural frequency of the system. In the case of NMR this is the application of an Radio Frequency (RF) pulse, also known as  $B_1$  field, near the Larmor frequency. Before the RF pulse is applied, the spins are at equilibrium, aligned with  $B_0$ . Upon the application of a  $B_1$  field close to the Larmor frequency of the target nucleus and perpendicular to  $B_0$ , the spins aligned with  $B_0$  will be displaced from equilibrium and thus precession is induced. The longer the  $B_1$  field is applied, the more the net magnetisation vector is displaced, or tipped, away from  $B_0$ , this allows arbitrary flip angles,  $\alpha$ , to be achieved, (2.10).

$$\alpha = \int_0^T \gamma B_1(t) dt \quad (2.10)$$

In addition to displacing the spins, the  $B_1$  field also induces phase coherence within the ensemble making up the net magnetisation vector. When considering the effects of RF pulses, it can often be simpler to imagine the system from

## 2.1. Source of the NMR Signal

---

a reference frame rotating about the  $z$ -axis at the Larmor frequency. This has the effect of making  $B_1$  stationary along the  $x$ -axis. Figure 2.1 shows the evolution of a spin in both the laboratory and rotating frame after the application of a  $90^\circ$  RF pulse. In both figures the spin is tipped into the transverse plane,  $M_{xy}$ .



Figure 2.1: The laboratory frame of reference shows the procession of the spin about  $B_0$  while in the rotating frame, the spin simply rotates about the  $x'$ -axis

## 2.2 Relaxation and Contrast Mechanisms

If disturbed from equilibrium by an RF pulse, the net magnetisation vector will not remain in this new state ad infinitum, instead, once the RF pulse has finished, it will transition back to its equilibrium state in a process known as relaxation. The time constants characterising the relaxation process vary depending on the environment the spins are in and as such, can vary between different biological tissues. These relaxation constants are the principle source of contrast in MRI. Mathematically, this relaxation is described by the full form of the Bloch equation, (2.11).

$$\frac{d\mathbf{M}}{dt} = \gamma(\mathbf{M} \times \mathbf{B}) - \frac{(M_z - M_0)}{T_1}\hat{\mathbf{z}} - \frac{M_x\hat{\mathbf{x}} + M_y\hat{\mathbf{y}}}{T_2} \quad (2.11)$$

### 2.2.1 Longitudinal Relaxation ( $T_1$ )

Upon excitation, energy is exchanged between the spin system and the surrounding environment. The result of this energy exchange is that the energy of the spin system decreases and the longitudinal magnetisation exponentially decays to its equilibrium position. The time constant of this exponential decay returning to equilibrium,  $M_0$ , is known as the longitudinal relaxation time or  $T_1$  and is dictated by the efficiency of energy transfer between the spin system and the surrounding lattice, hence its historical name, spin-lattice relaxation.

The efficiency of this energy transfer is primarily dictated by the motion of the surrounding lattice. As nearby molecules undergo rotation they cause variations in the local magnetic field. If these fluctuations are at a similar frequency to the Larmor frequency then energy transfer via dipole-dipole interactions will be relatively efficient. The rate of energy transfer can also be increased if the molecules are more closely coupled for example, tissues with a lower molecular mobility tend to have a shorter  $T_1$  than those with a high molecular mobility.

### Measuring $T_1$

The longitudinal component of the Bloch equation, (2.11), is given by (2.12).

$$\frac{d\mathbf{M}_z}{dt} = -\frac{(M_z - M_0)}{T_1} \quad (2.12)$$

Solving this equation for  $M_z$  gives,

$$M_z = M_0 \left[ 1 - \exp \left( -\frac{t}{T_1} \right) \right] + M_z(0) \exp \left( -\frac{t}{T_1} \right) \quad (2.13)$$

The gold standard method for quantification of  $T_1$  is the inversion recovery pulse sequence in which a  $180^\circ$  pulse is used to fully invert the magnetisation, such that  $M_z(0) = -M_0$  and as such (2.13) reduces to,

$$M_z = M_0 \left[ 1 - 2 \exp \left( -\frac{t}{T_1} \right) \right]. \quad (2.14)$$

To measure  $T_1$ , the experiment is repeated multiple times, with measurements of  $M_z$  taken at different times after the  $180^\circ$  inversion pulse, Inversion Time (TI). The magnetisation must have fully recovered to  $M_0$  between each inversion pulse, as such the minimum time between inversions, Repetition Time (TR) is five times  $T_1$ . Curve fitting can then be used to estimate  $M_0$  and  $T_1$ , Figure 2.2. This method is expanded upon when it is used in Chapter 6.



Figure 2.2: The longitudinal magnetisation for a sample of  $T_1 = 1000$  ms in an inversion recovery experiment. The experiment was repeated with inversion times from 250 ms to 3000 ms in 250 ms steps.

### 2.2.2 Transverse Relaxation ( $T_2$ and $T_2^*$ )

Upon the application of a  $90^\circ$  RF pulse, the net magnetisation vector has tipped in the  $y'$  direction resulting in phase coherence and creating transverse magnetisation,  $M_{x'y'}$ . The spins then precess about the  $z$ -axis at their Larmor frequency, dictated by the magnetic field they are in. This magnetic field is not perfectly homogenous over the whole ensemble though, random dipole-dipole interaction with neighbouring spins produce short-lived fluctuations in the local magnetic field and thus the Larmor frequency of each spin varies. As the spins precess at different frequencies, they de-phase, resulting in the transverse magnetisation decaying to zero as phase coherence is lost. This mechanism is driven by energy transfer between the spins within the system so is sometimes termed, spin-spin relaxation. The rate at which this loss of phase coherence due to spin-spin interactions occurs is characterised by the time constant  $T_2$ .

The local magnetic field is not just influenced by spin-spin interactions. Local inhomogeneities in the static  $B_0$  field can be caused by susceptibility

## 2.2. Relaxation and Contrast Mechanisms

---

differences within the sample and hardware imperfections. These  $B_0$  inhomogeneities result in additional perturbation to the local magnetic field and therefore results in additional de-phasing of the system. The rate at which this de-phasing due to static  $B_0$  inhomogeneities occurs is characterised by the time constant  $T'_2$ . The measured decay in transverse magnetisation is therefore dictated by  $T_2^*$ , which is related to  $T_2$  and  $T'_2$  by

$$\frac{1}{T_2^*} = \frac{1}{T_2} + \frac{1}{T'_2}. \quad (2.15)$$

### Measuring $T_2$ and $T_2^*$

The transverse component of the Bloch equation, (2.11), is given by (2.16).

$$\frac{dM_{xy}}{dt} = -\frac{M_{xy}}{T_2} \quad (2.16)$$

Solving the differential equation for  $M_{xy}$  with respect to  $t$  gives,

$$M_{xy}(t) = M_{xy}(0) \exp\left(-\frac{t}{T_2}\right), \quad (2.17)$$

It should be noted that (2.17) is an idealised equation and thus does not include static field inhomogeneities that contribute to  $T'_2$  and thus the magnetisation of a real signal will decay with  $T_2^*$ .

After a  $90^\circ$  RF pulse the envelope of the signal will decay with  $T_2^*$ , known as an Free Induction Decay (FID). As such, by measuring the amplitude of the signal at different time points,  $t$ , the decay can be sampled and fit to estimate  $T_2^*$ .

### Spin Echoes

To measure  $T_2$ , rather than  $T_2^*$ , the effects of static  $B_0$  inhomogeneities that lead to  $T'_2$  must be negated. Because the processes driving the de-phasing that lead to  $T'_2$  are constant over time, the refocussing effects of a Spin Echo (SE)

## 2.2. Relaxation and Contrast Mechanisms

---

sequence, outlined in Figure 2.3, can be utilised to reform this de-phasing component. In a SE sequence, an initial  $90^\circ$  excitation pulse shifts  $M$  into the transverse plane and induces phase coherence, Figure 2.4a.  $T_2^*$  effects will then cause some spins to precess quickly and others more slowly and thus dephase with  $T_2^*$ , Figure 2.4b. At time, Echo Time (TE)/2, later a  $180^\circ$  pulse is used to flip the spin ensemble, reversing the phase shift meaning those spins that had accrued the largest positive phase shift will now have the largest negative phase shift and vice versa, Figure 2.4c. Because the  $B_0$  inhomogeneities that lead to  $T_2'$  are static, they will still be acting to the same degree on each spin. This leads to an echo forming at  $t = \text{TE}$  as those spins with the highest Larmor frequency, and largest negative phase shift, refocus or “catch up” with those spins with a lower Larmor frequency, Figure 2.4d. The processes leading to  $T_2$  are not constant over time and as such are not refocussed by the  $180^\circ$  pulse, hence the echo in Figure 2.4d is not perfectly refocussed and the signal will be attenuated at a rate dictated by  $T_2$ .

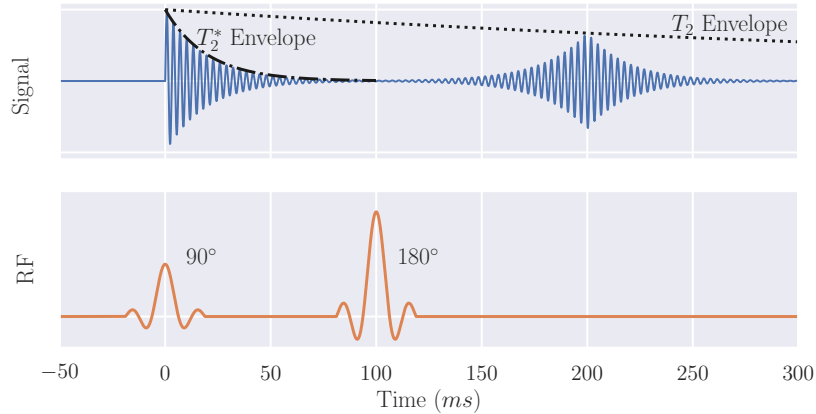


Figure 2.3: The signal produced in a spin-echo sequence used to measure  $T_2$ . This sequence has a TE of 200 ms.



Figure 2.4: Spins evolving in a spin echo sequence showing the de-phasing, (b), refocusing pulse, (c), and subsequent refocusing, (d).

By repeating this sequence over a range of TE the  $T_2$  curve can be samples and fit to (2.17) to estimate  $T_2$  and  $M_{xy0}$ . The SE sequence is the most basic form of  $T_2$  mapping, more methods are explored and compared in Chapter 3.

### Gradient Echoes

Echoes can be generated via another mechanism, the Gradient Echo (GE). In addition to the homogenous  $B_0$  field and RF fields encountered thus far, MRI scanners can produce additional fields known as gradients. These switchable fields can induce linearly varying spatially dependent magnetic fields to perturb  $B_0$ . They are used for image formation, explained in Section 2.3 but can also be used to form an echo. The GE pulse sequence uses a single  $90^\circ$  RF excitation pulse to tip the net magnetisation vector into the transverse plane. A gradient is then applied to the sample causing areas of higher field to de-phase quickly whereas areas with a relatively lower field will de-phase slower. At time  $TE/2$  the polarity of the gradient is reversed thus causing the spins to refocus and an echo to be formed at time  $TE$ . An overview of the sequence is shown in Figure 2.5.

## 2.2. Relaxation and Contrast Mechanisms

---



Figure 2.5: A schematic of a basic Gradient Echo (GE) sequence with TE 200 ms.

In reality, the gradients cannot switch polarity instantaneously due to the inductance of the gradient coils and characteristics of the amplifiers used to generate the gradients. This phenomenon leads to the gradient waveform being trapezoidal, however, to aid clarity in schematics within this chapter, an idealised gradient waveform has been shown. This characteristic of gradients is known as slew rate and is defined as the peak gradient amplitude upon the rise time, Figure 2.6, and for modern MRI scanners is of the order of 200 T/m/s.

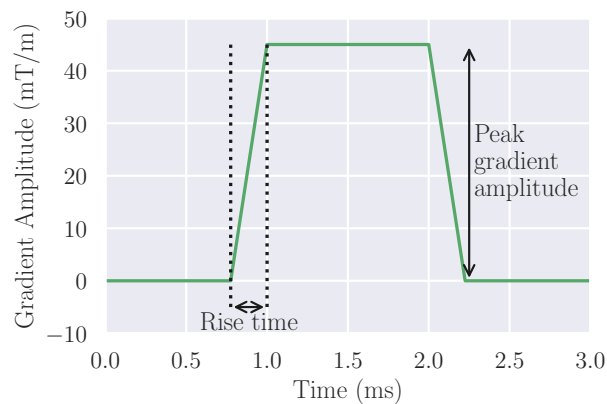


Figure 2.6: A gradient waveform with typical peak gradient amplitude, rise time and slew rate.

### 2.2.3 Dipole-Dipole Interactions

As outlined in 2.2.1 and 2.2.2, dipole-dipole interactions are a primary contributing factor to  $T_1$  and  $T_2$  times. The factors that dictate the strength of these interactions are the types of spin involved, the distance between them, the angle between them and their motion.

The strength of the interaction depends on the gyromagnetic ratio of the spins involved. The magnitude of an electrons gyromagnetic ratio is much greater than that of a proton (-28025 MHzT<sup>-1</sup> and 43 MHzT<sup>-1</sup> respectively [5]) and as such proton-electron interactions are much stronger than proton-proton interactions.

The strength of the interaction is inversely proportional to the sixth power of distance (seen in Equations (2.19) and (2.20)) and thus means that dipole-dipole interactions are only effective over a very short range. As such, the majority of interactions are intramolecular rather than intermolecular.

The  $z$  component of a magnetic field produced by a dipole,  $\mu$  is given by Equation 2.18,

$$B_{\mu z} \propto \frac{\mu}{r^3} (3 \cos^2 \theta - 1) \quad (2.18)$$

producing the field shown in Figure 2.7. Here it can be seen that at certain angles, the magnetic field is zero, this occurs when  $(3 \cos^2 \theta - 1) = 0$  and equates to angles at approximately 54.7°. These angles are known as magic angles. If the dipoles are orientated at approximately the magic angle to the  $B_0$  field, their  $T_2$  will be increased.



Figure 2.7: The  $z$  component of the magnetic field produced by dipole,  $\mu$ .

Molecules can move in three different ways, translation, vibration and rotation. Translation has little effect on NMR signals as it is usually omnidirectional. Vibrational oscillations are at a much higher frequency than NMR phenomenon and as such do not affect the MRI signal. Rotations can be at similar frequencies to MRI and as such, influence  $T_1$  and  $T_2$  due to dipole-dipole interactions.

Each molecule in a sample will have a characteristic correlation time,  $\tau_c$ , the time it takes the molecule to rotate by one radian. The correlation time is effected by how tightly bound the molecules are and their mass, light freely bound molecules like water in liquid form will have a short correlation time while heavy tightly bound molecules such as those found in bone, will have a longer correlation time. If a molecule is tumbling at a rate similar to the Larmor frequency, it will cause energy transfer to be more efficient, thus reducing  $T_1$ . As the tumbling rate slows, the properties of the dipole become more similar to those of a static field, this means that nearby dipoles will experience magnetic fields perpetuated about  $B_0$  and as such  $T_2$  will decrease.

The mathematical framework of this phenomenon is given by the Solomon-

## 2.2. Relaxation and Contrast Mechanisms

---

Bloembergen equations [6] (Equations (2.19) and (2.20)). These equations predict  $T_1$  and  $T_2$  dependence on correlation time, Figure 2.8, where it can be observed that  $T_1$  is lowest when the frequency of the molecular tumbling is similar to the Larmor frequency (labelled as  $\tau_0$  where  $\tau_0 = 1/\omega_0$ ) and that  $T_2$  decreases as correlation time increases. Tissues with a range of tumbling rates are highlighted in Figure 2.8; the molecules in Cerebrospinal Fluid (CSF) are weakly bound as they are in the liquid phase whereas solid tissues such as bone are tightly bound.

$$\frac{1}{T_1} = \frac{6}{20} \frac{\hbar^2 \gamma^4}{r^6} \left[ \frac{\tau_c}{1 + \omega^2 \tau_c^2} + \frac{4\tau_c}{1 + 4\omega^2 \tau_c^2} \right] \quad (2.19)$$

$$\frac{1}{T_2} = \frac{3}{20} \frac{\hbar^2 \gamma^4}{r^6} \left[ 3\tau_c + \frac{5\tau_c}{1 + \omega^2 \tau_c^2} + \frac{2\tau_c}{1 + 4\omega^2 \tau_c^2} \right] \quad (2.20)$$



Figure 2.8:  $T_1$  and  $T_2$  dependence on molecular correlation time as predicted by the Solomon-Bloembergen equations. Tissues with a range of correlation times are highlighted.

### 2.2.4 Diffusion Imaging

Spins have been considered stationary until now, however, in biological tissues, they are often undergoing Brownian motion leading to diffusion. The

## 2.2. Relaxation and Contrast Mechanisms

---

signal from a sample can be made sensitive to the degree of diffusion taking place using diffusion gradients applied between excitation and echo.

Figure 2.9 shows the phase evolution of two spins, one stationary and the other diffusing along the direction the diffusion gradients are applied. The stationary spin accrues a positive phase shift relative to  $\omega_0$  while the first diffusion gradient pulse is applied. The  $180^\circ$  RF pulse flips the spin system so the positive phase shift becomes a negative phase shift of equal magnitude. The spin then evolves under the same field strength in the second diffusion gradient pulse and as such, the diffusion pulses resulted in no net phase shift. The strength of the magnetic field experience by the diffusion spin is dependent on time, in this example, increasing in strength as time passes. This mean that the rate at which phase shifts are accrued increases over time and therefore the refocussing effects of the second diffusion pulse are reduced. This results in a signal attenuation proportional to the rate at which diffusion is occurring, the strength of the diffusion gradients, the time the diffusion gradients are applied for and the time between the two diffusion pulses. The diffusion gradients can either be bipolar, as seen in Figure 2.5 or monopolar if a SE sequence is used, Figure 2.9.

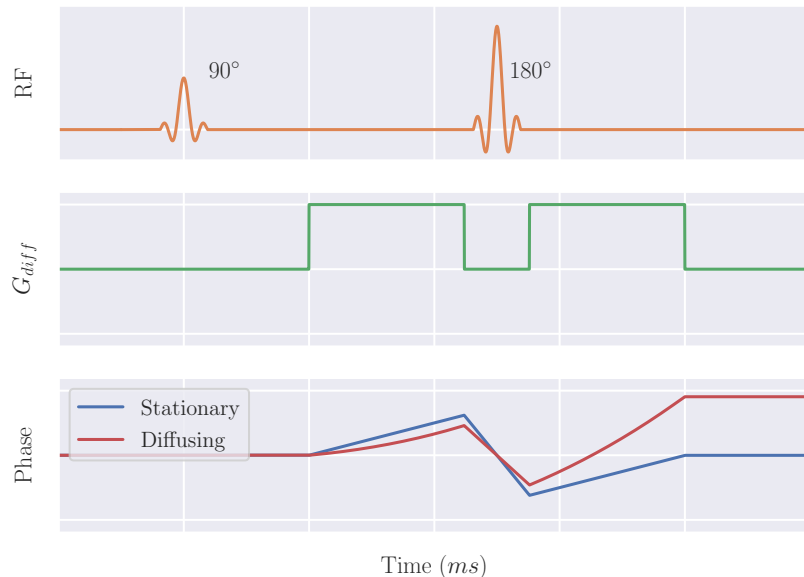


Figure 2.9: Phase evolution of two spins under the influence of monopolar diffusion encoding gradients.

## 2.2. Relaxation and Contrast Mechanisms

---

The interplay between diffusion gradients and measured signal can be mathematically modelled by Equation (2.21),

$$S(b) = S_0 \cdot e^{-b \cdot ADC}, \quad (2.21)$$

where  $b$  is the  $b$ -value, a quantity which dictates the degree of diffusion weighting and is given in units of  $\text{sec}/\text{mm}^2$  and Apparent Diffusion Coefficient (ADC) is the Apparent Diffusion Coefficient of the tissue and reflects the degree with which spins can diffuse through a tissue, given in  $\text{mm}^2/\text{sec}$ . The  $b$ -value can be increased by increasing the gradient strength (this is often limited by scanner hardware), the gradient pulse duration or the spacing between gradient pulses. By repeating the acquisition with different  $b$ -values, the signal from each voxel at each  $b$ -value can be used to estimate ADC (and  $S_0$ ) by fitting the data to Equation (2.21).

Not all diffusion is isotropic (occurs to the same degree in all directions), often the motion of the spins is restricted e.g. within tissue fibres. The amount of restriction is known as the Fractional Anisotropy (FA) where 0 represents isotropic diffusion e.g. a large vial of water, and 1 represents diffusion being constrained to a single dimension. By applying the diffusion gradients in different directions (and strengths) the preferred direction of diffusion and fractional anisotropy can be calculated. These techniques are used in Chapter 6.

### 2.2.5 Optimisation of Tissue Contrast

Quantitative mapping of  $T_1$ ,  $T_2$  and  $T_2^*$  can often be a slow process due to the number of acquisitions required at different time points to sample relaxation curves. Often it is more desirable to acquire a volume at a single time with the intensity difference between tissues of interest maximised. Although the voxel intensities do not directly represent any quantitative underlying physical properties of the tissue, the contrast between tissues is sufficient for diagnosis

## 2.2. Relaxation and Contrast Mechanisms

---

or further analysis.

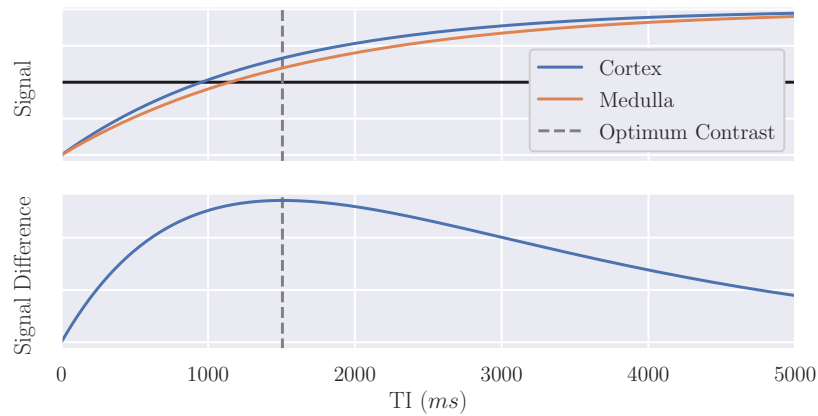


Figure 2.10: The signal generated from renal cortical and medullary tissues [7] and difference between signals. This shows that the contrast between the two tissues is optimal if the Inversion Time (TI) is 1500 ms.

## 2.3 Forming an Image

### 2.3.1 Signal Localisation

So far, NMR has been applied to measure signals from the entire sample, gaining no information about the spatial variation within it. MRI applies the techniques of NMR to spatially resolve the location of the signal.

The key concepts of MRI were developed by multiple groups in the 1970s. Lauterbur used magnetic field gradients and a back-projection reconstruction technique to generate 2D images in 1978 [8]. Simultaneously Mansfield was working on “NMR diffraction” introducing the mathematical framework of reciprocal  $k$ -space [9] and later slice selective excitation [10]. The final key insight was provided by Ernst who published the first Fourier imaging method [11], this used non-selective excitations and linear gradients to generate 2D Fourier encoded images. These techniques are still the basis of MRI today.

The concepts of signal localisation will be introduced through the example of an axial acquisition, Figure 2.11

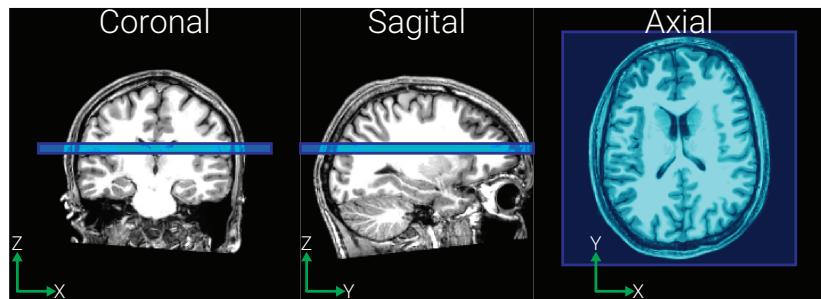


Figure 2.11: Planning used in the signal localisation example.

### Gradient Fields

Signal localisation makes use of gradient fields. These produce small linear perturbations in  $B_0$  and are applied in a combination of the  $x$ ,  $y$  and  $z$  direction to enable arbitrary gradient directions and result in  $B_0$  varying with position,

### 2.3. Forming an Image

---

$\mathbf{r}$ ,

$$B_z(r) = (B_0 + \mathbf{G} \cdot \mathbf{r}) \hat{k}. \quad (2.22)$$

As such, the resonant frequency of the spins can also be described as a function of position and, because the gradients are not static, time,

$$\omega(x, y, z, t) = \gamma (B_0 + G_x(t)x + G_y(t)y + G_z(t)z) \quad (2.23)$$

#### Slice Selection

The initial step in localisation is to measure the signal from a single, spatially defined, slice. If a gradient is applied along the  $z$  direction,  $G_z$ , the magnetic field experienced by the spins at position  $z$  will be

$$B(z) = B_0 + G_z z. \quad (2.24)$$

As such, from the simplification of (2.23), the Larmor frequency becomes

$$\omega(z) = \gamma (B_0 + G_z z). \quad (2.25)$$

If a frequency selective RF pulse is applied to the sample, it will only excite spins within the corresponding bandwidth and thus only a slice of desired thickness. This slice-selective thickness,  $\Delta z$ , can be changed by either adjusting  $G_z$  or the bandwidth of the excitation pulse,  $\Delta\omega$ .

$$\Delta z = \frac{\Delta\omega}{\gamma G_z} \quad (2.26)$$

The excitation profile achieved by a slice selective pulse can be approximated by a Fourier transform. Generally, a rectangular slice profile is wanted and as such, the RF pulse takes the form of a sinc function. To achieve a perfect rectangular pulse, the sinc would have to be infinite in length. Given the lack of infinite time available during an MRI examination, a truncated sinc pulse is used, generally including three or five lobes and a Gaussian filter.

### 2.3. Forming an Image

---

The gradient applied will result in de-phasing of the spins as in a GE sequence, therefore a gradient of the opposite polarity and half the magnitude is applied after the RF pulse to re-phase the spins, Figure 2.12a.

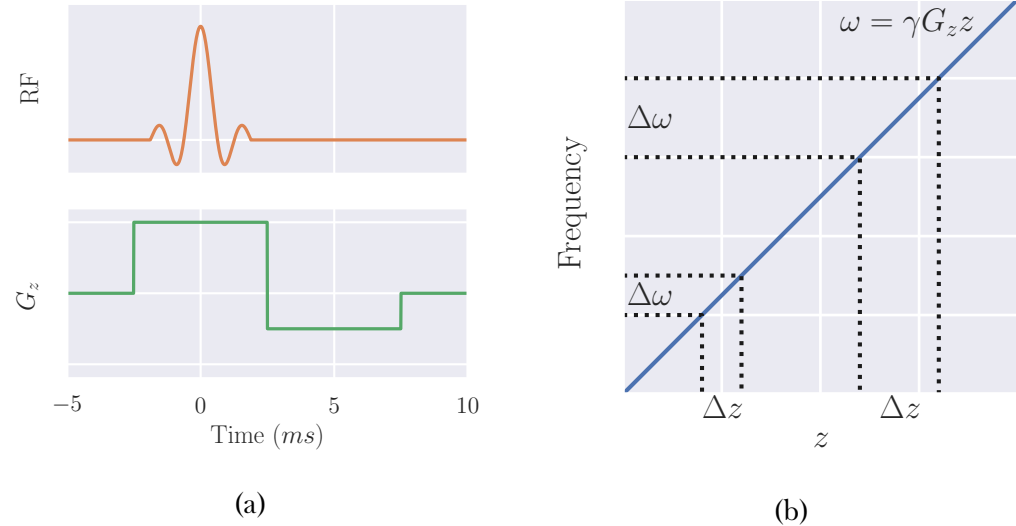


Figure 2.12: (a) A truncated sinc pulse of bandwidth  $\Delta\omega$  being applied over a slice selective gradient followed by the negative re-phasing gradient lobe. Note that the area under the re-phasing gradient is half of that of the slice selective gradient. (b) Example slices of thickness  $\Delta z$  being excited by RF pulses of bandwidth  $\Delta\omega$  showing that excitation pulses of larger bandwidth result in thicker slice profiles.

### Phase Encoding

The signal has been localised from a full 3D volume to a defined 2D volumetric slice. To localise the signal in the next dimension, phase encoding is used. This technique uses a gradient in the  $y$  direction applied for time  $T$ . For the duration of  $G_y$  the spins precess with a frequency according to their position in the  $y$  direction

$$\omega(y) = \gamma(B_0 + G_y y), \quad (2.27)$$

### 2.3. Forming an Image

---

and as such accrue a phase shift relative to if no gradient was applied, given by

$$\phi(y) = \gamma y \int_0^T G_y(t) dt. \quad (2.28)$$

Acquisitions must be repeated with different amplitudes/durations of  $G_y$  to fully sample in the  $y$  direction, Figure 2.14.

Phase aliasing occurs because the whole sample produces signal, whether it is in the Field Of View (FOV) or not. As there is a finite range of phase values (0 to  $2\pi$ ) tissue outside the FOV can have the same value as tissue within the FOV this results in the two signals becoming indistinguishable and therefore combined in a process known as wrapping. This artefact is illustrated in Figure 2.13.

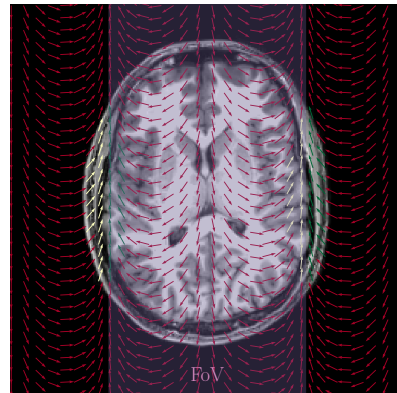


Figure 2.13: Spins outside the FOV have the same phase value as those within the FOV and thus wrapping occurs.

### Frequency Encoding

Finally, the signal needs to be localised in the  $x$  direction. This is achieved using frequency encoding. Here the gradient,  $G_x$  is applied during the acquisition section of the sequence i.e. when the signal is being sampled. As the gradient is being applied during readout, those spins in the centre of the gradient (at field  $B_0$ ) will be precessing at the Larmor frequency while those in a stronger or weaker field will be precessing faster or slower respectively. By sampling the signal generated and applying a Fourier transform to separ-

### 2.3. Forming an Image

---

ate components of the signal at each frequency, the signal is spatially resolved in all three dimensions. An overview of a basic signal localisation scheme is shown in Figure 2.14.

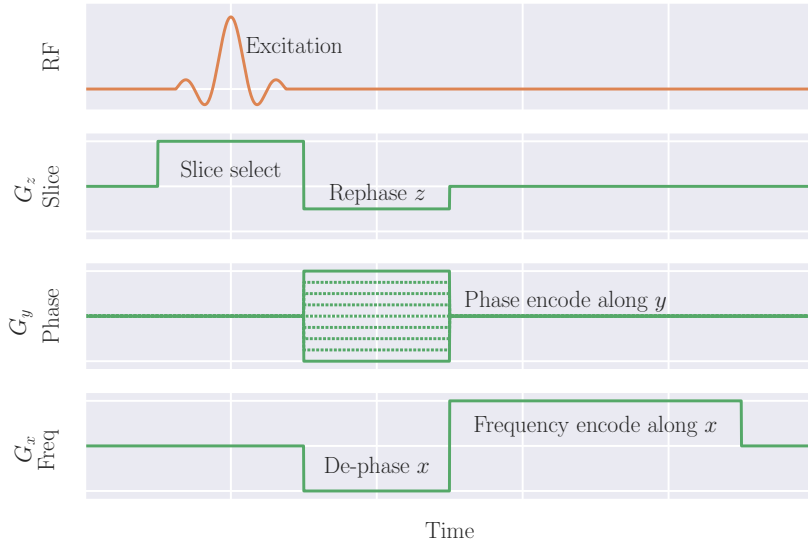


Figure 2.14: A basic spacial localisation pulse sequence showing how gradients applied along the  $z$ ,  $y$  and  $x$  directions can be used to localise the signal in the corresponding dimensions.

### $k$ -space

$k$ -space, sometimes known as Fourier space, is a useful concept for interpreting MRI pulse sequences and represents the spatial frequencies of the image. Immediately after an excitation pulse and rewind gradient, the signal being sampled is at the origin of  $k$ -space, corresponding to low spatial frequencies, or the low resolution aspects of the image e.g. which voxels are inside or outside the body. As gradients are applied to the sample, sampling moves out from the centre of  $k$ -space to higher spatial frequencies corresponding to finer detail within the image. For a 2D acquisition, as above, the location in  $k$ -space is defined by (2.29) and (2.30) where  $G_x$  and  $G_y$  are the gradients in the frequency encode and phase encode directions respectively

### 2.3. Forming an Image

---

and  $t_x$  and  $t_y$  are the duration the gradient is applied for.

$$k_x = \gamma G_x t_x \quad (2.29)$$

$$k_y = \gamma G_y t_y \quad (2.30)$$

When recording MRI data, the continuous signal must be discretised. The higher the sampling frequency i.e. the closer together in  $k$ -space the samples are,  $\Delta k$ , the wider the FOV and the further out from the origin of  $k$ -space is samples, the higher resolution the image will be. Examples of  $k$ -space sampling patterns and their corresponding image are shown in Figure 2.15.

### From $k$ -space to Image Space

The raw data sampled in  $k$ -space can be reconstructed to an image via a Fourier transform. When the quadrature data undergoes a 2D Fourier transform, it produces a complex image composed of a real and imaginary part. These constituent parts of the image can be converted into magnitude and phase images with the magnitude representing the spin density.

### Coordinate Systems

The above example was chosen so that only one gradient is used at once however if the planning of the acquisition is more complicated, the nomenclature can become more confusing, as such, for clarity multiple coordinate systems are often used.

**Scanner Space** This coordinate system has its origin at isocentre of the scanner and is defined in terms of  $x$ ,  $y$  and  $z$ .

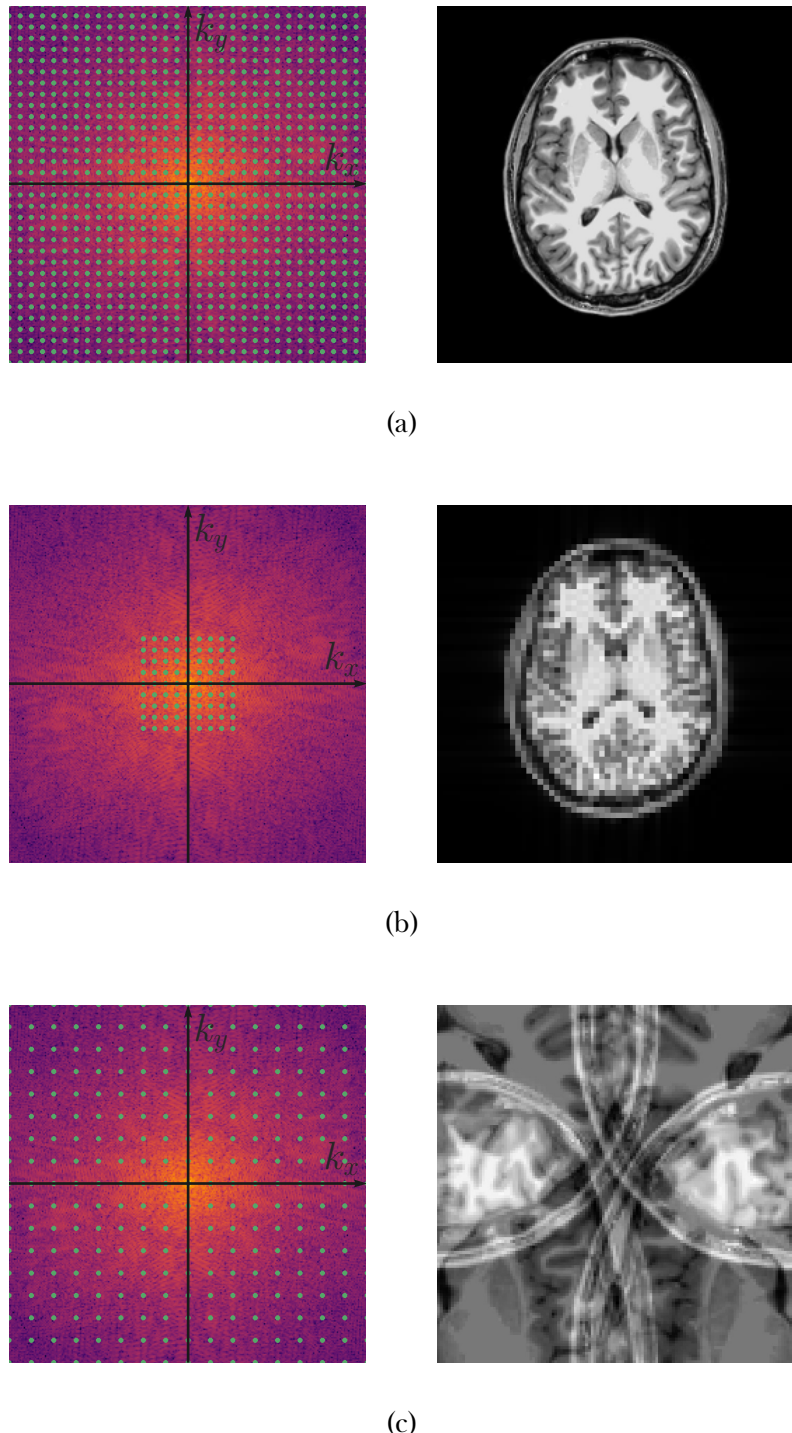


Figure 2.15: (a) Fully samples  $k$ -space and the corresponding image. (b) Centre sampling of  $k$ -space produces a lower resolution image. (c) Sampling with a larger  $\Delta k$  resulting in a decreased FOV and aliasing.

**Imaging Space** The coordinates of this system are defined by the directions used in signal localisation,  $M$  for the frequency encode direction (also called magnitude),  $P$  for the phase encode direction and  $S$  for the slice select direc-

## 2.3. Forming an Image

---

tion.

**Anatomical Space** Defined in terms of the subjects orientation in the scanner, this coordinate system has the axis, Right-Left (R-L), Anterior-Posterior (A-P) and Superior-Inferior (S-I).

### 2.3.2 Image Acquisition Acceleration

One of the recurring limiting factors in MRI is the acquisition time. For neuroimaging applications the relatively slow acquisition of MRI limits subject throughput or the number of different measures that can be performed. In abdominal imaging, acquisition times can be even more of a hindrance given many scans are performed while the subject is holding their breath on expiration. As such, image acquisition acceleration techniques have been developed. These techniques sacrifice a small amount of Signal to Noise Ratio (SNR) for a decrease in acquisition time.

#### Partial Fourier

Fully sampled  $k$ -space contains inherent redundancy as it contains its own complex conjugate; the real components of the signal are symmetric while the imaginary components are anti-symmetric. This means that no contrast information is lost if a reduced area of  $k$ -space is sampled e.g. only sample 66% of  $k$ -space. This technique does impact phase information though so should not be used in acquisitions where downstream processing requires accurate phase. Known as partial Fourier or halfscan, this technique results in a decreased SNR and can introduce image artefacts as the partial Fourier factor approaches 50%, however, the acquisition time reduces by approximately the percentage of  $k$ -space sampled e.g. an acquisition that would take three minutes fully sampled will take two minutes if a partial Fourier factor of 66% is used. An example of reconstructions of 100%, 75% and 51% of  $k$ -space

### 2.3. Forming an Image

---

are shown in Figure 2.16

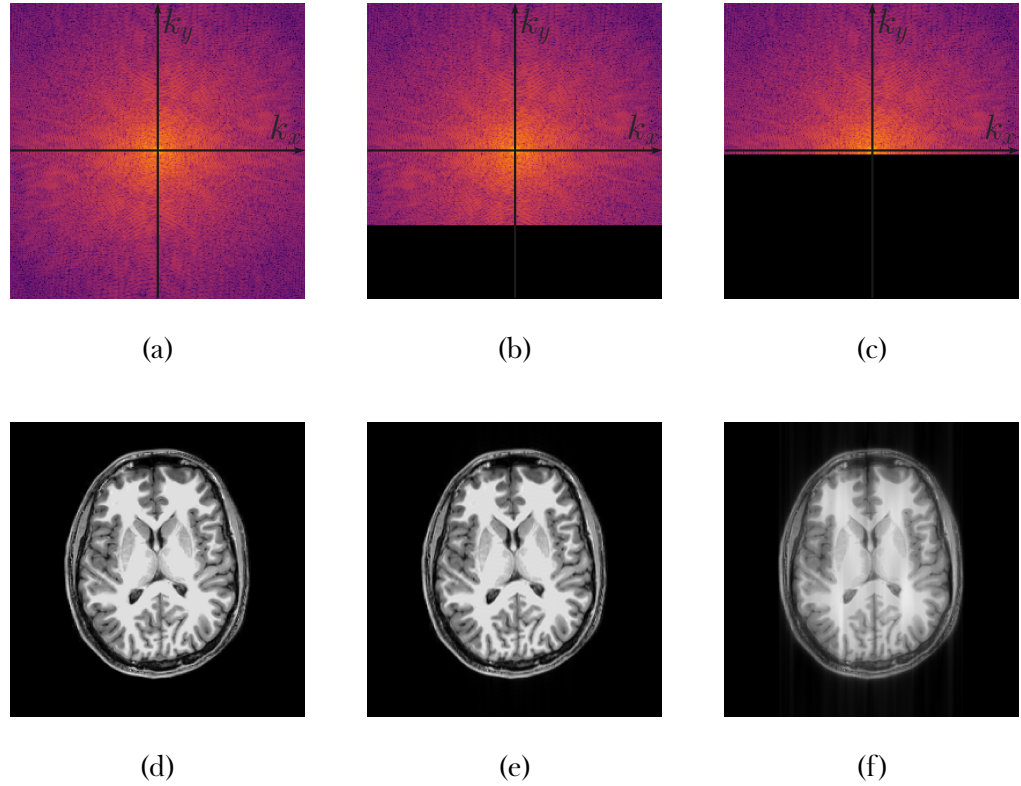


Figure 2.16: Full, (a), 75%, (b), and 51%, (c),  $k$ -space sampling and their corresponding reconstructions in image space, (d), (e) and (f) respectively.

### Sensitivity Encoding (SENSE)

Most modern scanners use different coils for RF transmission, and signal receiving. The transmission coil is usually built into the bore of the magnet while the receive coil is placed as close to the source of the signal as possible. These receive coils are usually composed of multiple smaller coils to make an array, each with its own signal sampling hardware. This means that it is possible to record signal from multiple coils simultaneously with different coils supplying data for each line of  $k$ -space e.g if the array has two coils, one coil will record the odd lines of  $k$ -space and the other, the even lines, thus resulting in an increase in acquisition speed [pruessmann\_sense\_1999]. This parallel sampling technique reduces the lines of  $k$ -space sampled per coil and results in wrapping as seen in Figure 2.15c, albeit only in the phase direction. To

### **2.3. Forming an Image**

---

combat this, the spatial sensitivity profile of each element within the array i.e. the area it can measure signal from, is measured. Using this prior knowledge of signal locations, each coil elements data can be unwrapped before the data from all elements is combined into a single volume.

The Sensitivity Encoding (SENSE) factor is the degree to which  $k$ -space is under-sampled and is limited to the number of elements in the receive array. Applying higher SENSE factors increases acquisition speeds, however, reduces SNR.

#### **2.3.3 Image Acquisition Schemes**

Many different acquisition schemes have been developed for sampling  $k$ -space. Outlined below are some of the key sequences that form the basis of much of MRI.

##### **Spin Warp Imaging**

The simplest uniformly sampled  $k$ -space trajectory is spin warp imaging. This technique is based on the GE scheme and samples one line of  $k$ -space per excitation, or shot, a schematic is shown in Figure 2.17. Each shot applies a different phase encode gradient to move a different amount in the  $k_y$  direction. The signal is then sampled while a gradient is applied in the frequency direction, also known as the readout gradient. The acquisition time for this sequence is very long because it only collects one line of  $k$ -space per shot and as such this technique is sensitive to subject motion.

### 2.3. Forming an Image

---

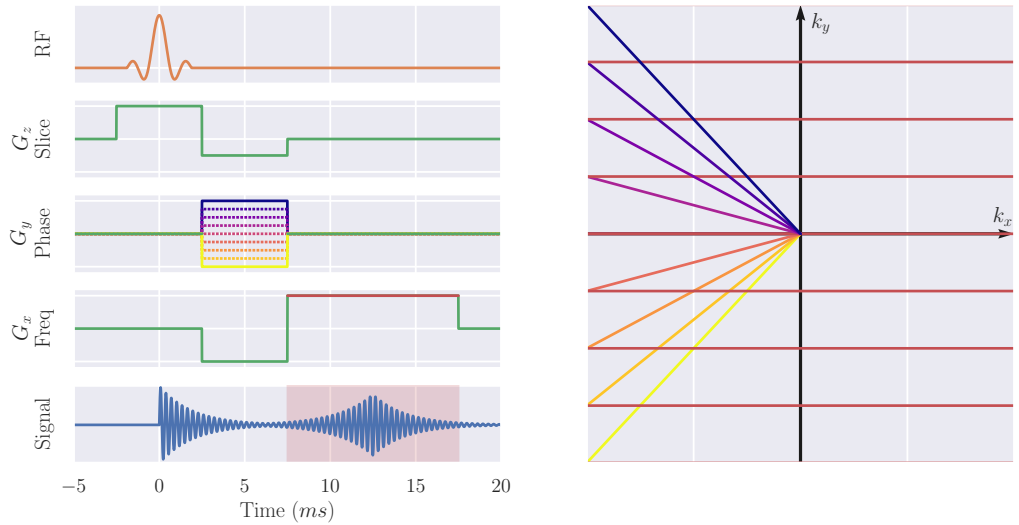


Figure 2.17: A schematic of the spin warp image sequence. The Pulse Sequence Diagram (PSD) shows the different phase encoding gradients,  $G_y$ , in colours from yellow to purple and the readout gradient,  $G_x$ , in red. These colours correlate with the colours in the  $k$ -space trajectory. The signal recorded is highlighted in red.

### Echo Planar Imaging (EPI)

A much faster technique than spin warp imaging is Echo Planar Imaging (EPI) [9]. This technique samples all lines of  $k$ -space in a single excitation shot with an acquisition time typically less than 100 ms. The Pulse Sequence Diagram (PSD) and  $k$ -space trajectory for this sequence are shown in Figure 2.18. The sequence begins very similarly to the spin warp sequence with a slice selective excitation and an acquisition of the bottom line of  $k$ -space, however, instead of a spoiler followed by another excitation as in spin warp imaging, in EPI a small positive phase encode gradient ‘blip’ is applied to move up a line in  $k$ -space, followed by an inversion of the readout gradient polarity. This blip followed by reversed readout is repeated, zig-zagging up  $k$ -space until the desired  $k$ -space is sampled.

### 2.3. Forming an Image

---

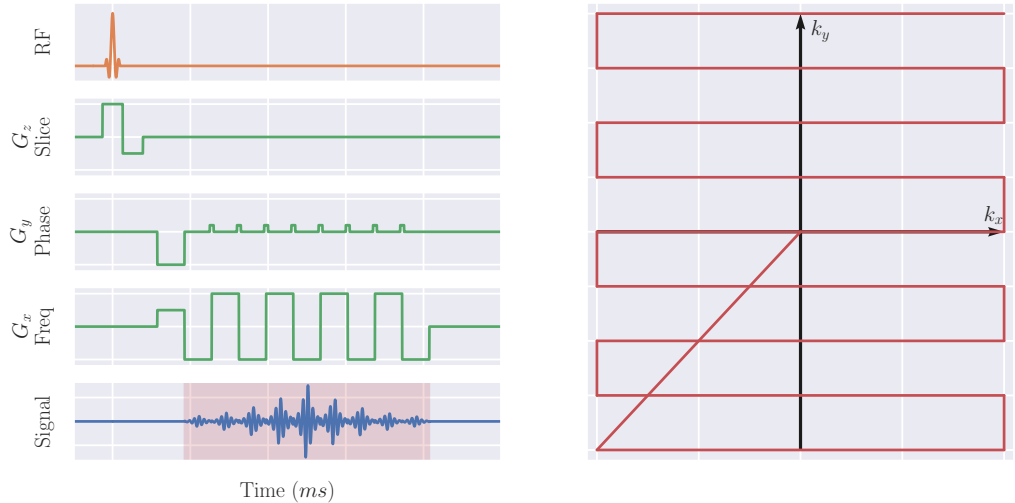


Figure 2.18: A schematic of the EPI pulse sequence and  $k$ -space trajectory. This diagram is not to scale.

While this sequence has a very quick acquisition time, it does have drawbacks. The long train of echoes makes EPI more sensitive to inhomogeneities in the  $B_0$  field caused by different tissue susceptibilities or poor shimming. Eddy currents and imperfections in gradient coils cause small differences in lines collected in the positive and negative direction, leading to a Nyquist ghost artefact. Eddy currents induced by the phase encode blips also cause geometric distortions in the image, Figure 2.19, however, these can be corrected via post processing if an image with phase encode blips of opposite polarity is collected i.e. collect images sampling  $k$ -space from both bottom to top and top to bottom.

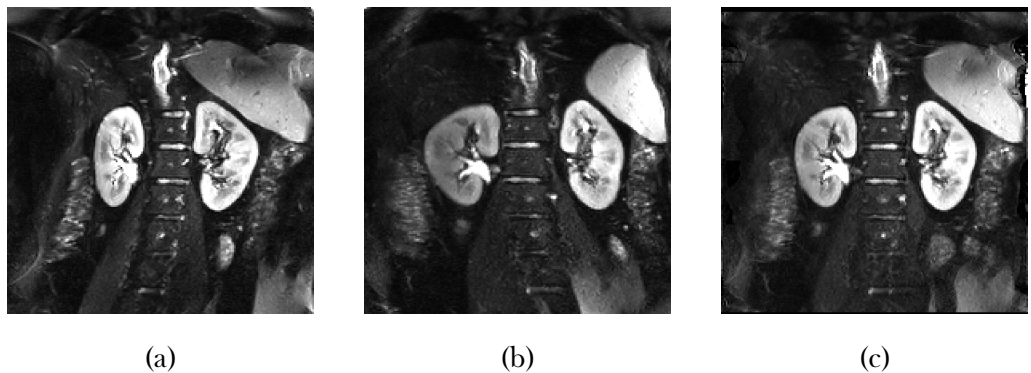


Figure 2.19: Geometric distortions in EPI when phase encode blips are (a) positive, (b) negative and (c) corrected via post processing.

## 2.3. Forming an Image

---

### Turbo Spin Echo (TSE)

The Turbo Spin Echo (TSE) sequence, also known as Fast Spin Echo (FSE) or Rapid Acquisition with Relaxation Enhancement (RARE), is an expansion on the conventional SE sequence applying evenly spaced  $180^\circ$  RF refocusing pulses to generate multiple echo from a single excitation, these echoes are used to record multiple lines of  $k$ -space. The number of echoes is known as the Echo Train Length (ETL), or ‘turbo factor’ and is the factor by which the scan time is reduced compared to a conventional spin echo sequence and is usually between 2 and 30 per TR; the time between echoes is known as the echo spacing and is typically 15 - 25 ms.

Each line of  $k$ -space is acquired at a different time after excitation, as such, they will have different  $T_2$  weightings, it is therefore important to ensure the centre of  $k$ -space is acquired at the desired TE as this echo will dominate the image contrast. The time between excitation and the centre of  $k$ -space is known as the Effective Echo Time (eTE).

The decrease in acquisition time comes at the expense of RF exposure, the large number of  $180^\circ$  pulses leads to lots of energy in the form of heat being deposited in the tissue being imaged, this is known as Specific Absorption Rate (SAR). SAR limits are imposed when scanning to avoid damaging any tissue and as such TSE with its high RF power can easily exceed these limits. Modern TSE sequences can reduce the angle of the refocusing pulse, however this can come at the expense of quantitative accuracy.

### 2.3. Forming an Image

---

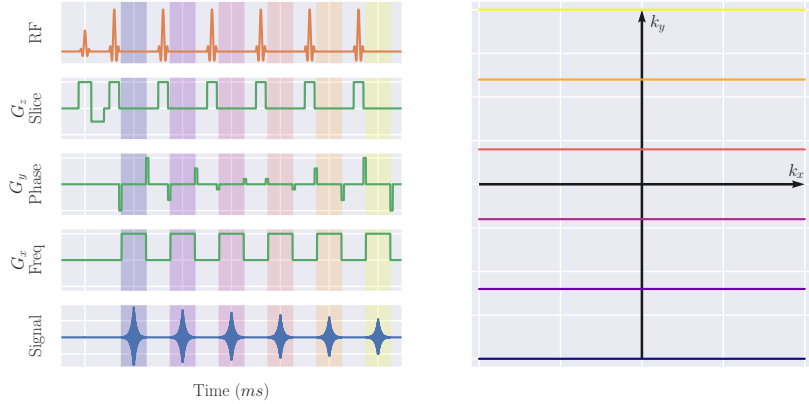


Figure 2.20: A schematic of the TSE pulse sequence and  $k$ -space trajectory. The coloured bands on the PSD correspond to the colours of the  $k$ -space trajectories. Note this diagram is not to scale.

### Half-Fourier Single-shot Turbo spin Echo (HASTE)

The Half-Fourier Single-shot Turbo spin Echo (HASTE) sequence uses a combination of the techniques above. A single excitation is followed by a very long echo train with short echo spacing. This allows a large proportion of  $k$ -space to be sampled within a single TR and thus a whole slice is acquired. To minimise the number of lines of  $k$ -space acquired and thus the ETL, partial Fourier techniques are utilised. The relatively long TE required for a HASTE sequence means images are normally  $T_2$  weighted.

The advantage of HASTE is its rapid acquisition. It can be used to minimise the effects of motion when scanning uncooperative patients, fetuses or structures the subject has no control over such as the bowel. Alternatively it can be used to capture a large FOV in a single breath hold, thus minimising the effects of inconsistent expiration level, as in Chapter 5. The very long ETL can cause significant blurring of the image, thus reducing its clinical readability.

### Turbo Field Echo (TFE)

Turbo Field Echo (TFE), also known as ulatrafast GE, is designed to speed up acquisition of GE images by reducing the TR between excitations. Typical basic GE sequences have relatively long TR to allow the recovery of longitudinal magnetisation. The flip angle used in the TFE sequence is much smaller than the examples explored so far, usually approximately  $10^\circ$  thus leaving a large component of the magnetisation in the longitudinal direction while tipping enough magnetisation into the transverse plane to record a signal at an acceptable SNR. Between each excitation, the transverse magnetisation is spoiled to ensure the images are only  $T_1$  weighted.

After a train of equally spaced RF pulses of flip angle,  $\alpha$ , and period, TR, the longitudinal magnetisation reaches a steady state,  $S_{TFE}$ , after a sufficient number of pulses. This steady state signal depends on the  $T_1$  of the tissue and the FA and TR of the sequence. Assuming perfect transverse magnetisation spoiling between each RF pulse, this equilibrium signal is given by,

$$S_{TFE} = M_0 \frac{\sin(\alpha) [1 - \exp(-TR/T_1)]}{1 - \cos(\alpha) \exp(-TR/T_1)} \exp\left(-\frac{TE}{T_2^*}\right). \quad (2.31)$$

The angle that produces the maximum signal, known as the Ernst angle,  $\alpha_E$ , is given by,

$$\alpha_E = \arccos \left[ \exp \left( -\frac{TR}{T_1} \right) \right]. \quad (2.32)$$

Figure 2.21 shows the ratio of the steady state signal to the fully recovered,  $90^\circ$  excitation signal of renal cortex ( $T_1$  of 1376 ms) for a range of flip angles and TR. Additionally the Ernst angle is shown.

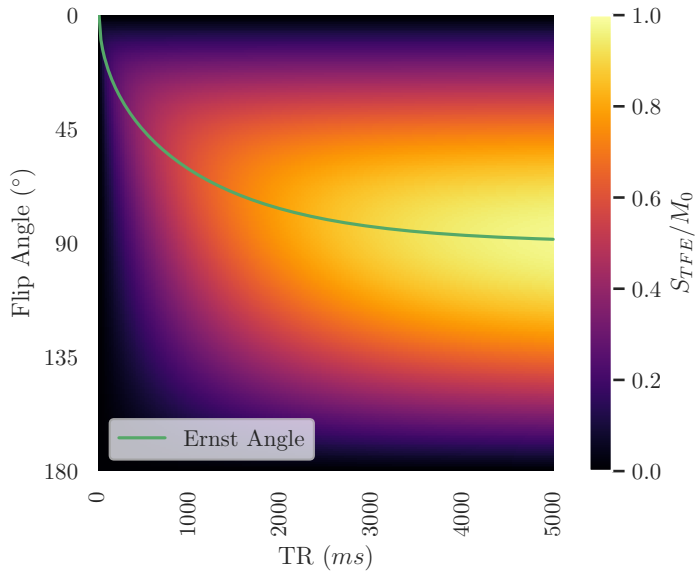


Figure 2.21: The expected steady state signal of a TFE pulse sequence and Ernst angle when imaging renal cortex.

## 2.4 Conclusion

This chapter has introduced the basic concepts of NMR and MRI required for interpreting this thesis. These techniques are built upon in the experimental chapters for quantification of renal properties, both in-vivo and ex-vivo.

## 2.5 References

1. Harris, R. K. N.m.r. and the Periodic Table. *Chemical Society Reviews* **5**, 1–22 (1st Jan. 1976).
2. Bernstein, M. A., King, K. F. & Zhou, X. J. *Handbook of MRI Pulse Sequences* 1041 pp. Google Books: d6PLHcyejEIC (Elsevier, 21st Sept. 2004).
3. Westbrook, C. *MRI at a Glance* 138 pp. Google Books: WeRbCwAAQBAJ (John Wiley & Sons, 18th Nov. 2015).
4. Bloch, F. Nuclear Induction. *Physical Review* **70**, 460–474 (1st Oct. 1946).
5. Mohr, P. J., Newell, D. B. & Taylor, B. N. CODATA Recommended Values of the Fundamental Physical Constants: 2014. *Reviews of Modern Physics* **88**, 035009 (26th Sept. 2016).
6. Solomon, I. Relaxation Processes in a System of Two Spins. *Physical Review* **99**, 559–565 (15th July 1955).
7. Cox, E. F., Buchanan, C. E., Bradley, C. R., Prestwich, B., Mahmoud, H., Taal, M., Selby, N. M. & Francis, S. T. Multiparametric Renal Magnetic Resonance Imaging: Validation, Interventions, and Alterations in Chronic Kidney Disease. *Frontiers in Physiology* **8**. doi:10.3389/fphys.2017.00696 (2017).
8. Lauterbur, P. C. Image Formation by Induced Local Interactions: Examples Employing Nuclear Magnetic Resonance. *Nature* **242**, 190–191 (5394 Mar. 1973).
9. Mansfield, P. & Grannell, P. K. NMR "Diffraction" in Solids? *Journal of Physics C: Solid State Physics* **6**, L422–L426 (Nov. 1973).
10. Garroway, A. N., Grannell, P. K. & Mansfield, P. Image Formation in NMR by a Selective Irradiative Process. *Journal of Physics C: Solid State Physics* **7**, L457–L462 (Dec. 1974).
11. Kumar, A., Welti, D. & Ernst, R. R. NMR Fourier Zeugmatography. *Journal of Magnetic Resonance (1969)* **18**, 69–83 (1st Apr. 1975).

## **Chapter 3**

# **Assessment of Renal $T_2$ Mapping Methods**

---

## Abstract

Renal  $T_2$  mapping shows promising early results for the evaluation of multiple pathologies, however, there is very little consistency between studies due to differing methodologies being employed by each research group. Here the four most common  $T_2$  mapping sequences for use in the kidneys, basic spin echo, multi echo-spin echo, gradient spin echo and Carr-Purcell-Meiboom-Gill (CPMG)  $T_2$  preparation methods, are evaluated.

Each of the four sequences was used to image a phantom with an array of spheres of known  $T_2$  to evaluate quantitative accuracy across the range of  $T_2$  reported in the kidneys. The sensitivity of each sequence to flow was evaluated using a different phantom over a range of flow rates. Additionally, the image quality of each sequence was assessed by estimating the point spread function. All sequences were then used to acquire  $T_2$  maps of five healthy volunteers.

In the static phantom, the basic spin echo sequence delivered the most accurate quantitative results over the range of  $T_2$  reported in the kidneys (40 sm - 200 ms), however its sensitivity to flow and wide point spread function limit its use in-vivo. Instead, a gradient spin echo sequence is recommended, with a mean relative error of  $15 \pm 4\%$  over the range of  $T_2$  reported within the kidneys (40 ms – 200 ms), superior readability due to its smaller point spread function and insensitivity to flow.

This work was presented as an aural presentation at the International Society of Magnetic Resonance in Medicine (ISMRM) 28th Annual Meeting (2020) [1].

### 3.1 Introduction

Quantitative Magnetic Resonance Imaging (MRI) is the process of taking measurements where the voxel values have numerical significance rather than simply representing signal intensity in arbitrary units [2]. These numerically significant values can take the form of macroscale properties such as rate of oxygen consumption and blood vessel flow rates or microscale properties such as tissue  $T_1$  and susceptibility. When interpreted, these values can be used to improve diagnosis and treatment of patients.

The kidneys are structurally and functionally complex organs and as such lend themselves to the wide variety of MRI protocols designed to probe different aspects of the tissue and processes carried out within. While high resolution images of the kidneys morphology and basic measures such as Total Kidney Volume (TKV) can be very useful in diagnosing and monitoring disease progression [3–5], these do not fully leverage the quantitative nature of MRI. Measurements of  $T_1$  have been shown to correlate well with fibrosis in the myocardium [6, 7], liver [8, 9] and kidneys [10] and more generally an increase in  $T_1$  is associated with Chronic Kidney Disease (CKD) [3, 11, 12]. Arterial Spin Labelling (ASL) techniques can be used to quantify renal perfusion in physiological units ( $\text{mL}/100\text{g}/\text{min}$ ) and have been shown to correlate with allograft function post renal transplant in addition to cold ischemia time and the recipients Estimated Glomerular Filtration Rate (eGFR) [13–16]. Additionally ASL has been used to measure a decrease in perfusion in CKD subjects [11, 17, 18]. These techniques have proved useful when used individually however they can be combined and used in the same scanning session to greater effect as a multiparametric protocol [3, 12, 19–21].

$T_2$  mapping has found wide use in cardiac MRI for assessment of myocardial edema [22–24] and iron overload [25, 26]. It has also effectively been used in the brain to study multiple sclerosis [27], epilepsy [28], dementia [29] and Parkinson’s disease [30]. Despite these developments elsewhere in the body,  $T_2$  mapping has had limited uptake in the renal community.

### 3.1. Introduction

---

Renal  $T_2$  mapping has seen most research focusing on repeatability measures [31–34] with clinical uses in the field of assessment of allograft function in mice [21] and humans [35, 36], and has shown potential for early diagnosis of Autosomal Dominant Polycystic Kidney Disease (ADPKD) [37] and assessment of clear cell renal cell carcinoma [38].

In the existing literature, there is a substantial variation in quoted  $T_2$  values within the kidneys of healthy volunteers, this is thought to be, in part, due to the differences in  $T_2$  mapping methodologies. There are currently four main methods that have been utilised in the kidneys, a basic spin echo method, a multi echo-spin echo method, a gradient spin echo method and a Carr-Purcell-Meiboom-Gill (CPMG)  $T_2$  preparation method. Here each of the four methods is compared in the context of renal  $T_2$  mapping to ascertain which is most suitable. This is achieved by evaluating each methods quantitative accuracy, image quality, sensitivity to flow in phantoms and suitability for use in-vivo in a cohort of five healthy subjects.

## 3.2 Methods

### 3.2.1 Data Acquisition

All data was acquired on a 3T Philips Ingenia system (Philips Medical Systems, Best, The Netherlands). The 14 element  $T_2$  array of a QalibreMD System Standard Model 130 contains spheres doped with varying concentrations of  $MnCl_2$  to modulate  $T_2$  between 5 ms and 650 ms, Figure 3.1. This array was used to compare the accuracy of  $T_2$  measurements to a known ground truth. Additionally, a square grid etched into the plastic of the phantom was used to assess the degree of image blurring.

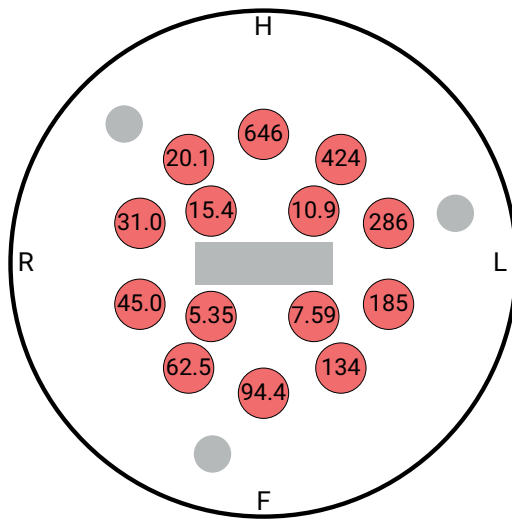


Figure 3.1: A schematic of the  $T_2$  spheres in the QalibreMD phantom.

To investigate the effects of flow upon  $T_2$  measurements, a Gold Standard Phantoms Quantitative Arterial Spin Labelling Perfusion Reference (QASPER) phantom was used. This allows the  $T_2$  of the perfusate to be measured at rest and whilst being pumped through the phantom at a range of flow rates.

Both phantoms were scanned using a 32-channel head coil. All data acquired on human subjects was done with approval of the local ethics committee and the study was conducted in accordance with the Helsinki Declaration.

### **3.2. Methods**

---

The subjects gave written, informed consent. Humans were scanned using a 16-channel anterior coil array and 16-channel posterior coil array. The study cohort consisted of 5 healthy participants (2 female, 3 male, mean age  $31 \pm 8$ ).

The protocol comprised of a survey, localisers,  $B_0$  and  $B_1$  mapping, then each of the optimised  $T_2$  mapping sequences. In-vivo subjects also had  $T_2$ -weighted and  $T_1$ -weighted structural scans to enable segmentation of the whole kidneys, and cortex/medulla respectively [39, 40], these Region Of Interest (ROI) were then used to calculate the mean  $T_2$  of each tissue type. The basic principles of  $T_2$  mapping are outlined in Section 2.2.2. A summary of the parameters of each  $T_2$  mapping sequence is shown in Table 3.1. Each protocol was designed to be between approximately two and three minutes (before respiratory triggering) and keep key parameters such as voxel size and Field Of View (FOV) constant. More accurate or higher resolution  $T_2$  mapping may be possible with longer acquisition times, however as the aim is for this sequence to be used as part of a multi-parametric protocol, the time constraints of the whole protocol must be considered.

### 3.2. Methods

---

	Spin Echo - Echo Planar Imaging	Multi-Echo Turbo Spin Echo	Gradient Spin Echo	CPMG $T_2$ Pre- paration - Echo Planar Imaging
Abbreviation	SE-EPI	ME-TSE	GraSE	CPMG $T_2$ Prep
TE (min:step:max) (ms)	20:10:70	13:13:130	11.2:5.6:173.3	0:20:160
Number of echoes	6	10	30	9
Startup echoes	N/A	0	1	N/A
TR (ms)	5000	3000	3000	3000
Voxel Size (mm <sup>3</sup> )	$3 \times 3 \times 5$	$3 \times 3 \times 5$	$3 \times 3 \times 5$	$3 \times 5.65 \times 5$
FoV (mm <sup>3</sup> )	$288 \times 288 \times 25$	$288 \times 288 \times 25$	$288 \times 288 \times 25$	$288 \times 288 \times 25$
Signal Averages	2	1	1	1
Acquisition Mode	Multi Slice	Multi Slice	Multi Slice	Multiple 2D
Fast Imaging Mode	EPI	TSE	GraSE	TFEPI
Flip Angle	90°	90°	90°	90°
Bandwidth (Hz)	40	180	405	113
SENSE	2.55	2.55	2.55	3
Halfscan	0.838	No	No	0.706
TSE Factor	N/A	10	30	N/A
EPI Factor	37	N/A	3	17
Respiratory Compensation	Triggered	Triggered	Triggered	Triggered
Acquisition Time (before respiratory compensation)	3 min 0 sec	1 min 57 sec	2 min 6 sec	2 min 23 sec

Table 3.1: A summary of the acquisition parameters of each of the  $T_2$  mapping methods compared.

### 3.2. Methods

---

#### Spin Echo-Echo Planar Imaging

This technique is the simplest of the four consisting of a  $90^\circ$  excitation pulse, followed by a  $180^\circ$  Radio Frequency (RF) pulse Echo Time (TE)/2 ms later, leading to an echo at TE. The  $180^\circ$  pulse corrects for components of the signal lost due to static field inhomogeneities,  $T_2'$  effects, however does not correct for  $T_2$  effects. By repeating the sequence multiple times with different TE, the  $T_2$  decay can be sampled. An Echo Planar Imaging (EPI) readout is used to sample the signal during the echo. This sequence suffers from a relatively low Signal to Noise Ratio (SNR), hence two signal averages are acquired; this means that only six different echo times can be sampled in the target acquisition time window. An overview of the sequence is shown in Figure 3.2.

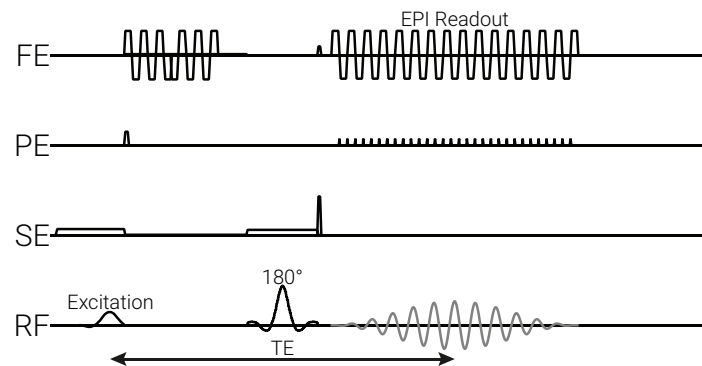


Figure 3.2: A pulse sequence diagram of the SE-EPI scheme.

### 3.2. Methods

---

#### Multi-Echo Turbo Spin Echo

This sequence also uses a multi-slice spin echo; however the EPI readout is substituted for a Turbo Spin Echo (TSE) readout. This replaces the single  $180^\circ$  pulse with a train of pulses with an echo forming between each allowing the whole  $T_2$  decay to be sampled in a single echo train. Different echo times are sampled by varying the number and spacing of the  $180^\circ$  pulses. The decrease in acquisition time per echo compared to the SE-EPI sequence means that ten echoes can be collected per  $T_2$  map at the minimum possible echo spacing, 13 ms. A schematic of the Pulse Sequence Diagram (PSD) can be seen in Figure 3.3.

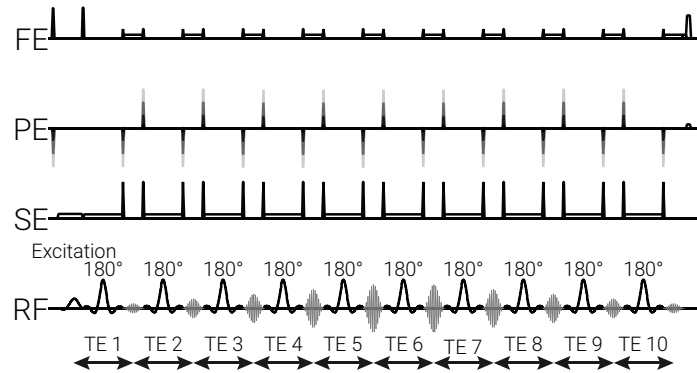


Figure 3.3: A pulse sequence diagram of the Multi-Echo Turbo Spin Echo (ME-TSE) scheme.

### 3.2. Methods

#### Gradient Spin Echo

To achieve further acceleration over the ME-TSE sequence, a Gradient Spin Echo (GraSE) sequence can be used. Here two gradient echoes are collected for every spin echo; the spin echo and gradient echo are used for the acquisition of the centre and periphery of  $k$ -space respectively. The multiple  $k$ -space profiles collected per spin echo enables a decrease in the echo spacing of the sequence compared to the ME-TSE sequence, decreasing to 5.6 ms and thus thirty echoes are collected per  $T_2$  map. The first echo of the train has an artificially high signal, however the short echo spacing of this technique means a startup echo can be sacrificed i.e. the first echo is sampled at 11.2 ms rather than 5.6 ms. This leads to a more accurate fit, while also retaining accuracy when measuring short  $T_2$  signals that will quickly decay. The PSD for the GraSE acquisition is shown in Figure 3.4.

Due  
to  
stim-  
ulate  
echoes?

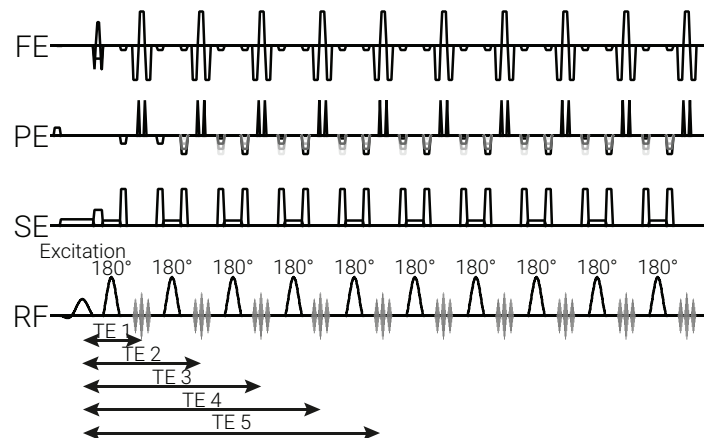


Figure 3.4: A pulse sequence diagram of the GraSE scheme.

### 3.2. Methods

---

#### CPMG $T_2$ Preparation

The CPMG  $T_2$  preparation sequence is considered the gold standard in terms of accuracy. As in the other sequences, this sequence begins with a  $90^\circ$  excitation pulse to transfer the magnetisation into the transverse plane. Carr and Purcell showed that a series of  $180^\circ$  pulses of alternating phase could be used to reduce the effects of molecular diffusion. These molecules diffuse into an area of slightly different magnetic field and thus experience a different Larmor frequency, causing an attenuation in transverse magnetisation above that of  $T_2$  [41]. This technique relies on very accurate  $180^\circ$  pulses as small imperfections could result in large cumulative errors over the length of the pulse train. Later Meiboom and Gill showed that by delivering the  $180^\circ$  pulses  $90^\circ$  out of phase to the initial excitation pulse e.g. excite about  $x'$  and refocus about  $y'$ , the undesirable effects of imperfect  $180^\circ$  pulses and  $B_1$  inhomogeneity could be greatly reduced [42]. The resulting sequence, known as a Carr-Purcell-Meiboom-Gill (CPMG) sequence, can be used to generate robust measurements of  $T_2$ ; by varying the number and temporal spacing,  $\tau_{\text{CPMG}}$ , of the  $180^\circ$  pulses the degree of  $T_2$  weighting can be modulated to achieve different Effective Echo Time (eTE). An EPI readout scheme is then used to sample the signal. An overview of this sequence is shown in Figure 3.5.

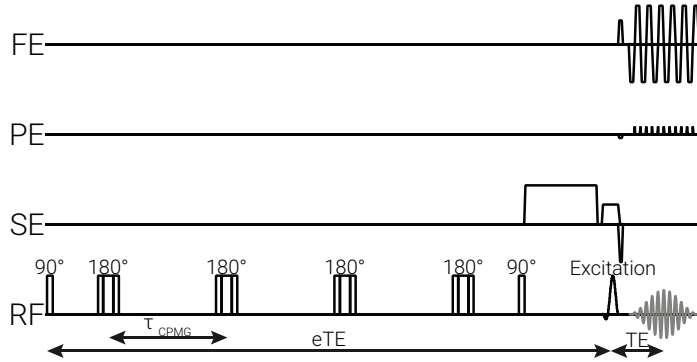


Figure 3.5: A pulse sequence diagram of the CPMG  $T_2$  preparation scheme.

### 3.2.2 Post Processing

All post processing was performed using Python 3.7 making use of the United Kingdom Renal Imaging Network (UKRIN) Kidney Analysis Toolbox (UKAT) [43, 44]. This open source software is specially designed for quantitative renal MRI. All curve fitting uses a least squares trust region reflective method to estimate unknown parameters.

#### *T<sub>2</sub>* Fitting Methods

The data were fit using a mono-exponential model, however, there are multiple models for fitting noisy data, each of which was evaluated here and illustrated in Figure 3.6. The basic fit simply takes the signal from each voxel at each TE and fits it to

$$S(t) = S_0 \cdot e^{-t/T_2}. \quad (3.1)$$

If no noise was present in the data and the sample was a single pure substance i.e. does not exhibit partial voluming effects, this would be the optimum method however, decreased SNR of later TE often leads to inaccurate fits. To combat this, the equation the data is fit to can be modified to

$$S(t) = S_0 \cdot e^{-t/T_2} + \epsilon, \quad (3.2)$$

where  $\epsilon$  represents thermal noise and a baseline in the signal due to long  $T_2$  compartments; this fitting method is referred to as “noise fit”. Another common method of negating the effects of the low SNR of later TE is to discard data below a threshold, illustrated in Figure 3.6 at 0.2 AU and referred to as “discard fit”. Finally, a combination of both noise estimation and discarding can be performed (discard and noise fit). All four of these fitting methods will be compared.

### 3.2. Methods

---

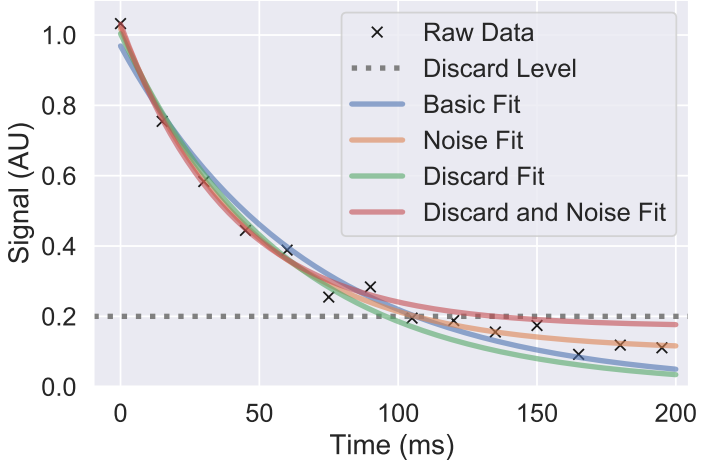


Figure 3.6: Each of the four fitting methods being used to estimate  $T_2$  of the same simulated data.

These fitting methods can either be applied on a voxel-by-voxel basis to generate spatial maps or, the signal from all voxels in an ROI with a single  $T_2$  can be averaged at each TE with parameters being fit to the subsequent mean signal.

#### 3.2.3 Assessment of Data

##### Quantifying Accuracy

Using the QalibreMD phantom, the quantitative accuracy of each of the sequences was assessed. A voxel-by-voxel  $T_2$  map was calculated for each sequence, ROI were then defined for each of the spheres in the  $T_2$  array, Figure 3.7, and the mean  $T_2$  within each sphere calculated. The estimated values of  $T_2$  were compared to the ground truth literature values and their discrepancy assessed over both the full range of  $T_2$  in the array (5 ms – 650 ms) and the range of  $T_2$  reported in the kidneys (40 ms – 200 ms) [45]. Accuracy was summarised over these ranges using Mean Relative Error (MRE) defined as

$$\text{MRE} = \frac{1}{N} \sum_n \left| \frac{t_{2,i}^{\text{ground truth}} - t_{2,i}^{\text{estimate}}}{t_{2,i}^{\text{ground truth}}} \right|. \quad (8.3)$$

### 3.2. Methods

---



Figure 3.7: The  $T_2$  spheres inside the QalibreMD phantom.

#### Effects of Flow

The kidneys are highly perfused organ, as such, the effects of fluid flow through the area being imaged should be evaluated. This was achieved using a Gold Standard Phantoms QASPER phantom, Figure 3.8. This phantom comprises of a MRI compatible pump with adjustable, continuous, flow rates from 0  $\text{m}\ell/\text{min}$  to 350  $\text{m}\ell/\text{min}$ . The perfusate exists the pump into a series of simulated arterioles before entering a cylinder of porous media designed to simulate a capillary bed. Having travelled through the porous media, the perfusate exists at the centre of the cylinder and is returned to the pump. The porous media is imaged using each sequence over the full range of flow rates the phantoms pump can deliver.  $T_2$  maps are calculated and the mean  $T_2$  calculated to evaluate the robustness of each sequence to variations in perfusion.

### 3.2. Methods

---

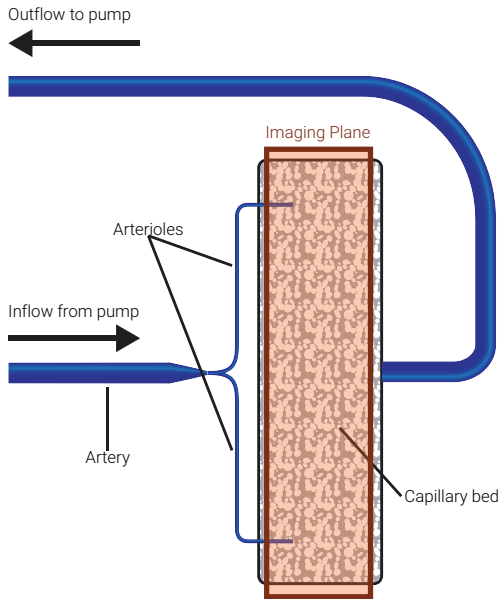


Figure 3.8: A schematic of QASPER phantom used to quantify the effects of flow upon the  $T_2$  measurements.

### Blurring

Unfortunately MRI doesn't produce perfect images, every signal is subject to a degree of blurring or spreading out into surrounding voxels. The amount of this blurring is different for each sequence and can dramatically effect the readability of an image and ultimately its clinical utility. In MRI the amount and characteristics of the blur is usually spatially invariant, that is to say, if a voxel in the centre of an image is blurred over its five neighbouring voxels in the phase encode direction, a voxel at the edge of the image would also be blurred over its five neighbouring voxels. The degree of blurring produced by each of the sequences outlined in Section 3.2.1 will be quantified.

The observed image,  $h$ , can be modelled as an ideal, unblurred signal,  $f$  distorted by a filter,  $g$ , Figure 3.9. This distorting filter is known as the Point Spread Function (PSF) and is the theoretical signal produced when imaging an infinitely small point source object or, in practice, the blurring observed in the imaging system when an object much smaller than the systems resolving power is imaged. In a spatially invariant system, such as MRI, the recorded

### 3.2. Methods

---

signal is simply a convolution of the true signal and the PSF i.e.  $f * g = h$ . By fitting a Gaussian to the PSF the degree of blurring in the image can be quantified [46, 47].

$$\begin{array}{c} \text{---} \\ \text{---} \\ f \end{array} * \begin{array}{c} \text{---} \\ \text{---} \\ g \end{array} = \begin{array}{c} \text{---} \\ \text{---} \\ h \end{array}$$

Figure 3.9: The convolution of the ideal signal,  $f$ , and the PSF,  $g$ , produces the measured signal,  $h$ .

A 3 mm deep, 2 mm thick, grid etched into one of the plastic plates of the QalibreMD phantom, Figure 3.10, was imaged using each of the  $T_2$  mapping methods with an echo time of 20 ms. A  $0.5 \text{ mm}^3$  isotropic structural scan was also collected. The thickness of the grid is smaller than the imaging resolution of the  $T_2$  mapping sequences and the resolution of the structural scan is much greater than the resolution of the  $T_2$  mapping scans, therefore the structural scan can be seen as an approximation of the ideal image produced by each  $T_2$  mapping method. This allows a deconvolution of the PSF from the  $T_2$  mapping scans and, by fitting a Gaussian to the line profiles through the centre of the PSF in each direction, an estimate the Full Width Half Maximum (FWHM) of the PSF as shown in Figure 3.11. Quoted values are the maximum PSF of each of the two directions as this is the limiting factor in an images readability, for the example in Figure 3.11, the quoted PSF would be  $9.49 \pm 0.23 \text{ mm}$ .

Would  
a 2D  
ex-  
ample  
of  
ap-  
ply-  
ing a  
Gaus-  
sian  
blur  
to  
an  
im-  
age  
be  
help-  
ful  
here  
too?

### 3.2. Methods

---

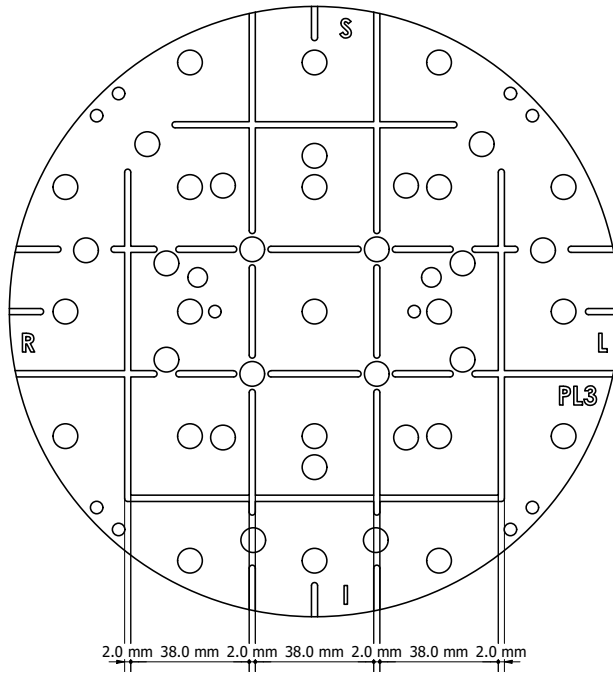


Figure 3.10: A scale drawing of plate three of the QalibreMD system phantom. The grid etched into this plate was used to assess the blurring of each  $T_2$  mapping sequence.



Figure 3.11: An overview of the estimation of the PSF. The  $T_2$  weighted data has had additional blur added to make the effect of each processing step clearer.

### **3.2. Methods**

---

#### **In-Vivo**

Using the  $T_1$ -weighted structural scans ROI were defined for both the renal cortex and medulla of each subject. These ROI were then used to calculate the mean and standard deviation  $T_2$  for each tissue type of each subject. Histogram analysis was also performed to interrogate the distribution of  $T_2$  within each tissue.  $T_2$  maps were qualitatively assessed for their readability.

## 3.3 Results

### 3.3.1 Fitting Methods

Each fitting method was tested using data acquired on the QalibreMD phantom and in-vivo. A full breakdown of the accuracy of each fitting method, applied to each sequence, over different ranges of  $T_2$  can be seen in Table 3.2 and Figure 3.12. The designers of the phantom calculate the mean signal from each sphere then fit to a  $T_2$  decay, resulting in a quicker and more accurate measurement of the homogenous  $T_2$  of each sphere [48]. Due to the heterogeneity within the kidneys, this method could not be applied in-vivo and as such, the accuracy of the sequences and fitting methods was evaluated by performing a voxel-by-voxel fit, then calculating the mean  $T_2$  from an ROI of each sphere in the resulting map.

$T_2$ Range	MRE (5 ms – 650 ms) (%)				MRE (40 ms – 200 ms) (%)			
	Basic	Noise	Discard	Discard and Noise	Basic	Noise	Discard	Discard and Noise
SE-EPI	$36 \pm 34$	$202 \pm 437$	$33 \pm 34$	$238 \pm 463$	$8 \pm 5$	$32 \pm 42$	$22 \pm 8$	$31 \pm 42$
ME-TSE	$38 \pm 31$	$13 \pm 16$	$41 \pm 35$	$35 \pm 36$	$23 \pm 13$	$14 \pm 3$	$15 \pm 13$	$13 \pm 4$
GraSE	$32 \pm 29$	$23 \pm 27$	$26 \pm 28$	$33 \pm 37$	$15 \pm 4$	$11 \pm 5$	$13 \pm 4$	$9 \pm 7$
CPMG $T_2$ Prep	$18 \pm 15$	$30 \pm 53$	$20 \pm 18$	$28 \pm 28$	$11 \pm 1$	$8 \pm 5$	$11 \pm 1$	$6 \pm 5$
Mean over se- quences	$31 \pm 8$	$67 \pm 90$	$30 \pm 9$	$83 \pm 103$	$14 \pm 7$	$16 \pm 11$	$14 \pm 36$	$15 \pm 11$

Table 3.2: MRE when measuring  $T_2$  of the QalibreMD phantom over different ranges using each sequence and fitting method. 5 ms – 650 ms is the full range of  $T_2$  available in the phantom and 40 ms – 200 ms is the range of  $T_2$  reported in the kidneys.

### 3.3. Results

---



Figure 3.12:  $T_2$  maps generated using each of the fitting methods using the GraSE sequence. The reduction in longer  $T_2$  values when fit with a noise term observed in the phantom can be seen here in the decreased  $T_2$  of the kidneys, while the spleen remains relatively similar. Discarding has relatively little effect on the kidneys but does increase the variance in  $T_2$  within the cortex and medulla compared to the basic fit.

The noise fit results in an increase in accuracy compared to the basic fit when measuring the  $T_2$  of the shortest  $T_2$  spheres, especially for sequences with a short echo spacing where the majority of echoes in the signal are after the sphere has fully relaxed back to its baseline noise level. This increase in accuracy for short  $T_2$  is at the expense of the accuracy of the long  $T_2$  spheres. The combination of decreased dynamic range and an extra parameter to optimise resulted in an inaccurate characterisation of these spheres, especially of the SE-EPI sequence due to the short final echo time and thus lower dynamic

### 3.3. Results

---

range. In the range of  $T_2$  reported in the kidney, the noise fit increased the average error over the four sequences.

The discard fit requires an empirical threshold to be chosen. If chosen correctly, this results in a slightly improved accuracy however, if the threshold was not correctly chosen the accuracy of  $T_2$  was compromised. While optimising the threshold is trivial when the known reference values are available, this is more difficult in-vivo and therefore, given the increase in accuracy was marginal and only effected spheres of short  $T_2$ , consistent results were deemed preferable.

The combination of discard and noise fit resulted in a decreased accuracy from the basic fit. Spheres that benefited from the additional noise term relax to their baseline noise quickly, however by discarding these echoes, the estimate of noise becomes inaccurate and thus so does the estimate of  $T_2$ .

It was therefore concluded that a basic fit should be used for all subsequent renal data.

#### 3.3.2 Phantom Verification

##### Accuracy

Each sequence was used to image the  $T_2$  array in the QalibreMD phantom. Figure 3.13 shows the measured  $T_2$  plot against the reference  $T_2$  for each method. All methods struggle to accurately measure the very short  $T_2$  spheres in the array with the CPMG  $T_2$  prep method faring best. The SE-EPI method overestimates short  $T_2$  spheres due to the first TE being sampled at 20 ms but is also underestimating long  $T_2$  because of its small range in TE. When considering only the spheres with physiologically similar  $T_2$  to the kidneys, the SE-EPI method is the most accurate with the GraSE and CPMG  $T_2$  prep delivering similar results. This is mirrored by the MRE shown in Table 3.3. Example  $T_2$  maps of the phantoms  $T_2$  array imaged with each sequence are

### 3.3. Results

---

shown in Figure 3.14.



Figure 3.13:  $T_2$  measured using each method compared to the reference  $T_2$  from literature. (a) The full range of  $T_2$  spheres is shown on logarithmic axis with the range of  $T_2$  reported in the kidneys shaded in red (b) The spheres with  $T_2$  in the range of the kidneys are shown on linear axis. (c) and (d) show the relative error of each sphere for the full and renal range of spheres respectively.

### 3.3. Results

Acquisition Method	MRE (5 ms – 650 ms) (%)	MRE (40 ms – 200 ms) (%)
SE-EPI	$36 \pm 34$	$8 \pm 5$
ME-TSE	$38 \pm 31$	$23 \pm 13$
GraSE	$32 \pm 29$	$15 \pm 4$
CPMG $T_2$ Prep	$18 \pm 15$	$11 \pm 1$

Table 3.3: MRE when measuring  $T_2$  of the QalibreMD phantom over different ranges using each sequence. 5 ms – 650 ms is the full range of  $T_2$  available in the phantom and 40 ms – 200 ms is the range of  $T_2$  expected in the kidneys.

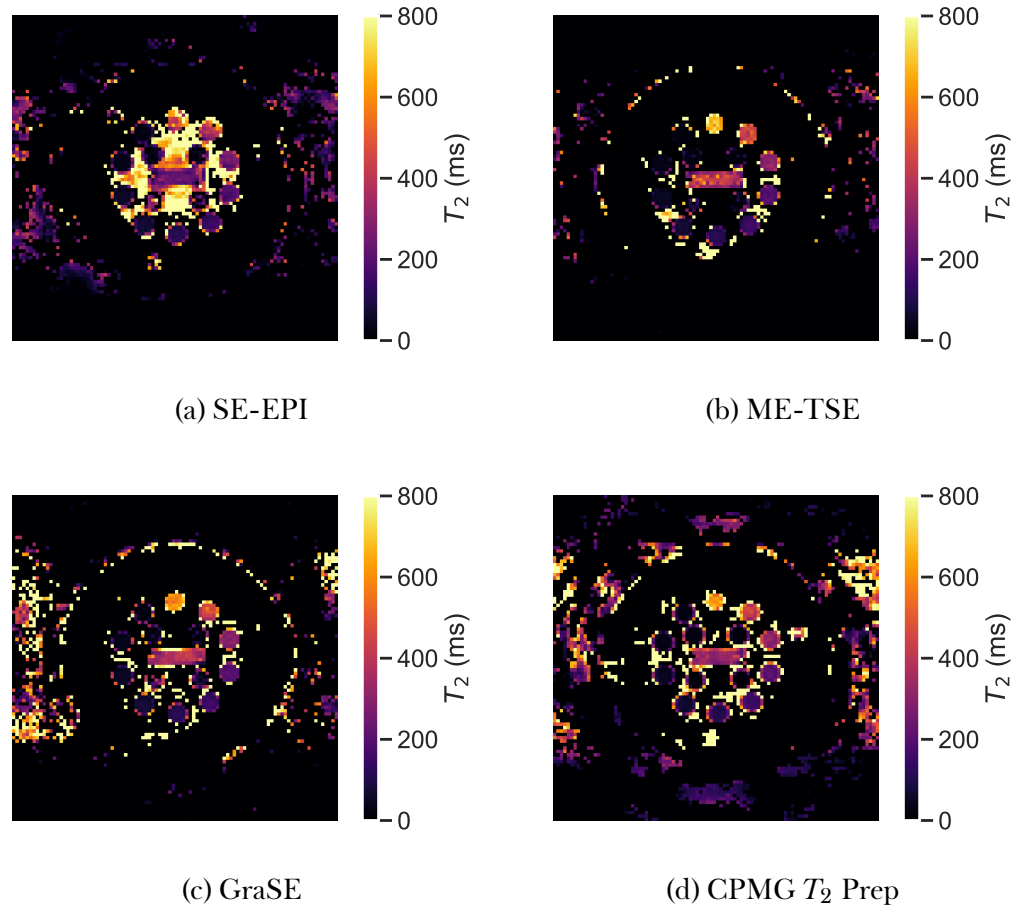


Figure 3.14:  $T_2$  maps of the QaliberMD system phantom  $T_2$  array generated using each sequence.

### 3.3. Results

---

#### Sensitivity to Flow

The simulated capillary bed of the flow phantom was imaged with the perfusate being pumped at rates from 0 to 350 mℓ/min. The absolute change in measured  $T_2$  is shown in Figure 3.15a and the change in  $T_2$  as a percentage of  $T_2$  measured when the pump was turned off is shown in Figure 3.15b. The  $T_2$  of the perfusate is relatively long and as such the inaccuracies measuring long  $T_2$  observed in the static phantom (Figure 3.13a and Figure 3.13c) manifest themselves here. This causes a large range in  $T_2$  even when the pump is turned off. In Figure 3.15b the SE-EPI sequence can be seen to be most sensitive to perfusion due to its largest deviation as flow rate increased, the GraSE sequence produced the minimum proportional change in  $T_2$  as the rate perfusate was pumped through the capillary bed was increased.

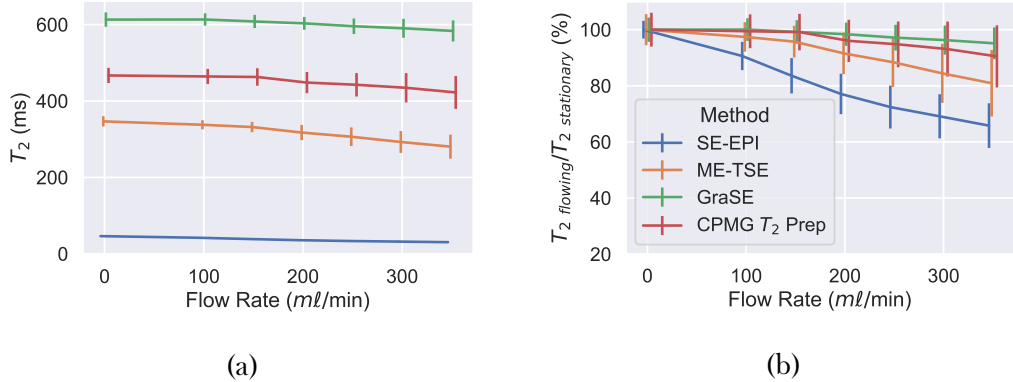


Figure 3.15: The effects of flow on measurements of  $T_2$  using each method. Points have been slightly staggered on the  $x$ -axis to aide the visibility of error bars. (a) Absolute measured  $T_2$ . (b) Change in  $T_2$  as a percentage of  $T_2$  measured at rest for each sequence.

The flow rate is measured at the pump, therefore the perfusate will not be travelling at the reported rate through the capillary bed. To quantify the movement of the perfusate using techniques widely available in the kidneys, Apparent Diffusion Coefficient (ADC) maps of the capillary bed were calculated at each flow rate, Figure 3.16.

### 3.3. Results

---



Figure 3.16: Changes in ADC as the rate perfusate is pumped through the simulated capillary bed is increased.

### Image Quality

Each sequence was slightly modified to contain a volume with TE 20 ms and used to image the orthogonal grid in the QalibreMD phantom, Figure 3.10. A high-resolution structural scan was then used to deconvolve an estimate of the PSF from each of the  $T_2$ -weighted images allowing the FWHM to be estimated, Table 3.4. Examples of the central slice of the grid imaged with each method are shown in Figure 3.17.

Acquisition Method	PSF FWHM (mm)
SE-EPI	$4.80 \pm 0.18$
ME-TSE	$4.20 \pm 0.14$
GraSE	$4.26 \pm 0.12$
CPMG $T_2$ Prep	$6.48 \pm 0.33$

Table 3.4: The FWHM of the estimated PSF for each acquisition method.

### 3.3. Results

---

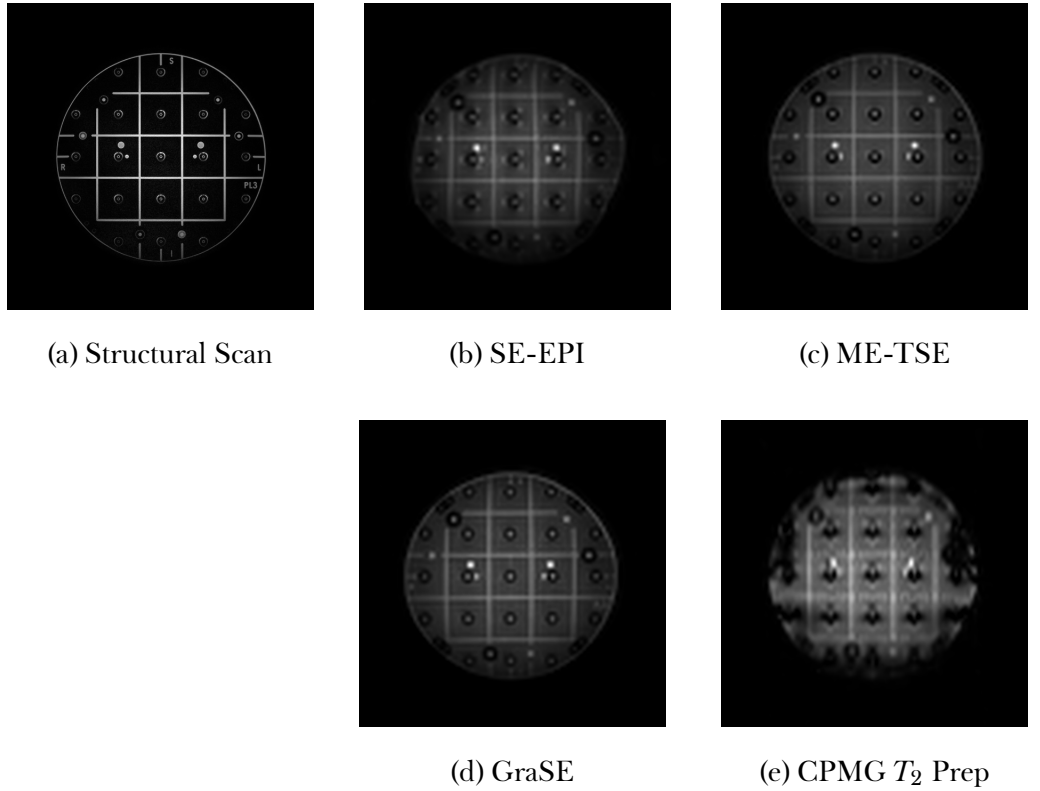


Figure 3.17: Examples of the orthogonal grid imaged with a TE of 20 ms using each sequence and the high-resolution structural scan used as the gold standard to be deconvolved from each  $T_2$ -weighted scan.

Both the SE-EPI and CPMG  $T_2$  prep sequences suffer from significant image distortions due to their EPI readout with the ME-TSE and GraSE both producing similar image quality and a comparable width of PSF.

#### 3.3.3 In-Vivo

Five healthy volunteers were imaged using each of the four methods. Example in-vivo maps are shown in Figure 3.18. The  $T_2$  measured using the SE-EPI method is much lower than when measured using each of the other three methods. The GraSE shows the largest contrast between cortex and medulla while the CPMG  $T_2$  prep suffers from image artefacts with the large amount of blurring measured on the phantom making the in-vivo data difficult to interpret.

### 3.3. Results

---



Figure 3.18: Example in-vivo maps generated using each of the sequences being compared including  $B_0$  and  $B_1$  maps used for quality control.

ROI for the cortex and medulla were defined from the  $T_1$ -weighted structural scan and these ROI used to calculate the mean  $T_2$  for each tissue using each mapping method. The mean across the five subjects is shown in Figure 3.19a. Additionally the Coefficient of Variation (CoV), defined as standard

### 3.3. Results

---

deviation upon the mean, between subjects was calculated to assess the repeatability of each measure, Figure 3.19b.



Figure 3.19: (a) Mean cortical and medullary  $T_2$  values across five subjects measured using each sequence. (b) The CoV between subjects measuring  $T_2$  using each of the sequences.

To better explore the variation between subjects, histograms of the  $T_2$  values of each tissue type were generated for each subject, Figure 3.20.

### 3.3. Results

---

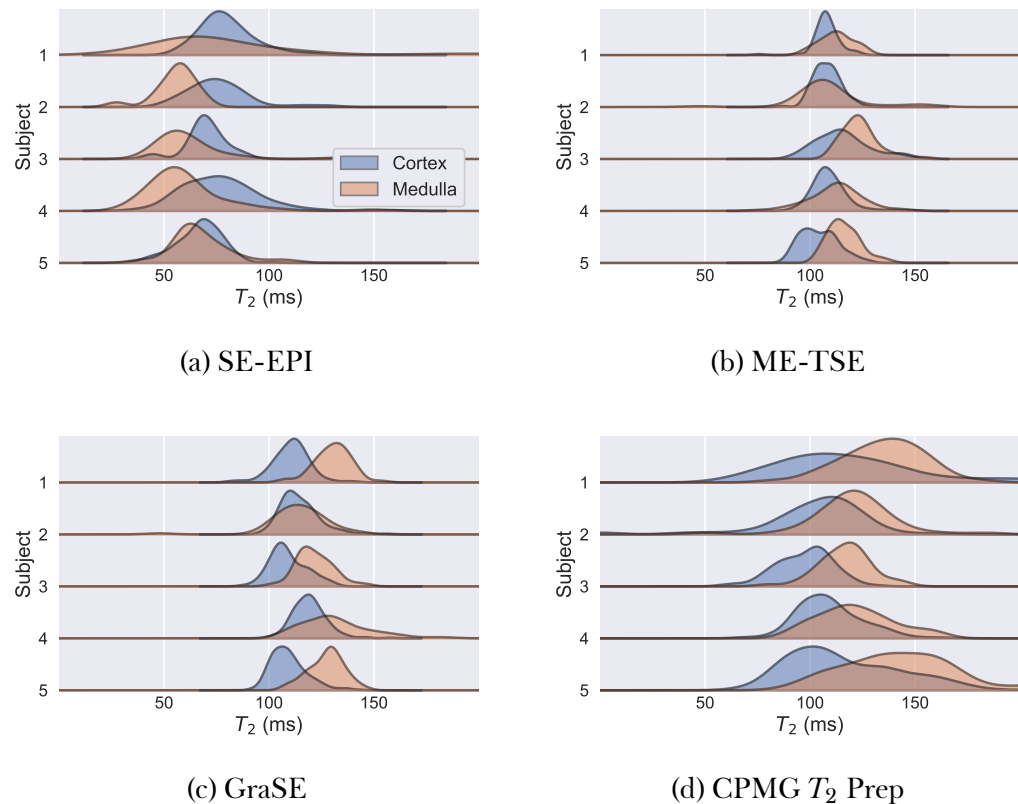


Figure 3.20: Histograms of the  $T_2$  of each tissue type for all subjects and mapping methods.

## 3.4 Discussion

In this chapter, four of the most common  $T_2$  mapping methods were optimised for use in the kidneys. These sequences were validated for quantitative accuracy, image quality and sensitivity to flow using phantoms before being used to image five healthy volunteers. Additionally, four different methods of fitting  $T_2$  maps from the subsequent raw data were compared.

Of the fitting methods explored, the basic fit was deemed the most appropriate. Over the range of  $T_2$  within the kidneys, fitting for a baseline noise term reduced the calculated  $T_2$  of longer  $T_2$  tissues because they had not fully recovered before the final TE and as such the noise term was over-estimated. This method would be more appropriate for use in tissues with a shorter  $T_2$  such as the liver or sequences with a very wide range of TE. Discarding TE with signal below an empirically derived threshold can result in an increased accuracy for short  $T_2$  tissues but does not improve the accuracy within the range of the kidneys. The discard threshold can be manually defined; however, this leads to potentially inaccurate results if a sub-optimum threshold is chosen, these inaccurate results can be difficult to identify in-vivo with no gold standard to compare against. An alternative to manually setting a threshold is to define a ROI over the liver, the signal from the final TE is then used to inform the estimation of the discard threshold as, in most cases due to its very short  $T_2$ , the liver will have fully recovered by the final TE. While this method does eliminate the manual aspect of threshold definition between subjects, it requires the additional manual processing step of delaminating an additional ROI for no increase inaccuracy within the kidneys. Discarding low intensity echoes and fitting for noise also produced inferior results to the basic fit. By discarding the late echo times that the fitting method uses to estimate noise, the  $\epsilon$  term becomes less accurate and as such, so does  $T_2$ . It was therefore concluded that the basic fit should be used for renal studies, however, the noise fit should be considered for liver  $T_2$  measurements.

The only sequence that was able to accurately estimate the  $T_2$  of the shortest

### 3.4. Discussion

---

$T_2$  spheres of the QalibreMD phantom was the CPMG  $T_2$  prep, Figure 3.13 and Table 3.3. This is because, it is able to achieve an effective echo time of 0 ms and thus sample the signal before it has decayed; for other sequences the first echo time can be multiple times the  $T_2$  of these short spheres and as such the signal has already decayed a large proportion of its initial signal. Additionally, the CPMG sequence is self-correcting for imperfect 180° pulses, and thus the longer TE are more accurate. It is the very large relative error of the shortest  $T_2$  spheres that leads to the unacceptable large MRE in the other sequences over the full range of  $T_2$  within the phantom, Figure 3.13c. Both the ME-TSE and GraSE yield similar accuracies over the range of  $T_2$  seen in the kidneys due to their rapid acquisition, initial TE much shorter than the  $T_2$  of the kidneys and, in the case of GraSE, short echo spacing and thus more TE to fit each voxel to. The SE-EPI sequence suffers due to being relatively slow, this is because the thick slice profile of the 180° pulse means that each TE needs to be collected in two packets with slices interleaved. As such only a limited number of TE can be acquired within the time limits prescribed and, without any of the more advance elements of the CPMG sequence its accuracy is compromised for  $T_2$  outside the central range of the kidneys.

From Figure 3.15b it can be observed that the SE-EPI sequence is most sensitive to flow due to its largest proportional change in measured  $T_2$  as the rate of flow is increased. The sequences with the lowest absolute  $T_2$  with the pump off are also the sequences that are effected most when the pump is turned on, this is because there are still effects of diffusion/flow even with the pump turned off and as such the  $T_2$  is still reduced. The ADC increases from  $1.15 \times 10^{-3} \pm 0.06 \times 10^{-3}$  mm<sup>2</sup>/s to  $1.36 \times 10^{-3} \pm 0.09 \times 10^{-3}$  mm<sup>2</sup>/s over the full range of flow rates the pump can produce, Figure 3.16, corresponding to an increase of 17% therefore it is expected that there will still be considerable confounding influences of diffusion on the  $T_2$  mapping sequences when the pump is turned off. This is also a contributing factor in the large range in  $T_2$  observed when the pump was turned off in Figure 3.15a. The GraSE sequence is least sensitive to flow with only a 5% decrease in  $T_2$ . This is due to the GraSE sequences short echo spacing and the fact multiple

### 3.4. Discussion

---

TE are collected within the same Repetition Time (TR), as such, the effects of diffusion are not consistent across TE and do not produce a diffusion weighting proportional to the  $T_2$  weighting.

The large amount of blurring of the CPMG  $T_2$  prep sequence limits its readability in-vivo and is due to the high EPI factor leading to an increased acquisition voxel size. The degree of blurring measured in the other three sequences was comparable with the SE-EPI having a slightly broader PSF.

The phantom evaluation of each sequence is summarised in Figure 3.21. This figure combines the quantitative accuracy of  $T_2$  within the range of the kidneys, the sensitivity to fluid motion and blurring characteristics of each sequence. The GraSE and CPMG  $T_2$  prep sequences produce the most accurate results, however the GraSE has a much smaller PSF.

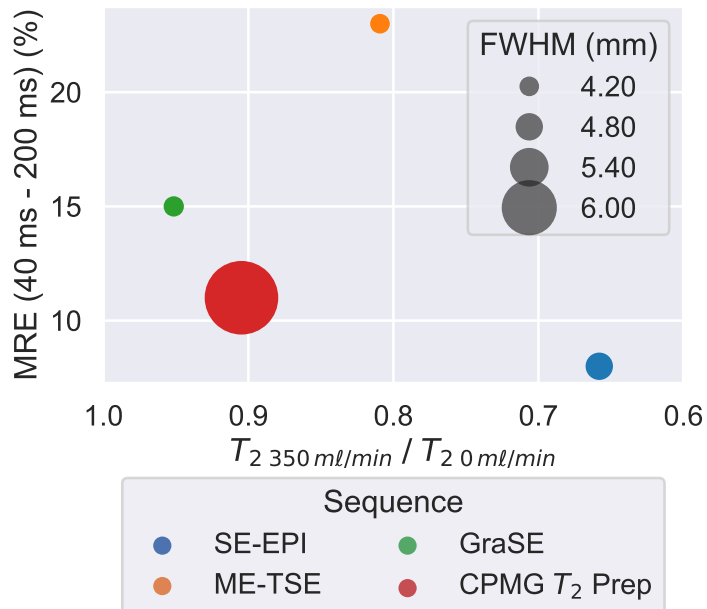


Figure 3.21: A summary of the quantitative accuracy, sensitivity to flow and degree of blurring observed for each  $T_2$  mapping sequence when evaluated on phantoms.

Comparing the in-vivo data in Figure 3.18 and Figure 3.19 it can be seen that the relative strengths and weaknesses of each sequence observed in the phantoms are mirrored in-vivo. The SE-EPI sequence is estimating much

### 3.4. Discussion

---

shorter  $T_2$  than the other three sequences. Additionally, this sequence results in a shorter  $T_2$  in the medulla than the cortex, this was also observed by de Bazelaire et al [31] and is somewhat surprising given the perfusion of the renal cortex is higher than the medulla [3, 49], yet in Figure 3.15 it was observed that measured  $T_2$  decreases as flow increases. This is most likely caused by a difference in the direction of flow between the phantom and the medulla. In the flow phantom the perfusate flows radially in from the circumference of the porous media towards the outlet at the centre. This results in a predominantly in-plain flow, whereas in the kidney, the renal vein quickly ascends to the inferior vena cava and is thus out-of-plain. This out-of-plain flow means that for longer TE, some protons have travelled out of the profile of the  $180^\circ$  refocusing pulse and as such do not contribute to the signal. This effect manifests itself more at longer TE and thus the measured  $T_2$  decreases. The SE-EPI sequence also appears to be the most sensitive to  $B_1$  inhomogeneity. A relatively large difference in  $T_2$  is observed between the left and right kidneys, this matches the pattern of  $B_1$  seen in Figure 3.18f. These factors combine and lead to the SE-EPI sequence having the largest CoV between subjects of the sequences tested.

The ME-TSE sequence produces reasonable images and broadly similar mean  $T_2$  to the GraSE and CPMG  $T_2$  prep for the cortex however the mean  $T_2$  measured in the medulla is lower therefore little contrast is seen between the cortex and medulla. The image quality and CoV produced by the GraSE sequence is similar to that of the ME-TSE which is expected given the comparable PSF and similar sequence architecture. The GraSE measures higher medullary  $T_2$  than the ME-TSE resulting in greater corticomedullary contrast; this increased contrast can be observed across subjects, Figure 3.20c. The GraSE sequence has the highest Specific Absorption Rate (SAR) and makes the most intimidating noises of the four sequences (sounding like an alarm). The SAR is well below safety limits, however these factors may be a consideration when scanning nervous subjects as heating can be felt. The effects of the wide PSF can be seen in the image produced by CPMG  $T_2$  prep with a large amount of blurring decreasing the readability of the image.

### 3.4. Discussion

---

The mean  $T_2$  of the cortex and medulla are similar to that measured using the GraSE sequence, however due to the inferior image quality, the variance within the ROI is much higher, Figure 3.20d.

Sequence	Acquisition Time (before respiratory compensation)	MRE (5 ms - 650 ms) (%)	MRE (40 ms - 200 ms) (%)	FWHM (mm)	Sensitivity to Flow	In-Vivo CoV (cortex/medulla) (%)	In-Vivo Comments
SE-EPI	3 min 0 sec	36 ± 34	8 ± 5	4.80 ± 0.18	0.65 ± 0.08	7.17/13.57	Inaccurate Sensitive to $B_1$
ME-TSE	1 min 57 sec	38 ± 31	23 ± 13	4.20 ± 0.14	0.81 ± 0.12	3.73/5.04	Reduced corticomedullary contrast
GraSE	2 min 6 sec	32 ± 29	15 ± 4	4.26 ± 0.12	0.95 ± 0.06	3.86/5.73	High SAR
CPMG $T_2$ Prep	2 min 23 sec	18 ± 15	11 ± 1	6.48 ± 0.33	0.90 ± 0.11	8.08/8.62	Large degree of image distortion

Table 3.5: A summary of the results both in phantoms and in-vivo.

Having compared the quantitative accuracy, image quality and acquisition time of four common  $T_2$  mapping sequences on phantoms and in-vivo for use in the kidneys, Table 3.5, it is concluded that the GraSE sequence provides the optimum protocol for renal  $T_2$  mapping. In phantoms, the accuracy was shown to be comparable with the ME-TSE sequence and its superior in-vivo image quality and insensitivity to flow lead us to recommend this sequence for further renal studies.

## 3.5 Conclusion

A SE-EPI, ME-TSE, GraSE and CPMG  $T_2$  prep sequence were used to image phantoms to assess their accuracy when quantifying  $T_2$ , sensitivity to flow and image quality by estimating the PSF. These sequences were then used to acquire  $T_2$  maps of the kidneys of five healthy volunteers.

The GraSE sequence is recommended for future renal studies due to its superior image quality and accuracy within the time constraints.

All acquisition presented here was carried out on a Philips system. Going forward these methods should be evaluated on other vendors to enable a better comparison of results between sites.

## 3.6 Acknowledgements

We are grateful for access to the University of Nottingham's Augusta high performance computing service.

### 3.7 References

1. Daniel, A. J., Cox, E., Buchanan, C. & Francis, S. *A Comparison of T2 Mapping Methods in the Kidneys* in *Proc. Intl. Soc. Mag. Reson. Med.* 28 International Society of Magnetic Resonance in Medicine Annual Meeting (Online, Aug. 2020).
2. Tofts, P. *Quantitative MRI of the Brain: Measuring Changes Caused by Disease* 688 pp. Google Books: RbFrAAAAMAAJ (Wiley, 2003).
3. Buchanan, C. E., Mahmoud, H., Cox, E. F., McCulloch, T., Prestwich, B. L., Taal, M. W., Selby, N. M. & Francis, S. T. Quantitative Assessment of Renal Structural and Functional Changes in Chronic Kidney Disease Using Multi-Parametric Magnetic Resonance Imaging. *Nephrology Dialysis Transplantation*. doi:10.1093/ndt/gfz129 (29th June 2019).
4. Chapman, A. B. *et al.* Kidney Volume and Functional Outcomes in Autosomal Dominant Polycystic Kidney Disease. *Clinical Journal of the American Society of Nephrology* **7**, 479–486 (1st Mar. 2012).
5. Gong, I. H., Hwang, J., Choi, D. K., Lee, S. R., Hong, Y. K., Hong, J. Y., Park, D. S. & Jeon, H. G. Relationship Among Total Kidney Volume, Renal Function and Age. *The Journal of Urology* **187**, 344–349 (Jan. 2012).
6. Bull, S. *et al.* Human Non-Contrast T1 Values and Correlation with Histology in Diffuse Fibrosis. *Heart* **99**, 982–987 (1st July 2013).
7. Ferreira, V. M. *et al.* T1 Mapping for the Diagnosis of Acute Myocarditis Using CMR: Comparison to T2-Weighted and Late Gadolinium Enhanced Imaging. *JACC: Cardiovascular Imaging* **6**, 1048–1058 (1st Oct. 2013).
8. Hoad, C. L. *et al.* A Study of T1 Relaxation Time as a Measure of Liver Fibrosis and the Influence of Confounding Histological Factors. *NMR in Biomedicine* **28**, 706–714 (2015).
9. Luetkens, J. A. *et al.* Quantification of Liver Fibrosis at T1 and T2 Mapping with Extracellular Volume Fraction MRI: Preclinical Results. *Radiology* **288**, 748–754 (26th June 2018).

### 3.7. References

---

10. Friedli, I. *et al.* New Magnetic Resonance Imaging Index for Renal Fibrosis Assessment: A Comparison between Diffusion-Weighted Imaging and T1 Mapping with Histological Validation. *Scientific Reports* **6**. doi:10.1038/srep30088. pmid: 27439482 (21st July 2016).
11. Gillis, K. A. *et al.* Non-Contrast Renal Magnetic Resonance Imaging to Assess Perfusion and Corticomedullary Differentiation in Health and Chronic Kidney Disease. *Nephron* **133**, 183–192 (2016).
12. Cox, E. F., Buchanan, C. E., Bradley, C. R., Prestwich, B., Mahmoud, H., Taal, M., Selby, N. M. & Francis, S. T. Multiparametric Renal Magnetic Resonance Imaging: Validation, Interventions, and Alterations in Chronic Kidney Disease. *Frontiers in Physiology* **8**. doi:10.3389/fphys.2017.00696 (2017).
13. Hueper, K. *et al.* Functional MRI Detects Perfusion Impairment in Renal Allografts with Delayed Graft Function. *American Journal of Physiology-Renal Physiology* **308**, F1444–F1451 (29th Apr. 2015).
14. Artz, N. S., Sadowski, E. A., Wentland, A. L., Grist, T. M., Seo, S., Djamali, A. & Fain, S. B. Arterial Spin Labeling MRI for Assessment of Perfusion in Native and Transplanted Kidneys. *Magnetic Resonance Imaging* **29**, 74–82 (1st Jan. 2011).
15. Ren, T. *et al.* Evaluation of Renal Allografts Function Early after Transplantation Using Intravoxel Incoherent Motion and Arterial Spin Labeling MRI. *Magnetic Resonance Imaging* **34**, 908–914 (1st Sept. 2016).
16. Niles, D. J., Artz, N. S., Djamali, A., Sadowski, E. A., Grist, T. M. & Fain, S. B. Longitudinal Assessment of Renal Perfusion and Oxygenation in Transplant Donor-Recipient Pairs Using ASL and BOLD MRI. *Investigative radiology* **51**, 113–120 (Feb. 2016).
17. Rossi, C., Artunc, F., Martirosian, P., Schlemmer, H.-P., Schick, F. & Boss, A. Histogram Analysis of Renal Arterial Spin Labeling Perfusion Data Reveals Differences Between Volunteers and Patients With Mild Chronic Kidney Disease. *Investigative Radiology* **47**, 490–496 (Aug. 2012).

### 3.7. References

---

18. Tan, H., Koktzoglou, I. & Prasad, P. V. Renal Perfusion Imaging with Two-Dimensional Navigator Gated Arterial Spin Labeling. *Magnetic Resonance in Medicine* **71**, 570–579 (2014).
19. Eckerbom, P., Hansell, P., Cox, E., Buchanan, C., Weis, J., Palm, F., Francis, S. & Liss, P. Multiparametric Assessment of Renal Physiology in Healthy Volunteers Using Noninvasive Magnetic Resonance Imaging. *American Journal of Physiology-Renal Physiology* **316**, F693–F702 (16th Jan. 2019).
20. Schley, G., Jordan, J., Ellmann, S., Rosen, S., Eckardt, K.-U., Uder, M., Willam, C. & Bäuerle, T. Multiparametric Magnetic Resonance Imaging of Experimental Chronic Kidney Disease: A Quantitative Correlation Study with Histology. *PLOS ONE* **13**, e0200259 (16th July 2018).
21. Hueper, K. *et al.* Kidney Transplantation: Multiparametric Functional Magnetic Resonance Imaging for Assessment of Renal Allograft Pathophysiology in Mice. *Investigative Radiology* **51**, 58–65 (Jan. 2016).
22. Gouya, H., Vignaux, O., Le Roux, P., Chanson, P., Bertherat, J., Bertagna, X. & Legmann, P. Rapidly Reversible Myocardial Edema in Patients with Acromegaly: Assessment with Ultrafast T2 Mapping in a Single-Breath-Hold MRI Sequence. *American Journal of Roentgenology* **190**, 1576–1582 (1st June 2008).
23. Giri, S., Chung, Y.-C., Merchant, A., Mihai, G., Rajagopalan, S., Raman, S. V. & Simonetti, O. P. T2 Quantification for Improved Detection of Myocardial Edema. *Journal of Cardiovascular Magnetic Resonance* **11**, 56 (30th Dec. 2009).
24. Naßenstein, K., Nensa, F., Schlosser, T., Bruder, O., Umuthlu, L., Lauenstein, T., Maderwald, S. & Ladd, M. E. Cardiac MRI: T2-Mapping Versus T2-Weighted Dark-Blood TSE Imaging for Myocardial Edema Visualization in Acute Myocardial Infarction. *RöFo - Fortschritte auf dem Gebiet der Röntgenstrahlen und der bildgebenden Verfahren* **186**, 166–172 (Feb. 2014).

### 3.7. References

---

25. Guo, H. *et al.* Myocardial T2 Quantitation in Patients with Iron Overload at 3 Tesla. *Journal of Magnetic Resonance Imaging* **30**, 394–400 (2009).
26. Krittayaphong, R., Zhang, S., Saiviroonporn, P., Viprakasit, V., Tanapibunpon, P., Komoltri, C. & Wangworatrakul, W. Detection of Cardiac Iron Overload with Native Magnetic Resonance T1 and T2 Mapping in Patients with Thalassemia. *International Journal of Cardiology* **248**, 421–426 (1st Dec. 2017).
27. Neema, M., Stankiewicz, J., Arora, A., Dandamudi, V. S. R., Batt, C. E., Guss, Z. D., Al-Sabbagh, A. & Bakshi, R. T1- and T2-Based MRI Measures of Diffuse Gray Matter and White Matter Damage in Patients with Multiple Sclerosis. *Journal of Neuroimaging* **17**, 16S–21S (2007).
28. Rugg-Gunn, F. J., Boulby, P. A., Symms, M. R., Barker, G. J. & Duncan, J. S. Whole-Brain T2 Mapping Demonstrates Occult Abnormalities in Focal Epilepsy. *Neurology* **64**, 318–325 (25th Jan. 2005).
29. Knight, M. J., McCann, B., Tsivos, D., Dillon, S., Coulthard, E. & Kauppinen, R. A. Quantitative T2 Mapping of White Matter: Applications for Ageing and Cognitive Decline. *Physics in Medicine and Biology* **61**, 5587–5605 (July 2016).
30. Vymazal, J., Righini, A., Brooks, R. A., Canesi, M., Mariani, C., Leonardi, M. & Pezzoli, G. T1 and T2 in the Brain of Healthy Subjects, Patients with Parkinson Disease, and Patients with Multiple System Atrophy: Relation to Iron Content. *Radiology* **211**, 489–495 (1st May 1999).
31. De Bazeilaire, C. M. J., Duhamel, G. D., Rofsky, N. M. & Alsop, D. C. MR Imaging Relaxation Times of Abdominal and Pelvic Tissues Measured in Vivo at 3.0 T: Preliminary Results. *Radiology* **230**, 652–659 (1st Mar. 2004).
32. Zhang, J. L. *et al.* Reproducibility of R2\* and R2 Measurements in Human Kidneys in Proc. Intl. Soc. Mag. Reson. Med. 19 ISMRM. **19** (2011), 2954.
33. Li, X., Bolan, P. J., Ugurbil, K. & Metzger, G. J. Measuring Renal Tissue Relaxation Times at 7 T. *NMR in Biomedicine* **28**, 63–69 (2015).

### 3.7. References

---

34. De Boer, A. *et al.* Multiparametric Renal MRI: An Intrasubject Test–Retest Repeatability Study. *Journal of Magnetic Resonance Imaging* **n/a**. doi:10.1002/jmri.27167 (16th Apr. 2020).
35. Mathys, C., Blondin, D., Wittsack, H.-J., Miese, F. R., Rybacki, K., Walther, C., Holstein, A. & Lanzman, R. S. T2' Imaging of Native Kidneys and Renal Allografts – a Feasibility Study. *RöFo - Fortschritte auf dem Gebiet der Röntgenstrahlen und der bildgebenden Verfahren* **183**, 112–119 (Feb. 2011).
36. Adams, L. C. *et al.* Multiparametric Assessment of Changes in Renal Tissue after Kidney Transplantation with Quantitative MR Relaxometry and Diffusion-Tensor Imaging at 3 T. *Journal of Clinical Medicine* **9**, 1551 (5 May 2020).
37. Franke, M. *et al.* Magnetic Resonance T2 Mapping and Diffusion-Weighted Imaging for Early Detection of Cystogenesis and Response to Therapy in a Mouse Model of Polycystic Kidney Disease. *Kidney International* **92**, 1544–1554 (1st Dec. 2017).
38. Adams, L. C. *et al.* Use of Quantitative T2 Mapping for the Assessment of Renal Cell Carcinomas: First Results. *Cancer Imaging* **19**, 35 (7th June 2019).
39. Petzold, K. *et al.* Building a Network of ADPKD Reference Centres across Europe: The EuroCYST Initiative. *Nephrology Dialysis Transplantation* **29**, iv26–iv32 (suppl\_4 1st Sept. 2014).
40. Will, S., Martirosian, P., Würslin, C. & Schick, F. Automated Segmentation and Volumetric Analysis of Renal Cortex, Medulla, and Pelvis Based on Non-Contrast-Enhanced T1- and T2-Weighted MR Images. *Magnetic Resonance Materials in Physics, Biology and Medicine* **27**, 445–454 (1st Oct. 2014).
41. Carr, H. Y. & Purcell, E. M. Effects of Diffusion on Free Precession in Nuclear Magnetic Resonance Experiments. *Physical Review* **94**, 630–638 (1st May 1954).

### 3.7. References

---

42. Meiboom, S. & Gill, D. Modified Spin-Echo Method for Measuring Nuclear Relaxation Times. *Review of Scientific Instruments* **29**, 688–691 (1st Aug. 1958).
43. Daniel, A. J. *et al.* UKRIN Kidney Analysis Toolbox (UKAT): A Framework for Harmonized Quantitative Renal MRI Analysis in Proc. Intl. Soc. Mag. Reson. Med. 28 International Society of Magnetic Resonance in Medicine Annual Meeting. **29** (Online, May 2021), 2379.
44. Nery, F., Daniel, A. J., Sousa, J. & Buchanan, C. *UKRIN Kidney Analysis Toolbox* version v0.1.0. UK Renal Imaging Network, Dec. 2020.
45. Wolf, M. *et al.* Magnetic Resonance Imaging T1- and T2-Mapping to Assess Renal Structure and Function: A Systematic Review and Statement Paper. *Nephrology Dialysis Transplantation* **33**, ii41–ii50 (suppl\_2 1st Sept. 2018).
46. Chaimow, D. & Shmuel, A. A More Accurate Account of the Effect of K-Space Sampling and Signal Decay on the Effective Spatial Resolution in Functional MRI. *bioRxiv*, 097154 (17th Sept. 2017).
47. Chaimow, D. & Shmuel, A. *A More Accurate Account of the Effect of K-Space Sampling and Signal Decay on the Effective Spatial Resolution in Functional MRI* in Proc. Intl. Soc. Mag. Reson. Med. 25 International Society of Magnetic Resonance in Medicine Annual Meeting. **25** (Honolulu, Hawai'i, USA, Apr. 2017), 5240.
48. MRIStandards. *MRIStandards/PhantomViewer* 20th Dec. 2020.
49. Nery, F. *et al.* Consensus-Based Technical Recommendations for Clinical Translation of Renal ASL MRI. *Magnetic Resonance Materials in Physics, Biology and Medicine* **33**, 141–161 (1st Feb. 2020).

## **Chapter 4**

# **Quantitative Methods to Measure Renal Oxygenation**

---

## Abstract

Measurements of oxygenation of blood entering and leaving the kidneys would be a highly desirable quantitative biomarker allowing the calculation of renal metabolic rate of oxygen. Two methods of measuring blood oxygen saturation using MRI have been developed for use in the brain, Susceptibility Based Oximetry (SBO) and  $T_2$  Relaxation Under Spin Tagging (TRUST).

Here both methods are tailored for use in the abdomen, these modified sequences are compared to their unmodified counterparts in the controlled environment of the brain, verifying that the modifications do not affect the quantitative accuracy. The methods are then applied to measure oxygenation in the renal vein. The geometry of the renal vessels leads to a high degree of uncertainty when applying SBO however TRUST produced results concordant with literature.

To verify the TRUST was able to measure a change in renal oxygenation, a hyperoxia challenge was undertaken. Measurements of oxygen saturation in the renal vein were collected using TRUST and BOLD  $T_2^*$  maps, the current standard for assessing renal oxygenation, were collected while the subject was breathing room air, then pure oxygen. A  $16 \pm 3\%$  increase in oxygenation was measured using TRUST whereas no significant difference in  $T_2^*$  was measured.

This work was presented as an aural presentation at the International Society of Magnetic Resonance in Medicine (ISMRM) 26th Annual Meeting (2018) [1].

## 4.1 Introduction

As part of a multi-parametric quantitative Magnetic Resonance Imaging (MRI) protocol, Section 1.2, properties such as haemodynamics, oxygenation, and microstructure are assessed in a single 45 minute scanning session [2, 3]. Currently oxygenation is assessed using Blood Oxygen Level Dependent (BOLD)  $T_2^*$  maps to measure oxygenation of different tissues within the kidney, predominately the separation in mean  $T_2^*$  between the renal cortex and medulla, an example of which is shown in Figure 4.1. These BOLD  $T_2^*$  maps are, however, affected by other factors such as susceptibility effects, shimming and baseline blood flow and thus may be limited in their ability to draw quantitative conclusions despite their widespread use [4, 5].



Figure 4.1: An example  $T_2^*$  map. A clear difference can be seen between the renal medulla and cortex.

A welcome addition to this multi-parametric model would be the assessment of Renal Metabolic Rate of Oxygen (RMRO<sub>2</sub>); a measure analogous to the Cerebral Metabolic Rate of Oxygen (CMRO<sub>2</sub>) [6]. This measure can be calculated via Equation (4.1),

$$\text{RMRO}_2 = (Y_a - Y_v) \times \text{RBF} \times [\text{Hct}] \quad (4.1)$$

where  $Y_a$  and  $Y_v$  are arterial and venous oxygen saturation respectively, RBF is renal blood flow (in  $\text{mL}/\text{min}$ ) and Hct is the ratio of the volume of erythro-

#### 4.1. Introduction

---

cytes to the volume of the rest of the blood, known as haematocrit. RBF can be measured relatively easily using Phase Contrast (PC)-MRI [7] and Hct is usually taken to be 0.41 for healthy adults but can be measured from a simple blood test [8, 9] or using the correlation between  $T_1$  of blood and its haematocrit [10]. This means that only a measurement of blood oxygen saturation via a non-invasive protocol is required to generate a quantitative value of RMRO<sub>2</sub>.

Blood oxygen saturation can be measured precisely via the insertion of catheters into the subject, however this is clearly an invasive process [11]. There are currently two well established methods of measuring blood oxygenation via MRI however, thus far, these techniques have only been used to measure oxygen saturation in the sagittal sinus, a prominent vein in the brain. These methods are  $T_2$  Relaxation Under Spin Tagging (TRUST) [12–15] and Susceptibility Based Oximetry (SBO) [16–19]. TRUST builds on the ideas of an Arterial Spin Labelling (ASL) sequence in the fact that by subtracting control images from labelled images only blood is imaged. However, instead of labelling a slab of tissue in the neck and imaging a superior slice, when implementing TRUST the imaging plane is inferior to the labelled slab. By collecting a series of pairs of labelled and control images with different  $T_2$  weightings it is possible to fit the data from the sagittal sinus to a  $T_2$  relaxation and use a calibration curve to convert the value of  $T_2$  to venous oxygenation [20]. SBO is based upon the differences in magnetic susceptibility between the blood and the surrounding tissue. Using a phase map it is possible to model this difference in susceptibility and using the known difference in susceptibility between fully oxygenated blood and fully deoxygenated blood, venous oxygenation can be calculated.

Here both of the above techniques are applied to study oxygenation in the renal vein in young healthy individuals to assess the technicalities of transferring these protocols from the brain to the body. Given that these techniques have already been used in the brain with a number of studies in the literature, the sequences are first implemented on the brain to assess oxygenation in the

#### **4.1. Introduction**

---

superior sagittal sinus, then adapted to work within the more challenging environment of applications within the abdomen. These adapted sequences are compared to the results gained using the established techniques in the brain before testing on the renal vein. An oxygen challenge is carried out to verify that changes in oxygenation can be measured in the renal vein. If proved successful these sequences will be incorporated into the multi-parametric renal MRI protocol.

## 4.2 Methods

Imaging was performed on a whole body 3 Tesla MRI scanner (Ingenia, Philips Medical Systems, The Netherlands) using a 32 channel head or body coil. Studies were carried out according to the principles of the Declaration of Helsinki and approved by either the Local Ethics Committee or the East Midlands Research Ethics Committee. Written informed consent was obtained from all subjects.

### 4.2.1 Susceptibility-Based Oximetry

#### MRI Protocol

The principle behind SBO is based on the fact that there is a difference in magnetic susceptibility between the blood within a vessel and the tissue surrounding it [21]. As outlined by Jain, if a blood vessel is modelled as a long paramagnetic cylinder, it is possible to calculate the oxygenation of the blood by knowing the phase difference between blood in the vessel and the surrounding tissue, the angle of the vessel to the  $B_0$  field, the echo time of the scan and the subject's haematocrit [16]. This relationship is given by,

$$Y_v = \left[ 1 - \frac{2|\Delta\phi|}{\gamma TE \Delta \chi_{do} B_0 (\cos^2 \theta - 1/3) Hct} \right] \times 100, \quad (4.2)$$

where  $\Delta\phi$  is the average phase difference between the blood in the vessel and the surrounding tissue,  $\gamma$  is the gyromagnetic ratio of a proton, TE is the echo time,  $\Delta\chi_{do}$  is the susceptibility difference between fully deoxygenated and fully oxygenated blood ( $4\pi \times 0.27$ p.p.m) [22, 23],  $B_0$  is the static field strength,  $\theta$  is the angle of the vessel to the  $B_0$  field and Hct is the subjects haematocrit. Given haematocrit can be assumed or is measured with a blood test or by measuring the  $T_1$  of the blood, this means that from a simple phase map it is possible to calculate  $Y_v$ . The optimum phase map for this purpose was produced using a 2D  $T_1$  weighted Fast Field Echo (FFE) sequence with a

## 4.2. Methods

---

flip angle of  $25^\circ$ , flow compensation, coil homogeneity correction and flyback. The Field Of View (FOV) was  $230 \times 184 \times 29$  mm, matrix size of  $400 \times 300$ , Repetition Time (TR) of 12 ms, Echo Time (TE) of 7.5 ms and three signal averages. This led to a total acquisition time of 9 seconds and as such could be completed in a single breath hold if required.

### Analysis

Once the phase map has been acquired, a Region Of Interest (ROI) containing the superior sagittal sinus was defined. This mask was then dilated with concentric shells to generate the two ROI shown in Figure 4.2, note that the outer ROI has been constrained to within the brain during its dilation. There were no occurrences of phase wrapping in or immediately surrounding the superior sagittal sinus observed due to its small size and the high field homogeneity within the head and of the 3T scanner used. Any occurrences of phase wrapping could easily be corrected using Phase Region Expanding Labeller for Unwrapping Discrete Estimates (PRELUDE), a tool within fMRIB Software Library (FSL) (fMRIB, The University of Oxford) [24]. The average values of phase within these two ROI along with the angle of the vessel to the  $B_0$  field, as calculated from the localisation scans can then be used with Equation (4.2) to calculate  $Y_v$ .

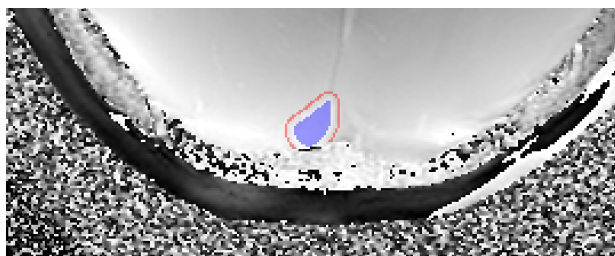


Figure 4.2: The region of interest averaged to find the intra-vascular phase (blue) and the region of interest used to find the phase of the surrounding tissue (red).

### 4.2.2 $T_2$ Relaxation Under Spin Tagging

#### MRI Protocol

The protocol for the TRUST MRI sequence in the brain involves the acquisition of a series of paired images using the pulse sequence shown in Figure 4.3a. A series of presaturation pulses using the Water suppression Enhanced through  $T_1$  effects (WET) scheme are applied to the imaging slice, shown in Figure 4.3b, to reduce the signal from static tissue and reduce contamination of the magnetisation in the imaging slice by an imperfect labelling slab profile [25, 26]. In the first of each image pair, a labelling pulse is applied consisting of two successive slice-selective  $90^\circ$  Radio Frequency (RF) pulses to generate a  $180^\circ$  label. The next image in the sequence has a control pulse applied to it instead of a labelling pulse, in this image the second of the  $90^\circ$  pulses is applied  $180^\circ$  out of phase to give zero net effect. As such any effects of magnetisation transfer related signal in the stationary tissue can be cancelled out because the net RF effect on the macromolecular spin magnetization is identical for both the labelling pulse and control pulse. This method of labelling is known as Transfer Insensitive Labelling Technique (TILT) and is widely used in literature for labelling in TRUST in the brain [27]. A series of non-selective  $T_2$  preparation pulses are then applied to minimise the blood outflow effect and modulate the  $T_2$  weighting of the image as in the Carr-Purcell-Meiboom-Gill (CPMG) sequence in Chapter 8, the time between the application of the labelling pulse and the  $T_2$  preparation is known as the Post Label Delay (PLD). Finally a  $90^\circ$  excitation pulse is applied followed by a standard Echo Planar Imaging (EPI) readout at time TE later [13]. If the control image is subtracted from the labelled image then only the venous blood that flowed from the labelled slab to the imaging slice will be visible, as shown in Figure 4.4.

## 4.2. Methods

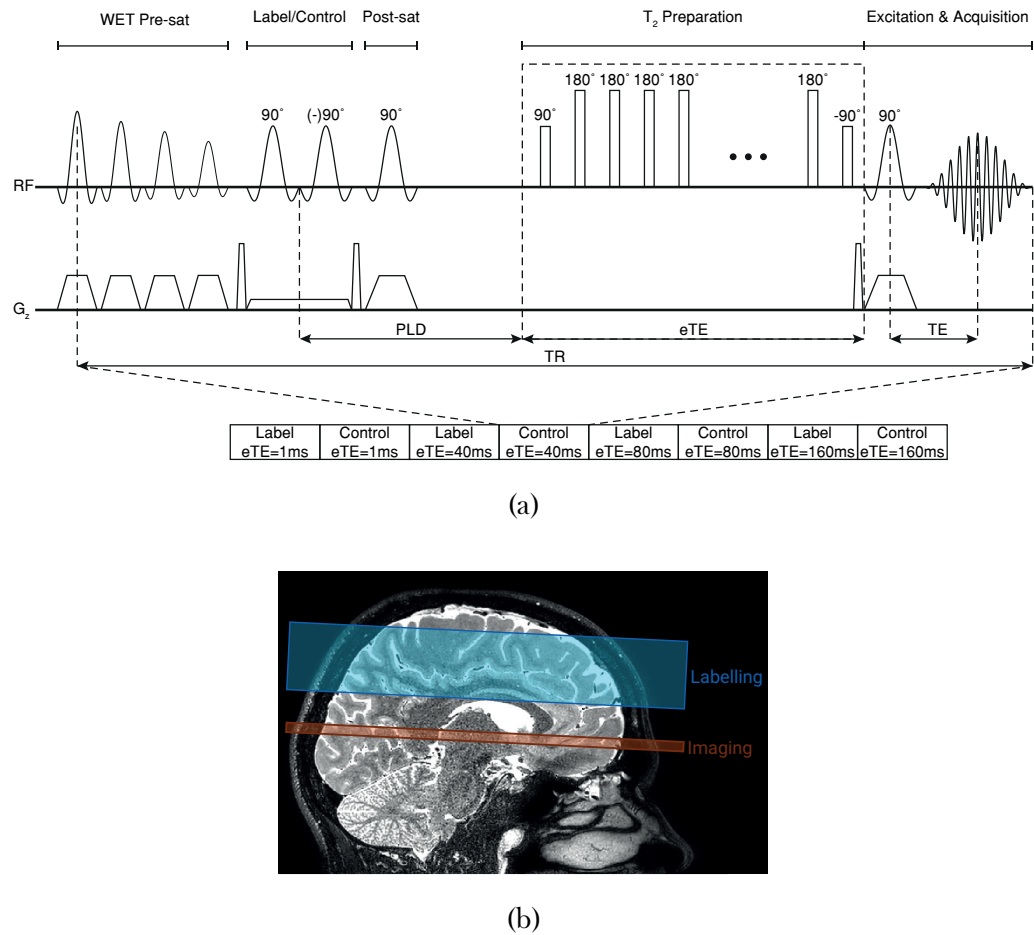


Figure 4.3: (a) The pulse sequence for TRUST MRI using the TILT labelling sequence. (b) The labelling and imaging volumes used for TILT tagging within the brain.

## 4.2. Methods

---



Figure 4.4: The control image, (a), is subtracted from the labelled image, (b), to generate a difference image, (c), of only the tagged blood.

This process is then repeated for another pair of images, however, this time the duration of the  $T_2$  preparation is increased to a larger Effective Echo Time (eTE), this applies a  $T_2$  weighting to the image in addition to the constant weighting caused by the regular TE. Three label/control image pairs were acquired with each eTE of 1 ms, 40 ms, 80 ms and 160 ms.

The resulting signal in the superior sagittal sinus of the difference between the labelled image and control image,  $\Delta S$ , is defined by Equation (4.3)

$$\begin{aligned}
 \Delta S &= S_{\text{label}} - S_{\text{control}} \\
 &= S_{\text{blood label}} - S_{\text{blood control}} \\
 &= S_0 e^{eTE(1/T_1 - 1/T_2)}
 \end{aligned} \tag{4.3}$$

where  $S_0 = 2e^{-T_1/T_1 - T_E/T_2^*}$  and;  $T_1$ ,  $T_2$  and  $T_2^*$  are the relaxation constants of blood. If it is assumed that  $T_1$  of blood is approximately 1624 ms [28] then it is possible to fit the collected data to a mono-exponential function and find an estimate of  $T_2$ . It is deemed acceptable to use a mean value of  $T_1$  as it will always be much greater than the value of  $T_2$  and thus the possible small changes in  $T_1$  due to blood oxygenation and haematocrit become negligible when fitting the  $T_2$  curve.

The final step in this procedure is to convert the value of  $T_2$  into one of

## 4.2. Methods

---

$Y_v$ . The relationship between  $T_2$  and  $Y_v$  is relatively well known and as such a simple empirically derived calibration curve can be used for this conversion, Figure 4.5 [9, 29, 30].

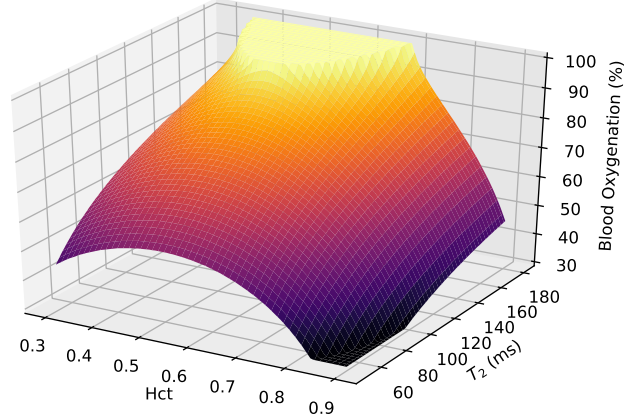


Figure 4.5: The calibration curve used to convert between  $T_2$  and  $Y_v$  for a given haematocrit [31].

The parameters used in the brain TILT TRUST sequence were as follows: label slab thickness = 100 mm, imaging slice thickness = 5 mm, distance between centre of imaging slice and centre of labelling slice = 75 mm, FOV = 220×220×5 mm, matrix size = 64×64, voxel size = 3.44 × 3.44 mm, Sensitivity Encoding (SENSE) = 3, EPI factor = 15,  $T_1$  = 1624 ms, PLD = 1022 ms, the choice of this value will be explored later, TR = 3000 ms, TE = 2.9 ms, eTE = 1 ms, 40 ms, 80 ms and 160 ms with three pairs of images acquired at each. This led to a total scan duration of approximately 84 seconds.

## 4.2. Methods



Figure 4.6: (a) The pulse sequence for TRUST MRI using the FAIR labelling sequence. (b) The selective and non-selective volumes used for tagging via FAIR in the brain. (c) The selective and non-selective volumes used for tagging via FAIR in the kidneys.

The main hurdle to be overcome when moving TRUST to the body is the inhomogeneity in the magnetic field caused by the far less homogeneous tissue susceptibilities within the body compared to the brain. These inhomogeneities mean that it is not possible to use TILT as the labelling method, instead the Flow-sensitive Alternating Inversion Recovery (FAIR) labelling scheme will be used [32], a diagram of this pulse sequence is shown in Figure 4.6a. In the FAIR labelling scheme a selective inversion pulse is applied with slice selective gradients turned on followed by  $T_2$  preparation and acquisition to generate the first image in the pair, a non-selective inversion pulse is then applied with a lower slice selective gradient followed by  $T_2$  preparation and then acquisition to generate the second image. An example of the raw

## 4.2. Methods

---

images produced is shown in Figure 4.7. A schematic of the selective and non-selective slices in the brain and the renal vein are shown in Figures 4.6b and 4.6c respectively. This sequence also has the advantage of being far easier to plan. In the brain having a separate labelling and imaging slice is relatively trivial however the flow of blood in the body is far less ordered and as such, the use of a selective slab within a non-selective slab yields far better results. Movement is a much greater problem in the body. Given the long acquisition time of TRUST it is impossible to carry out the scan in a breath hold, as such the sequence is respiratory triggered via a respiratory belt applied around the subjects chest. The total scan time is therefore dependent upon respiratory rate. Depending on the subject, a delay can be applied between the respiratory trigger and the labelling pulse to acquire images while the subject has fully exhaled.

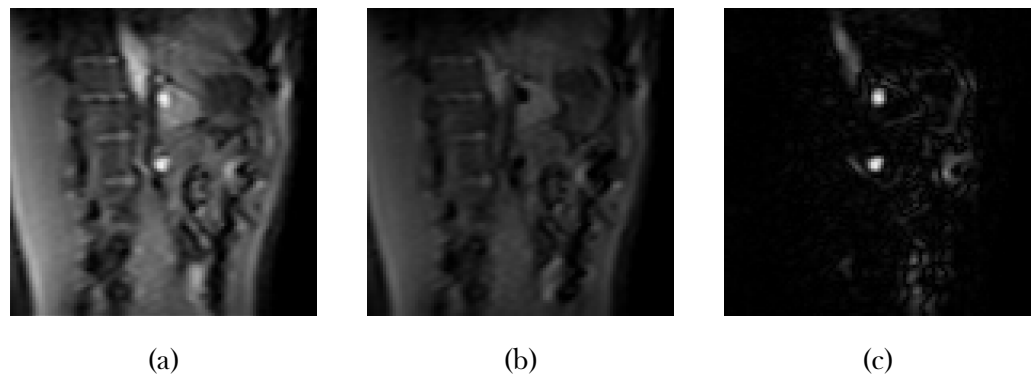


Figure 4.7: The raw images generated when using the FAIR labelling sequence on the kidneys. The non-selective image, (a), is subtracted from the selective image, (b), and generates (c), an image of only the untagged blood. The raw FAIR images from the brain are omitted as they are very similar to those seen in Figure 4.4.

When using the FAIR labelling sequence on the brain the following parameters were used: selective slab thickness = 25 mm, non-selective slab thickness = 400 mm, FOV =  $220 \times 220 \times 5$  mm, matrix size =  $64 \times 64$ , voxel size =  $3.44 \times 3.44 \times 5$  mm, SENSE = 3, EPI factor = 15,  $T_1$  = 1624 ms, PLD = 800 ms, TR = 7276 ms, TE = 2.9 ms, eTE = 1 ms, 40 ms, 80 ms and 160 ms with three pairs of images acquired at each. When used on the body, the para-

## 4.2. Methods

---

meters were as follows: selective slab thickness = 25 mm, non-selective slab thickness = 400 mm, FOV =  $244 \times 244 \times 5$  mm, matrix size = 96×96, voxel size =  $3.44 \times 3.44 \times 5$  mm, SENSE = 3, EPI factor = 15,  $T_1$  = 1624 ms, PLD = 1000 ms, the choice of this value will be explored later, TR = 8076 ms, TE = 2.9 ms, eTE = 1 ms, 40 ms, 80 ms and 160 ms with three pairs of images acquired at each.

### Analysis

The analysis of the data collected using the above protocol was carried out using custom MATLAB (MathWorks, Natick, MA) software based upon code written by Liu and modified to work with data collected using the FAIR labelling method [33]. This software loads the data and carries out the subtraction of each image pair then presents a difference image to the user so the vessel can be drawn around. At this point the voxels with the greatest intensity within the vessel, four voxels when calculating  $Y_v$  for the superior sagittal sinus and nine voxels when working on the renal vein, are averaged, as are the intensities of each repeat eTE. These mean signals are then fit to Equation (4.3) to compute a value of  $T_2$  with confidence bounds. The value of  $Y_v$  can then be found using the aforementioned calibration curve. Once the software has finished, it saves all outputs and intermediary variables to a file on the computer for later analysis.

### 4.2.3 Inducing Changes in Oxygenation of Blood in the Renal Vein

In order to assess the ability of these methods to measure a change in renal oxygenation, a method of inducing such a change in the kidneys needed to be devised. Looking at literature that has carried out similar studies, it is suggested that changes in renal oxygenation can be induced by either varying the subjects sodium intake, water intake or inspired oxygen level [34, 35].

## 4.2. Methods

---

Due to the challenges associated with controlling subjects diet for two weeks as was performed in Prijim [36], the use of sodium intake was discounted. From previous work we know that applying a large water load to subjects during the scanning session, as in Tumkur and Prasad [37, 38], can cause undesired effects on the resultant shim, as assessed by  $B_0$  maps, due to the large susceptibility change adding such a large quantity of water to the abdomen can cause, as such, this method was also discounted leaving us to pursue an oxygen challenge.

This method consisted of localisers and anatomical images being collected followed by alternating BOLD  $T_2^*$  and TRUST scans while the subject was breathing room air to record a baseline. Pure oxygen was then delivered to the subject at 15  $\ell/\text{min}$  via a gas mask and, after a two minute wash in period, the BOLD  $T_2^*$  and TRUST scans were repeated. A visual representation of this protocol can be seen in Figure 4.8. The BOLD  $T_2^*$  scans had a slice thickness of 5 mm, 12 echoes with an initial TE of 5 ms and subsequent echo spacing of 3 ms, the flip angle was 30°. The total scan time was approximately 17 seconds and was acquired during a single breath hold. The TRUST scans were conducted as per Section 4.2.2.



Figure 4.8: The protocol used to induce changes in renal oxygenation.

## 4.3 Results and Discussion

### 4.3.1 Susceptibility-Based Oximetry

#### Susceptibility-Based Oximetry in the Brain

Having collected data using the method outlined in 4.2.1 it was possible to use Equation (4.2) to estimate  $Y_v$  in the superior sagittal sinus to be  $63 \pm 2.1\%$ . This is consistent with the value reported by Liu of  $61.1 \pm 1.4\%$  found in a multi centre TRUST trial with 250 participants over a wide range of ages and ethnicity distribution [15].

#### Susceptibility-Based Oximetry in the Renal Vein

Having calculated an acceptable result in the brain that agreed with literature it was possible to move onto applying techniques to assess oxygenation in the renal vein. A set of three phase maps were collected along with three localisers, one along each plane. If  $\Delta\phi$  is plot against  $\theta$  for a typical  $Y_v$  of 85%, Figure 4.9 is produced. It can be seen that, for an expected  $Y_v$ , the phase difference is greatest if the vessel runs parallel to the  $B_0$  field. No part of the renal vein is located parallel to the  $B_0$  field, typically the angle is in the region of  $75^\circ$  (there is a large degree of variability in vasculature geometry between subjects) and as such delivers a very small phase difference. This coupled with the fact that the gradient of this function at these angles is large, meaning that the uncertainty in angle corresponds to a larger uncertainty in  $Y_v$  means it will unfortunately not be possible to use SBO to accurately measure  $Y_v$  within the renal vein.

### 4.3. Results and Discussion

---



Figure 4.9: For a typical  $Y_v$  of 85% the phase difference produced by a vessel at a range of angles to  $B_0$ .

This technique would perhaps be better suited to use in the liver to assess oxygenation in the portal vein. This vessel runs at a much smaller angle to the  $B_0$  field and as such the model will still be valid with reasonable errors, Figure 4.10. This would potentially work much better than TRUST here as the sequence is much quicker and therefore will be less susceptible to errors caused by movement.

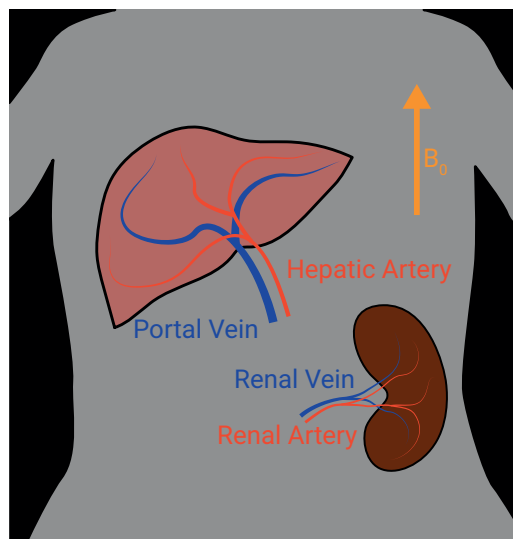


Figure 4.10: A schematic of the portal and renal veins entering the liver and left kidney respectively in relation to the  $B_0$  field.

### 4.3.2 $T_2$ Relaxation Under Spin Tagging

#### TRUST in the Brain

To test if the FAIR labelling sequence delivered the same signal decay as the TILT sequence both labelling schemes were performed sequentially on the superior sagittal sinus with a PLD of 800 ms. The resulting normalised signals are shown in Figure 4.11.

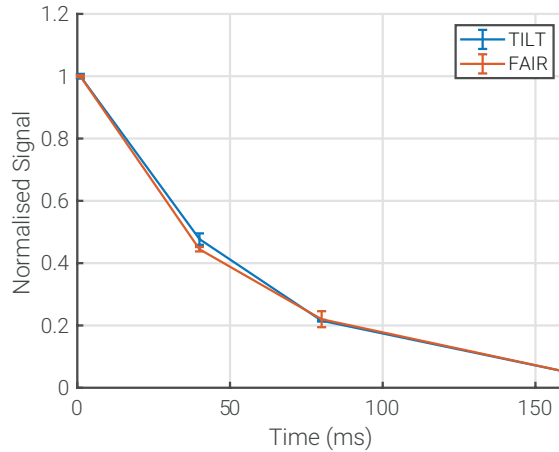


Figure 4.11: The signal decay within the superior sagittal sinus found using TRUST with both TILT and FAIR labelling sequences scaled by their initial signal intensities at eTE = 1 ms.

As can be seen these signals are in excellent agreement with the TILT sequence producing a  $T_2$  of  $52 \pm 1$  ms and the FAIR sequence producing a  $T_2$  of  $50 \pm 2$  ms, therefore in agreement within the bounds of error. This means that FAIR can be directly substituted for TILT in the TRUST sequence to measure  $Y_v$  in the superior sagittal sinus and can subsequently be used for the renal TRUST measurements.

To find the dependence PLD has upon the signal measured, scans were carried out at a range of delays from 400 ms to 1400 ms while using the FAIR labelling sequence. The signal from eTE=1 ms was then plot against label delay. Figure 4.12 shows the signal from the difference images. The maximum signal is observed with a PLD of 800 ms. This value is reached

### 4.3. Results and Discussion

---

due to the balance between  $T_1$  relaxation of the non-selective blood and inflow of unlabelled blood. This maximum in signal agrees with literature using the TILT labelling scheme [12]. By carrying out scans with this PLD the maximum Signal to Noise Ratio (SNR) will be achieved.



Figure 4.12: The mean signal from the first echo of each difference image over a range of PLD times.

$T_2$  should have no dependence upon PLD given the signal from the difference image will have the same decay in time, it will just be a lower intensity for non-optimal PLD thus leading to a larger confidence interval. To confirm this the fit values of  $T_2$  were plotted against PLD, Figure 4.13.



Figure 4.13: The dependence of  $T_2$  upon PLD.

It can be seen that, as predicted, there is no relationship between  $T_2$  and PLD. An increase in error with label delay was not observed, this effect may

### 4.3. Results and Discussion

---

only show itself at larger values of PLD however for our purposes, simply confirming there is no large increase in error around our chosen PLD is sufficient. This means that if there is a variation in the optimum PLD between subjects due to the larger range in RBF compared to Cerebral Blood Flow (CBF) then this will not have an affect upon the value of  $T_2$  and thus  $Y_v$ .

When the analysis is carried out on the images, the four brightest voxels of the difference image are averaged before the fitting occurs. This number of voxels is chosen due to the average size of the superior sagittal sinus however, for some subjects more voxels could be included, potentially yielding better results. To assess the variability in  $T_2$  measurements with the number of voxels averaged, the analysis was run multiple times with one to twelve voxels included in the calculation. Multiple TRUST scans were performed on the same subject and averaged generating Figure 4.14a.



Figure 4.14: (a) The value of  $T_2$  computed for the superior sagittal sinus with different numbers of voxels included in the calculation. (b) The difference image of the superior sagittal sinus with a three voxel ROI shown. This is already covering most of the vessel, hence the noise going up as more voxels are added to the calculation.

Although from Figure 4.14a it would appear that it would be best to only use the brightest voxel in the calculation due to its very small error and that it has the same value of  $T_2$  as the results with far more voxels; this would not be a very robust method. It is fairly easy to conceive a greater than average level of

### 4.3. Results and Discussion

---

noise being recorded on a single voxel in the relaxation and as such skewing the output of the calculation. The confidence interval is so large above six voxels because by this point the calculations are simply including the noise around the vessel rather than the signal from the blood within the sagittal sinus. Given these results, using four voxels in the calculation seems to be a reasonable balance between uncertainty and robustness.

To assess the repeatability of this measure, the optimised scan was repeated ten times on a single subject during one scanning session. This yielded a  $Y_v$  of  $69.5 \pm 0.6\%$ , a value consistent with literature [11, 15]. Given the success of the modified sequence on the superior sagittal sinus, it was possible to attempt to measure  $Y_v$  in the renal vein.

### TRUST in the Body

Ideal vessels to test the TRUST sequence within the body are the portal vein and hepatic artery as these vessels are large, have different oxygen saturations and can easily be imaged at the same time. Using the modified TRUST sequence the  $T_2$  and oxygen saturation of the portal vein was found to be  $109 \pm 5$  ms and  $79.9 \pm 0.8\%$  respectively; the  $T_2$  and oxygen saturation of the hepatic artery was found to be  $157 \pm 10$  ms and  $100 \pm 1\%$  respectively. This means that, as expected, the oxygen saturation in the hepatic artery is measured as greater than that of the portal vein and therefore the TRUST protocol is working as expected. Although normally the analysis would simply be based upon the mean of the brightest voxels in the difference image as outlined in Section 4.2.2, in Figure 4.15 a voxel by voxel analysis has been carried out for illustrative purposes.

To assess if the PLD that generates the greatest signal is the same in the renal vein as in the superior sagittal sinus, a series of scans were collected with PLD ranging from 400 ms to 1400 ms and the signal from eTE = 1 ms recorded.

### 4.3. Results and Discussion

---



Figure 4.15: The oxygen saturation of the portal vein and hepatic artery measured using TRUST.



Figure 4.16: (a) The mean signal from the first echo of each difference image of the renal vein over a range of PLD. (b) Mean signal from the first echo versus PLD from a different subject.

As seen in Figure 4.16a the PLD producing the largest signal in the difference image of the renal vein is indeed different to that of the superior sagittal sinus. This is most likely due to differences in blood flow through each of these vessels,  $413 \pm 136$  ml/min in the renal vein [2] and  $285 \pm 19$  ml/min in the superior sagittal sinus [7]. Given the much larger uncertainty in blood flow in the renal vein, a different subject was scanned over a smaller range of PLD to ascertain if the PLD delivering the maximum signal varies much between subjects, Figure 4.16b.

### 4.3. Results and Discussion

---

The maximum signal for the first subject was achieved at a PLD of 1200 ms whereas for the second subject the maximum is at a PLD of 800 ms. Given that these subjects had a RBF either side of the mean and that there is little dependence of  $T_2$  upon PLD it seems appropriate to use a PLD of 1000 ms for optimum signal in most subjects.

Given the larger size of the renal vein compared to the superior sagittal sinus, it would be better to include more voxels in the calculations when fitting to find a value of  $T_2$ . Multiple scans were completed on a single subject and the value of  $T_2$  found for each using one to twelve voxels in the fitting process. The results were averaged and plot in Figure 4.17a.



Figure 4.17: (a) The value of  $T_2$  calculated for the renal vein with different numbers of voxels included in the calculation. (b) The difference image of the renal vein with a nine voxel ROI shown.

Unlike the results when this process was carried out on the superior sagittal sinus in Figure 4.14a, here the error decreases as more voxels are added to the calculation. This uncertainty comes from the large variation in  $T_2$  for one voxel rather than a large error on the fit i.e. the error is coming from the differences between scans rather than the robustness of each scans results, this is precisely the concern that was raised with using a single voxel when discussing the superior sagittal sinus. As more voxels are added the error decreases until approximately six voxels are included, at this point the value of  $T_2$  stops increasing and stays approximately constant. Once again, given

### 4.3. Results and Discussion

---

the large variation in renal veins, it would be advisable to include slightly more than six voxels but not so many that in the cases of small vessels the algorithm is sampling surrounding tissue. Nine voxels seems to be a suitable middle ground as to work effectively with both small and large vessels.

To assess the repeatability of the measurements within the kidney, the same scan was repeated ten times in a single session with the optimised renal parameters. This yielded a  $T_2$  of  $135 \pm 5$  ms corresponding to a  $Y_v$  of  $89 \pm 2\%$ . The variation in measurements of  $Y_v$  in the renal vein are relatively substantial and show no dependence upon time so are therefore not likely due to physiological changes. The value of  $Y_v$  in the renal vein is much higher than in the sagittal sinus however is within the range found by Nielsen [39].



Figure 4.18: The  $T_2$  relaxation curves of ten scans repeated on a single subject.

To compare the abilities of BOLD  $T_2^*$  maps and TRUST to measure changes in oxygenation in the kidneys, a hyperoxia challenge was conducted. In Figure 4.19a, no systematic, bulk change in  $T_2^*$  can be seen indicating that the change in  $T_2^*$  caused by the introduction of pure oxygen is dominated by other confounding factors. This is confirmed when ROI are defined for the renal cortex and renal medulla with the mean change in  $T_2^*$  found to be  $-2 \pm 8$  ms and  $-1 \pm 6$  ms respectively. When TRUST is used to measure the oxygen saturation in the renal vein an increase of  $16 \pm 3\%$  is observed, Figure 4.19b. This shows that it is possible to measure changes in renal oxygenation using TRUST that would be undetectable using the current standard, BOLD

### 4.3. Results and Discussion

---

$T_2^*$  mapping.

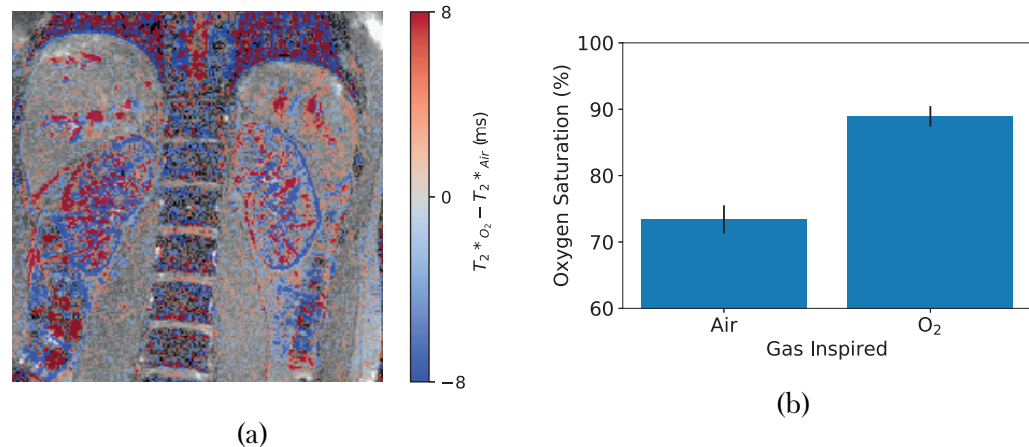


Figure 4.19: (a), The difference in  $T_2^*$  measured between baseline and the hyperoxia state. (b) The difference in  $Y_v$  measured using TRUST.

## 4.4 Conclusions and Future Work

This work shows promising results for the use of a modified TRUST sequence to measure oxygenation of blood within the body. The existing TRUST sequence was modified to be respiratory triggered and use the FAIR labelling scheme making it suitable for use in the body. Once these modifications had been carried out, parameters such as PLD and the number of voxels used in the ROI were optimised. The ability of TRUST to measure a change in renal oxygenation was successfully verified via a hyperoxia challenge which was able to measure an increase of  $16 \pm 3\%$  where the current standard measurement of renal oxygenation, BOLD  $T_2^*$  maps, recorded no significant change.

Looking forward this work could be expanded by carrying out the hyperoxia challenge on more subjects. Although a small number of measurements were gathered on the hepatic vessels, further work could be undertaken to compare the use of SBO and TRUST to measure oxygenation in the portal vein in response to a hyperoxia challenge as conducted for the kidneys here. In the current protocol, haematocrit is assumed to be an average value of 0.41 unless a blood test has recently been undertaken. As stated above, there is a correlation between  $T_1$  of blood and its haematocrit, this means that an estimate of the subjects haematocrit could be taken while they are in the scanner, thus leading to a more accurate measurement of oxygenation with only a small increase in scan time. This would be especially important when using TRUST on patients rather than healthy volunteers as their haematocrit has a larger variance.

## 4.5 Acknowledgements

We thank Hanzhang Lu for sharing the TRUST methodology.

## 4.6 References

1. Daniel, A. J., Cox, E., Buchanan, C., Bradley, C. & Francis, S. *Applying T2 Relaxation Under Spin Tagging (TRUST) to Assess Renal Oxygenation in the Kidney* in *Proc. Intl. Soc. Mag. Reson. Med.* 26 International Society of Magnetic Resonance in Medicine Annual Meeting (Paris, 21st July 2018).
2. Cox, E. F., Buchanan, C. E., Bradley, C. R., Prestwich, B., Mahmoud, H., Taal, M., Selby, N. M. & Francis, S. T. Multiparametric Renal Magnetic Resonance Imaging: Validation, Interventions, and Alterations in Chronic Kidney Disease. *Frontiers in Physiology* **8**. doi:10.3389/fphys.2017.00696 (2017).
3. Buchanan, C. E., Mahmoud, H., Cox, E. F., McCulloch, T., Prestwich, B. L., Taal, M. W., Selby, N. M. & Francis, S. T. Quantitative Assessment of Renal Structural and Functional Changes in Chronic Kidney Disease Using Multi-Parametric Magnetic Resonance Imaging. *Nephrology Dialysis Transplantation*. doi:10.1093/ndt/gfz129 (29th June 2019).
4. Pruijm, M., Milani, B. & Burnier, M. Blood Oxygenation Level-Dependent MRI to Assess Renal Oxygenation in Renal Diseases: Progresses and Challenges. *Frontiers in Physiology* **7**. doi:10.3389/fphys.2016.00667. pmid: 28105019 (5th Jan. 2017).
5. Niendorf, T. *et al.* How Bold Is Blood Oxygenation Level-Dependent (BOLD) Magnetic Resonance Imaging of the Kidney? Opportunities, Challenges and Future Directions. *Acta Physiologica* **213**, 19–38.
6. Chong, S. P., Merkle, C. W., Leahy, C. & Srinivasan, V. J. Cerebral Metabolic Rate of Oxygen (CMRO<sub>2</sub>) Assessed by Combined Doppler and Spectroscopic OCT. *Biomedical Optics Express* **6**, 3941–3951 (11th Sept. 2015).
7. Jordan, J. E., Pelc, N. J. & Enzmann, D. R. Velocity and Flow Quantitation in the Superior Sagittal Sinus with Ungated and Cine (Gated) Phase-Contrast MR Imaging. *Journal of Magnetic Resonance Imaging* **4**, 25–28 (1st Jan. 1994).

#### 4.6. References

---

8. Miao, G., Qingsheng, Y., Zhiyuan, R., Hongxian, Z., Yanfang, Z. & Shuyan, Y. Reference Value of Presenile Human Hematocrit and Geographical Factors. *Journal of Clinical Laboratory Analysis* **16**, 26–29 (1st Jan. 2002).
9. Gardener, A. G., Francis, S. T., Prior, M., Peters, A. & Gowland, P. A. Dependence of Blood R<sub>2</sub> Relaxivity on CPMG Echo-Spacing at 2.35 and 7 T. *Magnetic Resonance in Medicine* **64**, 967–974 (1st Oct. 2010).
10. Shimada, K., Nagasaka, T., Shidahara, M., Machida, Y. & Tamura, H. In Vivo Measurement of Longitudinal Relaxation Time of Human Blood by Inversion-Recovery Fast Gradient-Echo MR Imaging at 3T. *Magnetic resonance in medical sciences: MRMS: an official journal of Japan Society of Magnetic Resonance in Medicine* **11**, 265–271 (2012).
11. Nagdyman, N., Fleck, T., Schubert, S., Ewert, P., Peters, B., Lange, P. E. & Abdul-Khaliq, H. Comparison between Cerebral Tissue Oxygenation Index Measured by Near-Infrared Spectroscopy and Venous Jugular Bulb Saturation in Children. *Intensive Care Medicine* **31**, 846–850 (1st June 2005).
12. Lu, H. & Ge, Y. Quantitative Evaluation of Oxygenation in Venous Vessels Using T<sub>2</sub>-Relaxation-Under-Spin-Tagging MRI. *Magnetic Resonance in Medicine* **60**, 357–363 (1st Aug. 2008).
13. Xu, F., Uh, J., Liu, P. & Lu, H. On Improving the Speed and Reliability of T<sub>2</sub>-Relaxation-Under-Spin-Tagging (TRUST) MRI. *Magnetic Resonance in Medicine* **68**, 198–204 (July 2012).
14. Liu, P., Xu, F. & Lu, H. Test–Retest Reproducibility of a Rapid Method to Measure Brain Oxygen Metabolism. *Magnetic Resonance in Medicine* **69**, 675–681 (1st Mar. 2013).
15. Liu, P. *et al.* Multi-Site Evaluations of a T<sub>2</sub>-Relaxation-Under-Spin-Tagging (TRUST) MRI Technique to Measure Brain Oxygenation. *Magnetic resonance in medicine* **75**, 680–687 (Feb. 2016).
16. Jain, V., Langham, M. C. & Wehrli, F. W. MRI Estimation of Global Brain Oxygen Consumption Rate. *Journal of Cerebral Blood Flow & Metabolism* **30**, 1598–1607 (1st Sept. 2010).

#### 4.6. References

---

17. Jain, V. *et al.* Cerebral Oxygen Metabolism in Neonates with Congenital Heart Disease Quantified by MRI and Optics. *Journal of Cerebral Blood Flow & Metabolism* **34**, 380–388 (1st Mar. 2014).
18. Driver, I. D., Wharton, S. J., Croal, P. L., Bowtell, R., Francis, S. T. & Gowland, P. A. Global Intravascular and Local Hyperoxia Contrast Phase-Based Blood Oxygenation Measurements. *NeuroImage* **101**, 458–465 (1st Nov. 2014).
19. Lee, H., Langham, M. C., Rodriguez-Soto, A. E. & Wehrli, F. W. Multiplexed MRI Methods for Rapid Estimation of Global Cerebral Metabolic Rate of Oxygen Consumption. *NeuroImage* **149**, 393–403 (1st Apr. 2017).
20. Wright, G. A., Hu, B. S. & Macovski, A. Estimating Oxygen Saturation of Blood in Vivo with MR Imaging at 1.5 T. *Journal of Magnetic Resonance Imaging* **1**, 275–283 (1st May 1991).
21. Haacke, E. M., Lai, S., Reichenbach, J. R., Kuppusamy, K., Hoogenraad, F. G., Takeichi, H. & Lin, W. In Vivo Measurement of Blood Oxygen Saturation Using Magnetic Resonance Imaging: A Direct Validation of the Blood Oxygen Level-Dependent Concept in Functional Brain Imaging. *Human Brain Mapping* **5**, 341–346 (1st Jan. 1997).
22. Spees, W. M., Yablonskiy, D. A., Oswood, M. C. & Ackerman, J. J. Water Proton MR Properties of Human Blood at 1.5 Tesla: Magnetic Susceptibility, T1, T2, T\*2, and Non-Lorentzian Signal Behavior. *Magnetic Resonance in Medicine* **45**, 533–542 (1st Apr. 2001).
23. Jain, V., Abdulmalik, O., Propert, K. J. & Wehrli, F. W. Investigating the Magnetic Susceptibility Properties of Fresh Human Blood for Non-invasive Oxygen Saturation Quantification. *Magnetic Resonance in Medicine* **68**, 863–867 (1st Sept. 2012).
24. Jenkinson, M. Fast, Automated, N-Dimensional Phase-Unwrapping Algorithm. *Magnetic Resonance in Medicine* **49**, 193–197 (1st Jan. 2003).
25. Hendrikse, J., Lu, H., van der Grond, J., van Zijl, P. C. & Golay, X. Measurements of Cerebral Perfusion and Arterial Hemodynamics dur-

#### 4.6. References

---

- ing Visual Stimulation Using TURBO-TILT. *Magnetic Resonance in Medicine* **50**, 429–433 (1st Aug. 2003).
26. Golay, X., Petersen, E. T. & Hui, F. Pulsed Star Labeling of Arterial Regions (PULSAR): A Robust Regional Perfusion Technique for High Field Imaging. *Magnetic Resonance in Medicine* **53**, 15–21 (1st Jan. 2005).
  27. Golay, X., Stuber, M., Pruessmann, K. P., Meier, D. & Boesiger, P. Transfer Insensitive Labeling Technique (TILT): Application to Multislice Functional Perfusion Imaging. *Journal of Magnetic Resonance Imaging* **9**, 454–461 (1st Mar. 1999).
  28. Lu, H., Clingman, C., Golay, X. & van Zijl, P. C. Determining the Longitudinal Relaxation Time ( $T_1$ ) of Blood at 3.0 Tesla. *Magnetic Resonance in Medicine* **52**, 679–682 (1st Sept. 2004).
  29. Silvennoinen, M., Clingman, C., Golay, X., Kauppinen, R. & van Zijl, P. Comparison of the Dependence of Blood  $R_2$  and  $R_2^*$  on Oxygen Saturation at 1.5 and 4.7 Tesla. *Magnetic Resonance in Medicine* **49**, 47–60 (1st Jan. 2003).
  30. Liu, P., Chalak, L. F., Krishnamurthy, L. C., Mir, I., Peng, S.-l., Huang, H. & Lu, H.  $T_1$  and  $T_2$  Values of Human Neonatal Blood at 3 Tesla: Dependence on Hematocrit, Oxygenation, and Temperature. *Magnetic Resonance in Medicine* **75**, 1730–1735 (Apr. 2016).
  31. Lu, H., Xu, F., Grgac, K., Liu, P., Qin, Q. & van Zijl, P. Calibration and Validation of TRUST MRI for the Estimation of Cerebral Blood Oxygenation. *Magnetic Resonance in Medicine* **67**, 42–49 (1st Jan. 2012).
  32. Martirosian, P., Klose, U., Mader, I. & Schick, F. FAIR True-FISP Perfusion Imaging of the Kidneys. *Magnetic Resonance in Medicine* **51**, 353–361 (1st Feb. 2004).
  33. Liu, P., Cox, E. & Daniel, A. *Pro TRUST version V2018.5.* 23rd Aug. 2011.
  34. O'Connor, J. P. *et al.* Comparison of Normal Tissue  $R_1$  and  $R_2^*$  Modulation by Oxygen and Carbogen. *Magnetic Resonance in Medicine* **61**, 75–83 (1st Jan. 2009).

#### 4.6. References

---

35. Donati, O. F., Nanz, D., Serra, A. L. & Boss, A. Quantitative BOLD Response of the Renal Medulla to Hyperoxic Challenge at 1.5 T and 3.0 T. *NMR in Biomedicine* **25**, 1133–1138 (1st Oct. 2012).
36. Pruijm, M., Hofmann, L., Maillard, M., Tremblay, S., Glatz, N., Wuerzner, G., Burnier, M. & Vogt, B. Effect of Sodium Loading/Depletion on Renal Oxygenation in Young Normotensive and Hypertensive Men. *Hypertension* **55**, 1116–1122 (1st May 2010).
37. Tumkur, S. M., Vu, A. T., Li, L. P., Pierchala, L. & Prasad, P. V. Evaluation of Intra-Renal Oxygenation during Water Diuresis: A Time-Resolved Study Using BOLD MRI. *Kidney International* **70**, 139–143 (1st July 2006).
38. Prasad, P. V. & Epstein, F. H. Changes in Renal Medullary pO<sub>2</sub> during Water Diuresis as Evaluated by Blood Oxygenation Level-Dependent Magnetic Resonance Imaging: Effects of Aging and Cyclooxygenase Inhibition. *Kidney International* **55**, 294–298 (1st Jan. 1999).
39. Nielsen, K., Rehling, M. & Henriksen, J. H. Renal Vein Oxygen Saturation in Renal Artery Stenosis. *Clinical Physiology* **12**, 179–184 (1st Mar. 1992).

## **Chapter 5**

# **Automated Segmentation of Kidneys using Machine Learning**

---

## Abstract

Total Kidney Volume (TKV) is an important measure in renal disease detection and monitoring. Here a fully automated method to segment the kidneys from  $T_2$ -weighted Magnetic Resonance Imaging (MRI) to calculate TKV of Healthy Control (HC) and Chronic Kidney Disease (CKD) patients is developed.

This automated method uses machine learning, specifically a 2D Convolutional Neural Network (CNN), to accurately segment the left and right kidneys from  $T_2$ -weighted MRI data. The dataset consisted of 30 HC subjects and 30 CKD patients. The model was trained on 50 manually defined HC and CKD kidney segmentations. It was subsequently evaluated on 50 test data sets, comprising data from five HCs and five CKD patients each scanned five times in a scan session to enable comparison of the precision of the CNN and manual segmentation of kidneys.

The unseen test data processed by the 2D CNN had a mean Dice score of  $0.93 \pm 0.01$ . The difference between manual and automatically computed TKV was  $1.2 \pm 16.2$  m $\ell$  with a mean surface distance of  $0.65 \pm 0.21$  mm. The variance in TKV measurements from repeat acquisitions on the same subject was significantly lower using the automated method compared to manual segmentation of the kidneys.

The 2D CNN method provides fully automated segmentation of the left and right kidney and calculation of TKV in under ten seconds on a standard office computer, allowing high data throughput and is a freely available executable.

This work was presented as an aural presentation at the International Society of Magnetic Resonance in Medicine (ISMRM) 28th Annual Meeting (2020) [1] and has been accepted for publication in Magnetic Resonance in Medicine [2].

## 5.1 Introduction

Segmentation of the kidneys from Magnetic Resonance Imaging (MRI) is a time consuming aspect of many renal MRI studies [3–5]. Total Kidney Volume (TKV) gives insight into renal function and is therefore used as a measured parameter for a variety of renal pathologies. The use of TKV is an active area of ongoing research for Autosomal Dominant Polycystic Kidney Disease (ADPKD), which is characterised by an increase in TKV due to cyst formation. Disease progression can be monitored by recording TKV, with higher rates of TKV increase being associated with a more rapid decrease in renal function [6–8]. Measurements of TKV in Chronic Kidney Disease (CKD) subjects have shown a significant correlation with glomerular filtration rate [9], the primary measure of CKD severity [10], with more generally a decrease in TKV associated with a decrease in renal function [11]. When studying pathologies which commonly lead to a change in kidney function, total kidney perfusion is often measured, this metric relies on an accurate measurement of renal blood flow and kidney volume of each kidney, and allows investigators to ascertain if the blood flow is preserved as the organ changes in size or if tissue perfusion is impaired. In addition to TKV measurements, renal segmentation is an important first step for many other processing pipelines, be that for automated cortical-medullary segmentations or to carry out multiparametric mapping within only the kidney to reduce computation times.

The gold standards of kidney segmentation are manual Region Of Interest (ROI) boundary tracing [12] or stereology [13] by experienced and skilled experts, with blood vessels in the kidney and the hilum excluded. These manual processes are highly time consuming (taking approximately 15 – 30 minutes per subject [14–16] and can be biased by investigator judgement due to the similar signal intensities between the kidneys and surrounding organs, anatomical differences between subjects, cysts and image artefacts. Consequently, the resulting kidney ROIs produced are subject to intra- and inter-expert vari-

### 5.1. Introduction

---

ability as a result of the varying expertise levels; experts may segment a specific image differently when performed more than once, or different experts may segment the same image differently. These factors mean that the development of a faster and ideally fully automated method of renal segmentation is highly desirable. However the same factors that make manual segmentation difficult can also limit fully automated methods, for example the signal intensity of the kidneys closely matches that of other abdominal structures such as the spleen.

A number of automated methods have been proposed with varied success [14]. Some simply assume the kidney is an ellipse and calculate the volume from measurements of the pole-to-pole distance [17, 18] or include a correction factor to reduce overestimations [19]. Unfortunately these techniques produce a large confidence interval and still require human intervention to define the pole-to-pole length, a process that can produce inconsistencies between readers and takes a reasonable amount of time ( $\approx 5$  min) [20]. Other semi-automated methods use classical image processing techniques such as thresholding [21], water-shedding [22], level sets [16, 23], and spatial prior probability mapping [24]. These methods can either be inaccurate, over-segmenting the kidneys, or include a number of parameters that need to be manually adjusted and are computationally intensive. Further, the fact that each technique is highly optimised for a specific dataset means that it needs to be re-written to be applied to different pathology, another time consuming and highly skilled process.

Machine learning methods have the potential to automatically detect different patterns from data given to a model which has been trained. Deep learning is a class of machine learning algorithms that can model high-level information in an image using several processing layers of transformations. This uses an architecture of multi-level linear and non-linear operations, described by layers, to learn complex functions that can represent high-level detail to map the input data to the output segmentations directly. As more data becomes available the algorithm can become more accurate and gener-

### 5.1. Introduction

---

alised, without a need to rewrite the underlying methods, thus making it a good choice for long term development.

In recent years, deep learning-based methods have been applied to the segmentation of medical images, especially successful has been the U-Net [25]. This modified fully Convolutional Neural Network (CNN) architecture uses a number of convolution, pooling and up-sampling layers to detect features in the input data at multiple resolutions. The convolution layers convolve a learnable kernel with the input data to generate spatial feature maps that are passed to subsequent layers in the network. By adjusting the kernels, the resulting feature maps can be optimised to detect the location of the kidneys. Pooling layers are used to down-sample the data and allow some convolution kernels to become tuned to approximate features, this also reduces the tendency of the network to overfit the training data. When the data has been fully down-sampled, up-sampling layers are used to increase the resolution of the feature maps back to that of the original data while more convolution layers also learn the precise location of the kidneys. Parameters are adjusted by comparing the output from the network to a known ground truth. CNN methods have been applied to segmentation in other areas of medical imaging [26–29], for example to prostate segmentation of MRI images [30], liver segmentation of x-ray Computed Tomography (CT) images [31] and segmentation of polycystic kidneys [32–34]. However, to date, these methods have not been successfully applied to CKD and healthy kidney segmentation from MR images.

Here a single 2D U-Net model CNN is used for the segmentation of the kidneys in both Healthy Control (HC) participants and CKD patients using  $T_2$ -weighted MR images. Automatically generated kidney masks are compared with manual masks defined by experts and assessed for similarity using multiple voxel and surface based metrics and total segmented volume. A subset of subjects were scanned multiple times to assess the repeatability of the segmentations.

## 5.2 Neural Networks for Image Segmentation

### 5.2.1 Artificial Neural Networks

Artificial Neural Networks (ANNs) aim to solve computational problems using a similar methodology to their biological namesake. Input data is passed through a series of connected nodes or neurons, each of which can have multiple input and output connections from and to other neurons mimicking synapses. At each neuron, a weighted sum of the input values is calculated before being passed onto the next hidden layer of neurons. The final layer of neurons is connected to the output layer which will give an estimation of the desired property, be that a number e.g. probability someone will like a television program, an image e.g. the probability that a pixel in an image is a road sign, or a sample in a time series e.g. audio in voice synthesis. More concisely, an ANN can be used to map a non-linear set of input data to an output dimension.

A very basic example could use the mass and colour of an animal to guess if it is a dog or a cat, Figure 5.1. The connections between neurons are initialised with random weights.

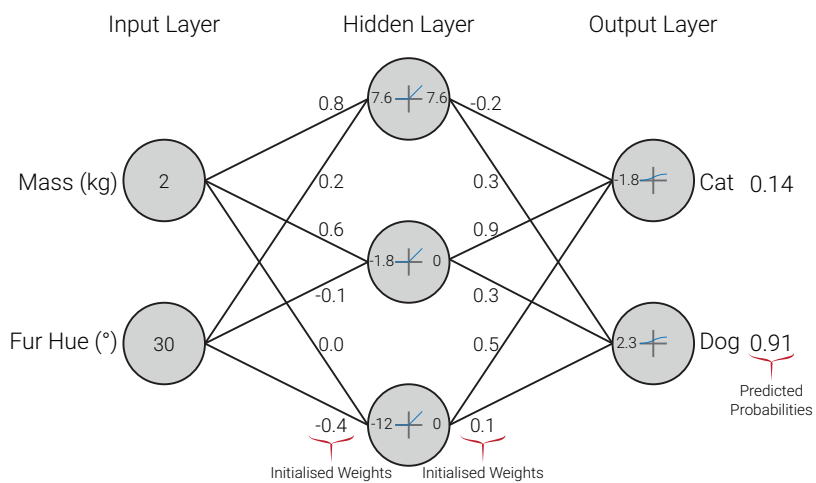


Figure 5.1: The ANN initialised with random numbers trying to predict the species of a small ginger cat.

At each neuron, a weighted sum of its inputs is taken, then an activation function applied, here a Rectified Linear Unit (ReLU), Figure 5.2a, for the hidden neurons and sigmoid, 5.2b, for the output neurons. These activation functions allow the network to act non-linearly and are modelling the action potential of biological neurons. The ReLU function represents a higher rate of firing for signals above zero; as it is impossible for a biological neuron to reduce its firing rate below zero, the ReLU outputs zero when the input signal is negative. The sigmoid function maps all values between zero and one, and therefore ensures the network outputs a probability at the output nodes.



Figure 5.2: Activation functions.

As the weights were randomly initialised, the network has incorrectly predicted that the animal is a dog. By comparing the result output from the network to the known ground truth, the weights of the network can be adjusted in a process known as back propagation, Figure 5.3. Hyper-parameters such as learning rate and momentum control how much each weight is adjusted in response to the input data and subsequent result.



Figure 5.3: The weightings of each connection are adjusted so the output layer produces results closer to the ground truth.

When another animal is input to the network, here a smaller, darker coloured cat, the network now correctly predicts that it is a cat, 5.4. By repeating this procedure many times, comparing the result to ground truths and adjusting the weights, a process known as training, the network becomes more and more accurate. Once trained, the network can be used to infer the species of animals with no ground truth data.

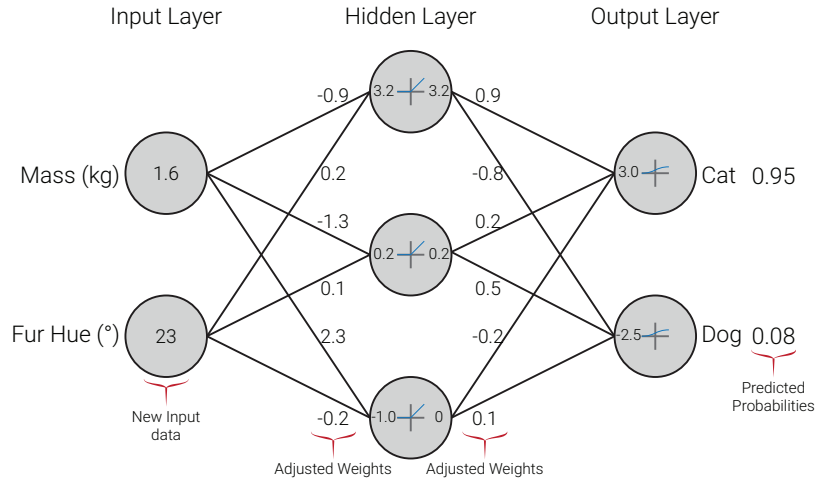


Figure 5.4: New data is presented to the network in the form of a smaller, darker coloured cat and the process of adjusting weights is repeated until more accurate results are produced.

The above example is highly simplified, real ANNs will have many more input nodes and hidden layers. In the case of imaging data, the input layer will simply be a node for each pixel in the image.

### 5.2.2 Convolutional Neural Networks

It was found that ANN segmentation performance was increased if additional features were input to the network. These features could be colour rather than greyscale date, different MRI contrasts e.g. fat/water images or artificially generated features. In Figure 5.5 a selection of artificially generated features are presented, some of these highlight the kidneys from the surrounding tissue e.g. the intensity range adjustment, 5.5b, and edge detector, 5.5f while others are better at providing contrast between the cyst in the right kidney and the renal tissue e.g. the intensity inversion, 5.5c and sharpening filter, 5.5e.



Figure 5.5: An example of the features that can be generated from a raw image (a). Implemented here are intensity range adjustments (b), intensity inversion (c), Gaussian blur (d), sharpening (e) and edge detection (f).

Many of these artificially generated features can be implemented as convolutional operations, these involve convolving a numerical kernel with every pixel in the image. By adjusting the values of each cell in the kernel, different features or filters can be produced. The control of these kernels can be handed over to similar optimisation processes to those used to adjust the weights of the connections between neurons. Over the training period, this enables the network to learn what features are useful for the task at hand and which are less useful rather than the network being given features that the programmer thinks will be helpful. Shallow layers of the network usually resemble features similar to those in 5.5 while deeper layers represent more complex and specific objects such as, using the cat and dog example above, pointy noses to distinguish dogs and triangular ears to distinguish cats. This architecture is known as a Convolutional Neural Network [35, 36].

## 5.2. Neural Networks for Image Segmentation

To aid with feature extraction, the raw image is often downsampled by max-pooling layers, this enables different kernels to act on different scales of the image can help keep the network generalisable and avoid overfitting. The U-Net architecture [25] combines an arm with downsampling and feature extraction with an upsampling arm that returns the image to its initial dimensions making it especially useful for segmentations tasks.

## 5.3 Methods

The study was approved by the University of Nottingham Medical School Research Ethics Committee (H14082014 and E14032013), and East Midlands Research Ethics committee REC reference: 17/LO/2086 and 15/EM/0274.

### 5.3.1 MRI Data Acquisition

All kidney MRI scans were acquired on a 3T Philips Ingenia system (Philips Medical Systems, Best, The Netherlands) using a 2D  $T_2$ -weighted Half-Fourier Single-shot Turbo spin Echo (HASTE) sequence optimised to achieve the maximum contrast between the kidneys and surrounding tissue (Echo Time (TE) = 60 ms, Repetition Time (TR) = 1300 – 1800 ms, Sensitivity Encoding (SENSE) factor = 2.5, refocus angle 120°, bandwidth, 792 Hz, Field Of View (FOV) = 350 x 350 mm<sup>2</sup>, voxel size = 1.5 x 1.5 x 5 mm<sup>3</sup> and a slice gap of 0.5 mm with approximately 18 coronal slices, enough to image the entire kidney [37, 38], in a single 17 - 23 s breath hold.

The dataset consisted of 60 subjects, 30 HC (10 female, 20 male) with a mean age of  $26 \pm 11$  (19–77) years and 30 CKD patients (6 female, 24 male) with a mean age of  $59 \pm 14$  (19–80) years and mean CKD Stage  $3.5 \pm 1.2$  (1-5). Ten of the subjects (5 HCs and 5 CKD patients) were scanned five times in the same scan session for use as test data. In each test data scan session, subjects were repositioned between each acquisition (removed from the scanner, asked to sit up and move on the bed), additionally the scanner operator attempted to vary the acquisition geometry between each scan while still acquiring full kidney coverage. These repeated test datasets allow the consistency of the networks ability to measure TKV to be assessed.

In total, 649 2D image slices from the 50 subjects in the training data and 650 2D image slices from the 10 subjects in the test data, were collected. A summary of the data collected is provided in Table 5.1 and Figure 5.9.

### 5.3.2 Manual Segmentation

The manual binary mask of the kidneys of each subject were generated by one of three observers (A, B and C who had been trained on kidney segmentation and had an average of 2 years of experience), with each observer segmenting data from both the training and testing datasets. Kidney boundaries were manually traced using freely available software (MRIcron [39]) and any area of non-renal parenchyma, such as the renal hilum and cysts, were excluded from the manual definition. Binary masks of the kidney were generated, and the volume of each kidney was computed from the product of the number of voxels in each kidney mask and the voxel volume. Separate kidney volume for the left and right kidneys was determined and summed to compute TKV. All measurements were performed by observers blinded for patient number and previous TKV measurements.

For the training phase, for each subject a manual mask was used from a single observer (randomised between observer A, B, or C). For the testing phase, all five scans from a given subject were segmented by a single reader with the ten subjects being segmented by a mix of the three readers i.e. the test data comprised of subjects segmented by all readers but the repeat scans of each subject were segmented by the same reader. For four HC subjects from the test dataset, manual masks were drawn by all three observers for all five repeat acquisitions to allow assessment of inter-observer variability in the manual masks. HCs were chosen for this analysis as they healthy kidneys have a more consistent morphology and thus will give a best-case measure of observer variability and provide a comparison of the automated method to the highest standard of manual segmentation.

### 5.3.3 Automated Segmentation Using a CNN Architecture

Voxel intensities were normalised between 0 and 255, where 0 was set to the mean voxel intensity minus 0.5 times the standard deviation of that

### 5.3. Methods

---

slice and 255 was set to the mean voxel intensity plus four times the standard deviation of the volume. This empirically derived windowing led to a clear contrast between the kidneys and surrounding tissue while negating the effects of bulk signal changes between volumes. Each dataset volume was then split into 2D coronal slices and resampled to a matrix size of  $256 \times 256$ . Twenty percent of slices were reserved for validation during the network optimisation process, this validation data was used to monitor over-fitting and direct the optimisation process between epochs. Once the data had been split into training and validation sets, the slice order was randomised within sets. Splitting the data before slice randomisation limited the possibility of slices from only one subject being split over both the training and validation datasets. During training, data augmentation was applied. At the start of each epoch, a batch of images and their corresponding masks was selected at random from the training data and a series of random shifts (up to 25 % of the image in both the horizontal and vertical direction), zooms (between 0.75 and 1.25 magnification), rotations (within a  $20^\circ$  range), and sheers (within a  $5^\circ$  range) were applied to the image/mask pair to produce different yet anatomically reasonable images. The weights of the network were then adjusted based on this augmented data before selecting a new batch of images for the next epoch. Augmenting the data reduces the tendency of a model to over-fit the training data and thus increases accuracy when the model is applied to unseen images.

The U-Net consists of two Fully Convolutional Neural Network-like structures that are cascaded in the form of an encoder-decoder (autoencoder) structure. The encoder is used for feature extraction and the decoder is used for feature mapping to the original input resolution. A summary of the network architecture is shown in Figure 5.6. The convolution layers use a set of small parameterised filters, referred to as kernels, to perform convolution operations to produce different feature maps of their input. Here each convolution and deconvolution layer uses a  $3 \times 3$  kernel. Activation layers use a ReLU. Following convolution at each resolution, max pooling with a stride 2 is used on the encoding half of the network.

### 5.3. Methods



Figure 5.6: The architecture of the network used.

The network was implemented using Keras (v2.2.4) [40] with a TensorFlow backend (v1.13.1) [41] in Python 3.6.9. All training was carried out on an NVIDIA Titan Xp Graphical Processing Unit (GPU) (3840 CUDA cores, 12 GB GDDR5X). The network uses a Dice score loss function, given by,

$$D(A, B) = \frac{2|A \cap B|}{|A| + |B|} = \frac{2TP}{2TP + FP + FN}, \quad (5.1)$$

where  $TP$  is true positive,  $FP$  is false positive and  $FN$  is false negative. A value of 1 implies complete overlap between the automated mask and the manual mask while 0 implies no overlap. This function is ideal for renal segmentation as it does not weight true negatives which represent the majority of voxels input to the network and thus means that while the network is training, it does not become trapped in a local minimum outputting solely background voxels. Training was carried out over 150 epochs using stochastic gradient descent with an initial learning rate of 0.01 and learning rate decay of  $5 \times 10^{-7}$  and momentum of 0.8, these parameters help the optimiser converge quickly while also avoiding overshooting. As seen in Figure 5.7, after 150 epochs the validation Dice score plateaued while the training Dice score was still rising slightly, indicating that any further training would lead to over-fitting. Training took approximately thirty minutes.

### 5.3. Methods

---



Figure 5.7: Dice score of the network for the training and validation data. Data is shown with a 10 epoch rolling average.

#### 5.3.4 Statistical Analysis

Baseline demographics are reported as mean  $\pm$  Standard Deviation (SD). Inter-observer variability in manual segmentation and TKV was calculated by comparing the TKV of the manual masks each observer generated for a given volume, and also assessing the Bland-Altman and regression analysis. Intra-observer variability in manual segmentation was calculated by comparing the TKV of the five masks generated by an observer for a given subject. For each, the mean Coefficient of Variation (CoV); defined as standard deviation/mean and Intraclass Correlation (ICC) were used as measures of repeatability of TKV. Voxel-based metrics (Dice score, Equation (5.1) and Jaccard index, Equation (5.2)) and surface based metrics such as the average distance between the surface of the two masks and Hausdorff Distance 95th percentile, the 95th percentile of the largest distance between the two surfaces, were also calculated between each observer.

$$J(A, B) = \frac{A \cap B}{A \cup B} = \frac{TP}{TP + FP + FN} \quad (5.2)$$

The performance of the automated segmentation was assessed using the

### **5.3. Methods**

---

voxel and surface based similarity metrics outlined above and, in addition, sensitivity, specificity, precision and accuracy, Equations (5.3) - (5.6). Performance was further assessed by determining the mean difference in TKV between the automatic and manual methods. Both actual and percentage (%) difference in TKV were evaluated. Bias (mean) obtained from the automatic and manual methods was assessed using a paired sample t-test. The mean CoV and ICC were also used as measures of repeatability of the automated TKV.

$$\text{Sensitivity} = \frac{TP}{TP + FN} \quad (5.3)$$

$$\text{Specificity} = \frac{TN}{TN + FP} \quad (5.4)$$

$$\text{Precision} = \frac{TP}{TP + FP} \quad (5.5)$$

$$\text{Accuracy} = \frac{TP + TN}{TP + TN + FP + FN} \quad (5.6)$$

## 5.4 Results

### 5.4.1 Characteristics of the Training Cohort

Data was collected using a  $T_2$ -weighted HASTE sequence providing optimal contrast between the kidneys and surrounding tissue, examples shown in Figure 5.8, however there is limited contrast between the left kidney and spleen due to their similar  $T_2$ -weighting. Cysts of variable size are clearly visible in the kidneys of the CKD patient.



Figure 5.8: All slices of the raw data from representative subjects of the HC cohort, shown in a, and CKD cohort, b.

The training data comprised 25 healthy controls (9 female, 16 male) with a mean age of  $26 \pm 12$  (19–77) years and 25 CKD patients (6 female, 19 male) with a mean age of  $58 \pm 15$  (19–80) years and mean CKD stage  $3.3 \pm 1.1$  (1–5). The manual TKV was  $277 \pm 60$  mℓ, ranging between 145 and

## 5.4. Results

---

422 mℓ. Including both healthy control subjects and CKD patients meant the kidneys had variable morphology (shape, size and heterogeneous cysts) within the training dataset. Table 5.1 provides the characteristics of datasets used for training and testing of the CNN, whilst Figure 5.9 shows the distribution of TKV within the training and testing data.

	Number of Subjects	Number of Datasets	Number of 2D Slices	Sex (F/M)	Mean Age	TKV (mℓ)
Training HC	25	25	325	9/16	26 ± 12	296 ± 38
Training CKD	25	25	324	6/19	58 ± 15	258 ± 72
Testing HC	5	25	325	1/4	25 ± 3	330 ± 35
Training CKD	5	25	325	0/5	69 ± 3	274 ± 56

Table 5.1: Characteristics of datasets used for training and validation of the 2D U-Net model CNN.



Figure 5.9: Distribution of TKV within the training and testing data.

### 5.4.2 Reducing Acquisition Time

Initial data was collected with a TR of 1800 ms leading to a breath hold of approximately 23 seconds. Some subjects struggled to hold their breath for this long on expiration, therefore the effects of reducing the TR of the

## 5.4. Results

---

sequence were investigated. As can be seen in Figure 5.10, there is no degradation in image quality from the image with TR of 1800 ms to that with at TR of 1300 ms, the differences between these images are mainly due to the small movements between volumes, as can be seen in the difference data where the largest differences are seen around the periphery of the kidneys and in the gut. Moving forward, the TR was reduced to 1300 ms leading to a sequence with a breath hold of approximately 17 seconds.

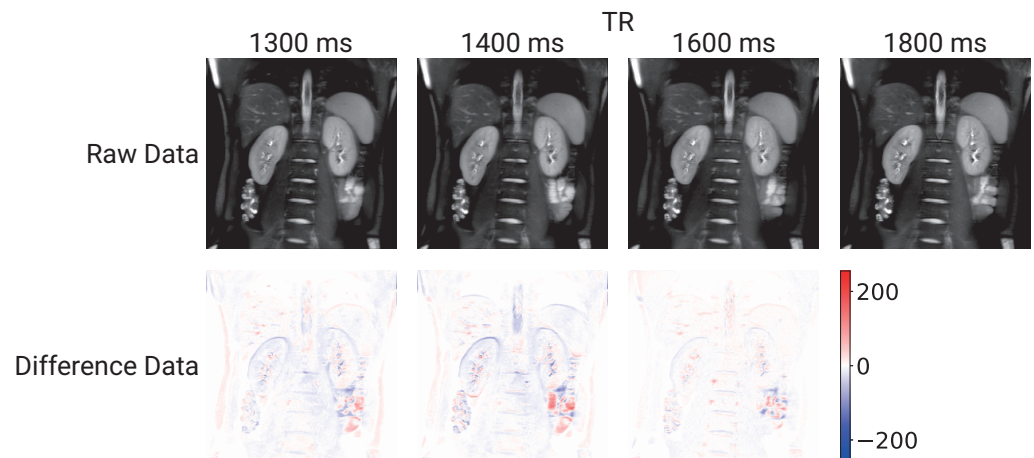


Figure 5.10: The effects of changing the TR of the sequence.

### 5.4.3 Accuracy of Manual Segmentation

Four of the test subjects were each scanned five times, with the left and right kidneys in the 20 datasets each masked by Observers A, B and C. The intra-observer and inter-observer variability for this manual segmentation was computed, as shown in Table 5.2.

## 5.4. Results

---

Observer	Kidneys	CoV (%)	ICC
Intra A	Total	$2.2 \pm 0.7$	0.939
	Left	$3.2 \pm 0.8$	0.783
	Right	$1.9 \pm 0.5$	0.957
Intra B	Total	$1.9 \pm 0.3$	0.895
	Left	$2.0 \pm 0.5$	0.807
	Right	$2.4 \pm 0.3$	0.892
Intra C	Total	$2.5 \pm 0.9$	0.908
	Left	$2.8 \pm 1.3$	0.769
	Right	$3.1 \pm 1.9$	0.940
Inter	Total	$3.0 \pm 1.0$	0.897
	Left	$4.0 \pm 1.4$	0.713
	Right	$2.9 \pm 1.0$	0.910

Table 5.2: Repeatability of the manual segmentation for left, right and TKV, with coefficient of variation and intraclass coefficient computed.

Additionally, similarity metrics were used to assess the overlap between each observer’s manual masks, Table 5.3. Due to the large difference between in-plane and out-of-plane resolution ( $1.5 \text{ mm}^3$  vs  $5.5 \text{ mm}^3$ ) the Hausdorff distance is very susceptible to inaccuracies in the anterior – posterior direction; this metric is highly sensitive to noise and as such the 95th percentile is used to generate a more representative value. Bland-Altman plots and regression analysis of inter-observer variance in measured TKV are provided in Figure 5.11.

## 5.4. Results

Observer	Kidney	Dice Score	Jaccard Index	Average Distance (mm)	Hausdorff Distance (mm) (95th Percentile)	Volume Difference (ml)
A - B	Both	0.93 ± 0.03	0.87 ± 0.05	0.81 ± 0.58	5.59 ± 2.77	20.84 ± 9.33
	Left	0.92 ± 0.07	0.85 ± 0.10	0.94 ± 1.12	5.53 ± 3.65	13.36 ± 5.76
	Right	0.94 ± 0.01	0.88 ± 0.02	0.65 ± 0.14	4.75 ± 1.15	7.48 ± 5.63
A - C	Both	0.93 ± 0.01	0.87 ± 0.02	0.79 ± 0.18	5.83 ± 1.86	16.01 ± 8.56
	Left	0.93 ± 0.01	0.87 ± 0.02	0.84 ± 0.27	6.83 ± 3.12	6.93 ± 5.78
	Right	0.93 ± 0.01	0.87 ± 0.02	0.72 ± 0.17	4.82 ± 1.25	9.08 ± 5.41
B - C	Both	0.94 ± 0.04	0.89 ± 0.06	0.68 ± 0.62	3.59 ± 2.74	-4.83 ± 9.92
	Left	0.93 ± 0.08	0.88 ± 0.11	0.78 ± 1.22	4.31 ± 3.58	-6.44 ± 6.17
	Right	0.95 ± 0.01	0.90 ± 0.02	0.48 ± 0.14	3.39 ± 1.15	1.61 ± 6.56

Table 5.3: Metrics comparing each combination of observers manual masks (A – B, A – C and B – C). All values are quoted as mean ± standard deviation.



Figure 5.11: Bland-Altman and regression analysis of inter-reader variations in TKV

#### 5.4.4 Network Testing

To verify that the trained network is behaving as expected saliency maps were produced, Figure 5.12, this is especially important given the black box nature of machine learning methods. This map shows the areas the network is using most in its classification [42]. It verifies that the networks is using the outside areas of the kidney to make its prediction with areas of a similar intensity receiving some attention to distinguish them from the kidney. While this is precisely what is expected of the algorithm, it is important to check this as it is possible for such a method to have learnt a slightly different mechanism for the segmentation, one that is more prone to errors if new data is presented to it.

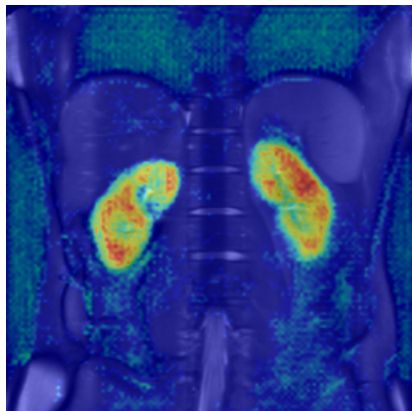


Figure 5.12: An example saliency map of the areas the network uses most when segmenting the kidney.

The trained network was used to predict segmentations of the 2D kidney slices and compute TKV for each of the unseen test volumes. The mean Dice score over the 50 test volumes was  $0.93 \pm 0.01$  ( $0.94 \pm 0.02$  for HC and  $0.92 \pm 0.01$  for CKD patients). The TKV predicted by the network was, on average,  $1.2 \pm 16.2$  mℓ less than the manually segmented TKV and thus not significantly different ( $p = 0.615$ ) (Figure 5.13) This accuracy was comparable for the HC and CKD cohorts, with automated CNN TKV measurements of  $4.7 \pm 17.7$  mℓ greater than manual and  $7.0 \pm 12.4$  mℓ less than manual respectively. A summary of the CNN accuracy when evaluated using

## 5.4. Results

---

similarity metrics and volume difference from manual measures is shown in Table 5.4. Note a slightly larger discrepancy for the left compared to the right kidney. Figure 5.13 shows plots of the difference in volume between manual segmentation and automated segmentation of the test dataset.



Figure 5.13: The difference between the TKV predicted by the CNN and the manually segmented true TKV. Mean and standard deviation TKV difference are shown as dashed and dotted lines respectively. Each subject is shown in a different colour. (a) shows the absolute volume difference (b) shows the percentage volume difference.

## 5.4. Results

---

Cohort	Kidney	Dice Score	Jaccard Index	Sensitivity	Specificity	Precision	Accuracy	Mean Surface Distance (mm)	Hausdorff Distance (mm) (95th Percentile)	Volume Difference (p)
All	Total	0.93 ± 0.01	0.87 ± 0.03	0.93 ± 0.03	0.997 ± 0.001	0.93 ± 0.02	0.995 ± 0.001	0.65 ± 0.21	4.33 ± 1.64	-1.16 ± 16.23 (0.615)
	Left	0.92 ± 0.02	0.86 ± 0.04	0.91 ± 0.05	0.997 ± 0.001	0.94 ± 0.03	0.994 ± 0.002	0.76 ± 0.31	4.42 ± 1.52	-3.95 ± 12.38 (0.029)
	Right	0.94 ± 0.02	0.89 ± 0.03	0.95 ± 0.03	0.997 ± 0.001	0.93 ± 0.03	0.996 ± 0.001	0.54 ± 0.21	3.66 ± 1.76	2.79 ± 6.84 (0.006)
	Total	0.94 ± 0.02	0.88 ± 0.03	0.95 ± 0.05	0.997 ± 0.001	0.93 ± 0.03	0.995 ± 0.001	0.68 ± 0.27	4.50 ± 1.97	4.66 ± 17.72 (0.201)
	Left	0.93 ± 0.02	0.87 ± 0.04	0.94 ± 0.05	0.997 ± 0.001	0.93 ± 0.03	0.994 ± 0.002	0.79 ± 0.37	4.47 ± 1.81	1.91 ± 12.93 (0.467)
	Right	0.95 ± 0.02	0.90 ± 0.03	0.96 ± 0.03	0.997 ± 0.001	0.94 ± 0.02	0.996 ± 0.001	0.56 ± 0.26	3.81 ± 2.11	2.75 ± 7.70 (0.087)
CKD	Total	0.92 ± 0.01	0.86 ± 0.02	0.91 ± 0.02	0.998 ± 0.001	0.94 ± 0.02	0.995 ± 0.001	0.63 ± 0.14	4.16 ± 1.24	-6.98 ± 12.38 (0.009)
	Left	0.92 ± 0.02	0.85 ± 0.03	0.89 ± 0.04	0.998 ± 0.001	0.95 ± 0.02	0.994 ± 0.002	0.73 ± 0.24	4.37 ± 1.21	-9.81 ± 8.62 (0.00001)
	Right	0.93 ± 0.01	0.88 ± 0.02	0.94 ± 0.02	0.997 ± 0.001	0.92 ± 0.03	0.996 ± 0.001	0.51 ± 0.13	3.51 ± 1.34	2.83 ± 6.02 (0.027)

Table 5.4: The accuracy of the CNN compared to manual segmentations using a variety of metrics stratifying the testing data by cohort and left vs right kidney. All values are given as mean ± standard deviation.

## 5.4. Results

---

In Figure 5.14, the TKV predicted by the CNN is plot against the manual TKV, in ninety percent of subjects, the standard deviation of TKV measurements between each volume for a subject was smaller when the TKV was measured using the CNN as oppose to manually. The mean CoV and ICC were  $2.7 \pm 0.9\%$  and 0.979 respectively across the 5 repeats of the manually segmented test data (using masks from observers A, B and C), compared to a value of  $1.5 \pm 0.5\%$  and 0.993 respectively for the automatic segmentations of the 5 repeats of test data. The CNN produced a significantly lower CoV than the manual segmentations ( $p = 0.008$ ).

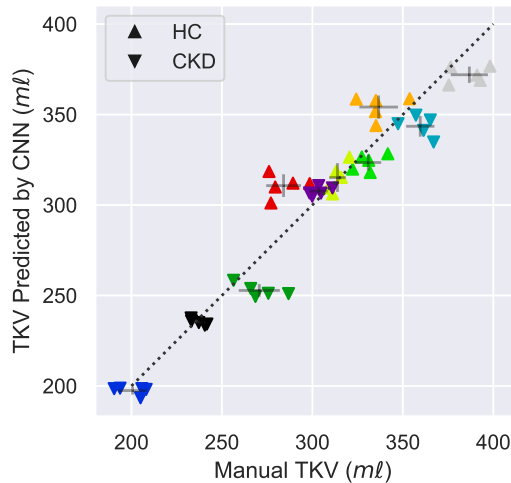


Figure 5.14: The TKV predicted by the CNN plot against the manually segmented true TKV with each subject plot in a different colour. The standard deviation measured using both methods is shown as error bars originating from the mean of each subject. The dotted line represents perfect correlation between the CNN and manual segmentation.

Representative examples of the output from the network for both HC and CKD data are shown in Figure 5.15. The automated CNN accurately segments the kidneys, and for CKD patients, often omits cysts from the masks.

## 5.4. Results

---



(a)



(b)

Figure 5.15: Representative raw test data and corresponding masks of a HC, (a), and CKD subject, (b). Manually generated masks are shown in blue, automatically generated masks are shown in red and the overlap of the two is shown in magenta.

Since this is a 2D CNN, it is important to assess the accuracy across the anterior – posterior 2D slices of the kidney. This was achieved by comparing

## 5.4. Results

---

the Dice score of the CNN to the inter-reader Dice scores, Figure 5.16. A decrease in accuracy in the outer slices can be seen in both the CNN and manual masks.

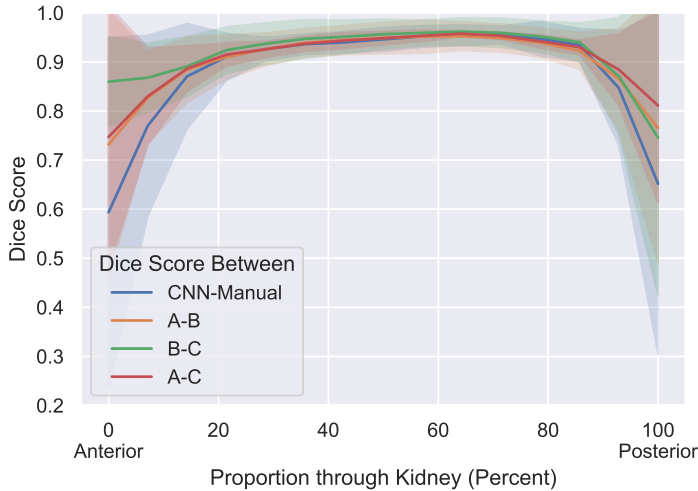


Figure 5.16: Mean Dice score for 2D slices from anterior to posterior. The shaded area represents one standard deviation from the mean Dice score.

This decrease in accuracy manifests itself on the outer slices of the volume, where the proportion of kidney per slice is smaller and as such the 2D network, with a lack of spatial context in the anterior – posterior direction, finds these outer slices more challenging. This decrease in accuracy can partly be explained by the fact that larger structures (in terms of number of voxels) will in general produce higher scores for comparable errors because the vast majority of errors are on the perimeter of the kidney in each slice, slices with fewer voxels of kidney have a smaller area to perimeter ratio, Figure 5.17.

## 5.4. Results

---



Figure 5.17: A 2D histogram of the perimeter and area of each slice for both the HC and CKD cohorts.

## 5.5 Discussion

In this chapter, a 2D CNN has been trained to generate automatic segmentations of healthy control and CKD patients. Segmentations of the left and right kidneys are computed from which total kidney volume is estimated. The CNN was trained on both healthy control and CKD kidneys with a range of TKV (144.76 – 422.49 ml) which included the presence of cysts. The automated segmentation by the CNN yielded a mean Dice score of  $0.93 \pm 0.01$  and took an average time of 9 s to measure TKV compared to 15 – 30 minutes [14] for manual segmentation. The automated CNN can be run as a self-contained Graphical User Interface (GUI) with the data and programme freely available [[daniel\\_alexdaniel654/renal\\_segmentor\\_2020](#)] and thus avoid the need for complicated software setup. Note the software released at present can only be used to process coronal HASTE images and will not be accurate with other geometries/contrasts, for this, training of the network with a different dataset would be required and thus necessitate the use of a GPU.



Figure 5.18: The Graphical User Interface used to segment kidneys.

### 5.5.1 Evaluation of Methodology

The network performed with high precision on the test data with a  $1.2 \pm 16.2 \text{ m}\ell$ , statistically insignificant, discrepancy between manual and automated TKV measurements. Table 5.4 shows the agreement between the CNN and manual masks is higher for the right than left kidney, this is in part due to the proximity and lack of contrast between the left kidney and the spleen making distinguishing this boundary difficult for the CNN. This difficulty also leads to inconsistencies in manual masks, borne out by the increased CoV and decreased ICC and similarity metrics of the left kidney when compared to the right kidney in Table 5.2 and Table 5.4 assessing the variability in manual masks between observers. From Table 5.4 it can also be seen that the agreement between the CNN and manual masks is greater for the healthy control cohort than the CKD cohort, this is expected due to the increased variation in kidney morphology and the presence of cysts in the CKD cohort. Figure 5.13 shows that the difference between the manual TKV and CNN predicted TKV is not dependent on the true TKV, therefore the training data is balanced and well augmented as the network is able to accurately perform over the full range of kidney size in the test data.

Here, five volumes of test data were collected for each subject by repositioning the subject in the scanner within an hour scan session, and therefore any variance in measured TKV is purely due to inaccuracies in the kidney ROI definition. On assessing the correlation between manual and CNN measured TKV in Figure 5.14, it can be seen that, in 90 % of subjects the intra-observer variance in manual TKV between the segmentation of the five volumes collected in each subject is larger than using the CNN to estimate TKV, as reflected by the lower CoV and increased ICC of the TKV measured using the CNN ( $\text{CoV } 1.5 \pm 0.5 \%$ ,  $\text{ICC } 0.993$ ) compared to the manual measures ( $\text{CoV } 2.7 \pm 0.9 \%$ ,  $\text{ICC } 0.979$ ). As the network is trained on the kidney segmentations from three observers (A, B and C), it has been optimised by inheriting the most accurate tendencies of each observer e.g. one observer may have been very accurate when excluding cysts but not as accurate at defining

## 5.5. Discussion

---

the kidney-spleen boundary. The network will have learnt to exclude cysts from this observer but to delineate between kidney and spleen from another observer. Thus the network can become more precise than each individual observers manual segmentations. This increased precision can be seen in Figure 5.13 when compared to Figure 5.14 where the variance in difference in TKV is driven by the larger variance in manual TKV. The smallest TKV per subject is consistently overestimated when compared to its manual mask and vice versa the largest manual TKV per subject is often an underestimation compared to the manual TKV.

Figure 5.15 illustrates the masks produced by the manual segmentation and the CNN for both a HC and CKD patient. For the HC, the CNN includes more voxels around the edge of its mask than manual segmentation, and the network is more anatomically accurate e.g. where the interface between the kidney and spleen is very narrow, the CNN predicts the kidney is adjacent to the spleen whilst the observers manual segmentation leaves a gap. The CKD data shown in Figure 5.15b includes a cyst in each of the kidneys. The network was trained on a combination of healthy and CKD data, with 19 of the 25 CKD training datasets containing at least one cyst. The CNN can be seen to segment out the cysts, despite their highly variable morphology and prevalence in the overall training data.

The amount of augmentation applied to the training data was empirically derived (random shifts up to 25 % of the image in both the horizontal and vertical direction, zooms between 0.75 and 1.25 times magnification, rotations within a 20 degree range, and sheers within a 5 degree range) and led to the potential for large transforms being applied to the data and masks if the extremes of each transform were randomly selected. This large degree of augmentation was advantageous as it mirrors the large variation in acquisition planning in abdominal imaging.

A 2D CNN was used to process each 2D slice of a full volume, rather than a 3D volume. This was advantageous for the relatively small training dataset

## 5.5. Discussion

---

the network was optimised on, as it avoids overfitting and allows the network to easily be used on volumes of variable slice number. However, this can come at the expense of accuracy as 2D CNNs do not leverage the information from adjacent slices in the segmentation as is done in 3D CNN, but 3D CNN come with a computational cost as a result of the increased number of parameters used. 3D networks have successfully been implemented on neural data using patching methods where the image volume is divided up into smaller cubes [28] to reduce memory requirements and allow for differing input shapes. While this works well in the brain, there are a number of reasons why this method may not be as successful for body applications. The out-of-plane resolution is significantly less than the in-plane resolution; this results in far fewer slices in one direction than the other two. To avoid overfitting for a certain number of slices e.g. training on a 11 slice image with a 113 patch, and subsequently the network not performing well when the patch is applied to a 16 slice image, the patch would need to be much smaller than the number of slices, thus diminishing the benefits of the 3D methodology. Additionally, the extra memory requirements for a 3D network limit the ease of use of the software for inference on many standard office computers.

### 5.5.2 Future Directions

Future work will explore alternative network architectures. As the main source of inaccuracy with the current network is its lack of slice-to-slice context, there are multiple architectures that can address this. A relatively simple method would be exploiting the fact that the Keras framework is designed to work with colour images. By combining three slices into a single image where each slice represents either the red, green or blue channel, Figure 5.19, the network would be able to use contextual information about the adjacent slices to help inform its predictions. This method result in two slices from each volume being becoming impossible to process and as such the FOV would have to be increased. Alternatively multiple network architectures such as Recursive Neural Network (RNN) [48], and Long Short-Term

## 5.5. Discussion

---

Memory (LSTM) [44] are designed to have a memory therefore enabling them to retain contextual information from slice to slice. Alternatively, if more training data were available, a 3D CNN could be explored to ascertain if the any improved accuracy is worth the increase in hardware requirements and reduced generalisability.



Figure 5.19: An example of using colour information to represent adjacent slices for processing by a CNN. Vessels in the liver can clearly be seen travelling through the three slices as they change from red to green to blue.

This image contrast was chosen as a result of recent publications comparing  $T_1$ - and  $T_2$ -weighted images for TKV assessment reporting that  $T_2$ -weighted images provide better quality to enable TKV measurements, leading to improved reproducibility with lower intra- and inter-reader variability [45]. Other contrasts e.g. a  $T_1$ -weighted scan, could also be collected, registered to the  $T_2$ -weighted images and used as another channel to inform segmentation.

This network was validated on healthy subjects and CKD patients, but has not been trained and validated on subjects with ADPKD. These subjects have many more cysts in their kidneys, while the CNN was able to segment cysts encountered in the CKD cohort, it would be beneficial for future work on ADPKD to retrain the network with HC, CKD and ADPKD data, where TKV is a recognised biomarker of disease progression.

## 5.5. Discussion

---

Another common segmentation task in renal imaging is generating an ROI for the renal cortex and medulla. There are some automated methods of achieving this once a total kidney mask has been produced [3, 46], however there has been no work on the application of deep learning to this task. In addition to the acquisition of the  $T_2$ -weighted dataset used here, a  $T_1$ -weighted dataset designed to optimise the contrast between cortex and medulla was also collected on each subject [38], an example of which is shown in Figure 5.20. Using this data, it may be possible to develop this method further such that an automated mask for each tissue type is produced.



Figure 5.20: An example of the data collected to enable segmentation of the renal cortex and medulla.

## 5.6 Conclusions

A CNN has been shown to successfully segment the kidneys of both HC and CKD subjects from  $T_2$ -weighted data delivering a mean Dice score of  $0.93 \pm 0.01$  leading to a mean volume of  $1.2 \pm 16.2 \text{ m}^3$  less than the manually segmented TKV and mean surface distance of  $0.65 \pm 0.21 \text{ mm}$ . The CNN produces higher than human precision, with a CoV and ICC of  $1.5 \pm 0.5 \%$  and  $0.993$  respectively. The accuracy of the network could be further increased via the acquisition of more training data, something the renal group at Sir Peter Mansfield Imaging Centre (SPMIC) are actively pursuing.

The methods developed here can easily be deployed via the self contained, easy to use GUI, thus moving renal segmentation from a 15 to 30 minute skilled task, to a 10 second task for anyone, on any hardware. Additional, this executable can be called from a terminal, making it suitable for use in scripting applications and pipelines.

Future development will focus around exploring different network architectures, use of additional contrasts and expanding the tool to produce masks of both the cortex and medulla.

## 5.7 Acknowledgements

We gratefully acknowledge the support of NVIDIA Corporation with the donation of the Titan Xp GPU used for this research.

## 5.8 References

1. Daniel, A. J., Buchanan, C., Allcock, T., Scerri, D., Cox, E., Prestwich, B. & Francis, S. *Automated Renal Segmentation in Healthy and Chronic Kidney Disease Subjects Using A Convolutional Neural Network* in *Proc. Intl. Soc. Mag. Reson. Med.* 28 International Society of Magnetic Resonance in Medicine Annual Meeting (Online, Aug. 2020).
2. Daniel, A. J., Buchanan, C. E., Allcock, T., Scerri, D., Cox, E. F., Prestwich, B. L. & Francis, S. T. Automated Renal Segmentation in Healthy and CKD Subjects Using A Convolutional Neural Network. *Magnetic Resonance in Medicine*. doi:10.1002/mrm.28768 (2021).
3. Cox, E. F., Buchanan, C. E., Bradley, C. R., Prestwich, B., Mahmoud, H., Taal, M., Selby, N. M. & Francis, S. T. Multiparametric Renal Magnetic Resonance Imaging: Validation, Interventions, and Alterations in Chronic Kidney Disease. *Frontiers in Physiology* **8**. doi:10.3389/fphys.2017.00696 (2017).
4. Cohen, E. I., Kelly, S. A., Edye, M., Mitty, H. A. & Bromberg, J. S. MRI Estimation of Total Renal Volume Demonstrates Significant Association with Healthy Donor Weight. *European Journal of Radiology. Rheumatoid Disease and Imaging* **71**, 283–287 (1st Aug. 2009).
5. Van den Dool, S. W., Wasser, M. N., de Fijter, J. W., Hoekstra, J. & van der Geest, R. J. Functional Renal Volume: Quantitative Analysis at Gadolinium-Enhanced MR Angiography—Feasibility Study in Healthy Potential Kidney Donors. *Radiology* **236**, 189–195 (1st July 2005).
6. Chapman, A. B. *et al.* Kidney Volume and Functional Outcomes in Autosomal Dominant Polycystic Kidney Disease. *Clinical Journal of the American Society of Nephrology* **7**, 479–486 (1st Mar. 2012).
7. Tangri, N., Hougen, I., Alam, A., Perrone, R., McFarlane, P. & Pei, Y. Total Kidney Volume as a Biomarker of Disease Progression in Autosomal Dominant Polycystic Kidney Disease. *Canadian Journal of Kidney Health and Disease* **4**, 2054358117693355 (1st Jan. 2017).
8. Grantham, J. J. *et al.* Volume Progression in Polycystic Kidney Disease. *New England Journal of Medicine* **354**, 2122–2130 (18th May 2006).

## 5.8. References

---

9. Buchanan, C. E., Mahmoud, H., Cox, E. F., McCulloch, T., Prestwich, B. L., Taal, M. W., Selby, N. M. & Francis, S. T. Quantitative Assessment of Renal Structural and Functional Changes in Chronic Kidney Disease Using Multi-Parametric Magnetic Resonance Imaging. *Nephrology Dialysis Transplantation*. doi:10 . 1093 / ndt / gfz129 (29th June 2019).
10. Stevens, L. A., Coresh, J., Greene, T. & Levey, A. S. Assessing Kidney Function — Measured and Estimated Glomerular Filtration Rate. *New England Journal of Medicine* **354**, 2473–2483 (8th June 2006).
11. Gong, I. H., Hwang, J., Choi, D. K., Lee, S. R., Hong, Y. K., Hong, J. Y., Park, D. S. & Jeon, H. G. Relationship Among Total Kidney Volume, Renal Function and Age. *The Journal of Urology* **187**, 344–349 (Jan. 2012).
12. Di Leo, G., Di Terlizzi, F., Flor, N., Morganti, A. & Sardanelli, F. Measurement of Renal Volume Using Respiratory-Gated MRI in Subjects without Known Kidney Disease: Intraobserver, Interobserver, and Interstudy Reproducibility. *European Journal of Radiology* **80**, e212–e216 (1st Dec. 2011).
13. Bae, K. T., Commean, P. K. & Lee, J. Volumetric Measurement of Renal Cysts and Parenchyma Using MRI: Phantoms and Patients with Polycystic Kidney Disease. *Journal of Computer Assisted Tomography* **24**, 614–619 (July–Aug. 2000).
14. Zöllner, F. G., Svarstad, E., Munthe-Kaas, A. Z., Schad, L. R., Lundervold, A. & Rørvik, J. Assessment of Kidney Volumes From MRI: Acquisition and Segmentation Techniques. *American Journal of Roentgenology* **199**, 1060–1069 (1st Nov. 2012).
15. Sharma, K., Caroli, A., Quach, L. V., Petzold, K., Bozzetto, M., Serra, A. L., Remuzzi, G. & Remuzzi, A. Kidney Volume Measurement Methods for Clinical Studies on Autosomal Dominant Polycystic Kidney Disease. *PLOS ONE* **12**, e0178488 (30th May 2017).
16. Simms, R. J. *et al.* A Rapid High-Performance Semi-Automated Tool to Measure Total Kidney Volume from MRI in Autosomal Dominant

## 5.8. References

---

- Polycystic Kidney Disease. *European Radiology* **29**, 4188–4197 (1st Aug. 2019).
- 17. Cheong, B., Muthupillai, R., Rubin, M. F. & Flamm, S. D. Normal Values for Renal Length and Volume as Measured by Magnetic Resonance Imaging. *Clinical Journal of the American Society of Nephrology* **2**, 38–45 (1st Jan. 2007).
  - 18. Spithoven, E. M. *et al.* Estimation of Total Kidney Volume in Autosomal Dominant Polycystic Kidney Disease. *American Journal of Kidney Diseases* **66**, 792–801 (1st Nov. 2015).
  - 19. Seuss, H. *et al.* Development and Evaluation of a Semi-Automated Segmentation Tool and a Modified Ellipsoid Formula for Volumetric Analysis of the Kidney in Non-Contrast T2-Weighted MR Images. *Journal of Digital Imaging* **30**, 244–254 (1st Apr. 2017).
  - 20. Magistroni, R., Corsi, C., Martí, T. & Torra, R. A Review of the Imaging Techniques for Measuring Kidney and Cyst Volume in Establishing Autosomal Dominant Polycystic Kidney Disease Progression. *American Journal of Nephrology* **48**, 67–78 (2018).
  - 21. Coulam, C. H., Bouley, D. M. & Sommer, F. G. Measurement of Renal Volumes with Contrast-Enhanced MRI. *Journal of Magnetic Resonance Imaging* **15**, 174–179 (2002).
  - 22. Karstoft, K., Lødrup, A. B., Dissing, T. H., Sørensen, T. S., Nyengaard, J. R. & Pedersen, M. Different Strategies for MRI Measurements of Renal Cortical Volume. *Journal of Magnetic Resonance Imaging* **26**, 1564–1571 (2007).
  - 23. Gloger, O., Tonnies, K. D., Liebscher, V., Kugelmann, B., Laqua, R. & Volzke, H. Prior Shape Level Set Segmentation on Multistep Generated Probability Maps of MR Datasets for Fully Automatic Kidney Parenchyma Volumetry. *IEEE Transactions on Medical Imaging* **31**, 312–325 (Feb. 2012).
  - 24. Kim, Y. *et al.* Automated Segmentation of Kidneys from MR Images in Patients with Autosomal Dominant Polycystic Kidney Disease. *Clin-*

## 5.8. References

---

- ical Journal of the American Society of Nephrology* **11**, 576–584 (7th Apr. 2016).
25. Ronneberger, O., Fischer, P. & Brox, T. *U-Net: Convolutional Networks for Biomedical Image Segmentation* in *Medical Image Computing and Computer-Assisted Intervention – MICCAI 2015* (eds Navab, N., Hornegger, J., Wells, W. M. & Frangi, A. F.) (Springer International Publishing, Cham, 2015), 234–241. doi:10.1007/978-3-319-24574-4\_28.
  26. Lu, F., Wu, F., Hu, P., Peng, Z. & Kong, D. Automatic 3D Liver Location and Segmentation via Convolutional Neural Network and Graph Cut. *International Journal of Computer Assisted Radiology and Surgery* **12**, 171–182 (1st Feb. 2017).
  27. Sharma, K., Rupprecht, C., Caroli, A., Aparicio, M. C., Remuzzi, A., Baust, M. & Navab, N. Automatic Segmentation of Kidneys Using Deep Learning for Total Kidney Volume Quantification in Autosomal Dominant Polycystic Kidney Disease. *Scientific Reports* **7**, 2049 (1 17th May 2017).
  28. Wachinger, C., Reuter, M. & Klein, T. DeepNAT: Deep Convolutional Neural Network for Segmenting Neuroanatomy. *NeuroImage. Segmenting the Brain* **170**, 434–445 (15th Apr. 2018).
  29. Fu, Y. *et al.* A Novel MRI Segmentation Method Using CNN-Based Correction Network for MRI-Guided Adaptive Radiotherapy. *Medical Physics* **45**, 5129–5137 (2018).
  30. Hassanzadeh, T., Hamey, L. G. C. & Ho-Shon, K. Convolutional Neural Networks for Prostate Magnetic Resonance Image Segmentation. *IEEE Access* **7**, 36748–36760 (2019).
  31. Li, X., Chen, H., Qi, X., Dou, Q., Fu, C.-W. & Heng, P.-A. H-DenseUNet: Hybrid Densely Connected UNet for Liver and Tumor Segmentation From CT Volumes. *IEEE Transactions on Medical Imaging* **37**, 2663–2674 (Dec. 2018).
  32. Kline, T. L. *et al.* Performance of an Artificial Multi-Observer Deep Neural Network for Fully Automated Segmentation of Polycystic Kidneys. *Journal of Digital Imaging* **30**, 442–448 (1st Aug. 2017).

## 5.8. References

---

33. Van Gastel, M. D. A., Edwards, M. E., Torres, V. E., Erickson, B. J., Gansevoort, R. T. & Kline, T. L. Automatic Measurement of Kidney and Liver Volumes from MR Images of Patients Affected by Autosomal Dominant Polycystic Kidney Disease. *Journal of the American Society of Nephrology* **30**, 1514–1522 (1st Aug. 2019).
34. Shin, T. Y. *et al.* Expert-Level Segmentation Using Deep Learning for Volumetry of Polycystic Kidney and Liver. *Investigative and Clinical Urology* **61**, 555–564 (Nov. 2020).
35. Fukushima, K. Neocognitron: A Hierarchical Neural Network Capable of Visual Pattern Recognition. *Neural Networks* **1**, 119–130 (1st Jan. 1988).
36. Lecun, Y., Bottou, L., Bengio, Y. & Haffner, P. Gradient-Based Learning Applied to Document Recognition. *Proceedings of the IEEE* **86**, 2278–2324 (Nov. 1998).
37. Petzold, K. *et al.* Building a Network of ADPKD Reference Centres across Europe: The EuroCYST Initiative. *Nephrology Dialysis Transplantation* **29**, iv26–iv32 (suppl\_4 1st Sept. 2014).
38. Will, S., Martirosian, P., Würslin, C. & Schick, F. Automated Segmentation and Volumetric Analysis of Renal Cortex, Medulla, and Pelvis Based on Non-Contrast-Enhanced T1- and T2-Weighted MR Images. *Magnetic Resonance Materials in Physics, Biology and Medicine* **27**, 445–454 (1st Oct. 2014).
39. Rorden, C. *NeuroLabusc/MRIcron* 18th Jan. 2021.
40. Chollet, F. *Keras* version 2.2.4. Keras, 2015.
41. Abadi, M. *et al.* TensorFlow: Large-Scale Machine Learning on Heterogeneous Distributed Systems, 19 (9th Nov. 2015).
42. Mahapatra, D. & Buhmann, J. M. Visual Saliency-Based Active Learning for Prostate Magnetic Resonance Imaging Segmentation. *Journal of Medical Imaging* **3**, 014003 (Feb. 2016).
43. Chen, J., Yang, L., Zhang, Y., Alber, M. & Chen, D. Z. in *Advances in Neural Information Processing Systems* 29 (eds Lee, D. D., Sugiyama, M.,

## 5.8. References

---

- Luxburg, U. V., Guyon, I. & Garnett, R.) 3036–3044 (Curran Associates, Inc., 2016).
44. Stollenga, M. F., Byeon, W., Liwicki, M. & Schmidhuber, J. in *Advances in Neural Information Processing Systems 28* (eds Cortes, C., Lawrence, N. D., Lee, D. D., Sugiyama, M. & Garnett, R.) 2998–3006 (Curran Associates, Inc., 2015).
45. Van Gastel, M. D. A. *et al.* T1 vs. T2 Weighted Magnetic Resonance Imaging to Assess Total Kidney Volume in Patients with Autosomal Dominant Polycystic Kidney Disease. *Abdominal Radiology* **43**, 1215–1222 (1st May 2018).
46. Morris, D., Donnelly, M., Gifford, F., Dunne, P., Hayes, P., Simpson, K., Fallowfield, J. & Semple, S. *Segmentation of the Cortex and Medulla in Multiparametric Magnetic Resonance Images of the Kidney Using K-Means Clustering* in *Proc. Intl. Soc. Mag. Reson. Med.* 27 ISMRM. **27** (Montreal, 13th May 2019), 1915.

# Chapter 6

## Ex-Vivo Renal MRI

### Abstract

This work was presented as a digital poster at the International Society of Magnetic Resonance in Medicine (ISMRM) 27th Annual Meeting, 2019 [1] and as a poster at United Kingdom Kidney Week (UKKW) 2019 [2]. The bespoke analysis pipelines and software developed here were heavily drawn upon in the development of The United Kingdom Renal Imaging Network (UKRIN) Kidney Analysis Toolbox (UKAT) [3]. This work has also been accepted to be presented at the ISMRM 29th Annual Meeting, 2021, [4].

## 6.1 Introduction

A recurring theme in renal Magnetic Resonance Imaging (MRI) studies are the limitations imposed by respiratory motion. Sequences must either be optimised and accelerated to fit within a breath-hold, be hugely slowed down through the use of respiratory triggering or accept the motion artefacts that are inevitable during free-breathing acquisition. Additionally the common trade-off in MRI between voxel size, Field Of View (FOV) and acquisition time becomes all the more limiting within the constraints of respirator motion. While these issues are ever-present in day-to-day clinical practice, they also impeded progress, and ultimately, clinical adoption, of techniques in the research phases of their development. Often in research, it is desirable to acquire data of higher quality than would be required in clinical practice. This can be to gain a better understanding of the spacial variance within small structures or acquire best case scenario data with many averages/time points to compare to existing, non-imaging, diagnostic techniques.

In this chapter, techniques for ex-vivo renal MRI are developed. These allow research to be conducted without the limitations imposed by respiratory motion and, in future, could be used in the clinic to assess allograft viability prior to transplant.

### 6.1.1 Validation of Multiparametric MRI via a Nephrectomy Model

Blood and urine tests are commonly used to assess renal health and function however, these are indirect measures and give no indication as to the health of individual kidneys. Consequently, the gold standard in renal diagnostics is a biopsy followed by histological analysis. During a renal biopsy, an area on the patient's back is injected with local anaesthetic then, using ultrasound as a guide, a biopsy needle is inserted into the kidney to remove a

## 6.1. Introduction

---

sample of the tissue. Acquiring the biopsy takes approximately half an hour. The patient is then asked to lie in bed for several hours to minimise the risk of internal bleeding. In approximately 1% of patients, the bleeding caused will require a blood transfusion and approximately 0.5% of patients will require embolisation. While these risks are relatively small, the procedure is still an invasive, destructive and time consuming one for the patient thus making it poorly suited for longitudinal monitoring of renal health. Additionally, this method of biopsy is not viable for some patients such as those with coagulopathy or thrombocytopenia due to the increased risk if a hemorrhage occurs or those that are unable to lie prone such as patients who are intubated for respiratory assistance [5]. While techniques such as the transjugular renal biopsy have been developed (albeit accidentally after taking a wrong turn at the portal vein while trying to acquire a liver biopsy [6]) to serve these patients, this is a more technically complicated procedure. Finally, the samples acquired via biopsy are very small and thus are often not representative of the entirety of the kidney biopsied, let alone both kidneys.

These drawbacks have provided the incentive for the development of multiparametric renal MRI protocols which could prove to be advantageous for both clinicians and patients. A key aspect in the widespread adoption of MRI into renal clinical practice, is a full understanding of the interplay between the current histological pipelines and the newly developed MRI measurements. While it is possible to correlate biopsy results with MRI findings and gain some information as to how different MRI measurements vary with tissue properties, this paradigm still suffers from the small tissue sampling volumes outlined above and the inherent difficulties of in-vivo MRI data acquisition [7]. An alternative paradigm is to scan the kidney in-vivo to collect typical renal MRI data, scan the organ ex-vivo to acquire exquisite MRI data of a far higher quality than would be possible in-vivo, then perform whole organ histology on the tissue. These three streams of complimentary data, all acquired from the same organ, eliminate the large issues with currently implemented paradigms, while still being able to reference the data back to clinically feasible measures.

## 6.1. Introduction

---

One of the first works correlating multiparametric MRI with renal histology was by Inoue *et al*, who found a statistically significant correlation between fibrosis area, as determined from a renal biopsy stained with Masson's trichrome, and Apparent Diffusion Coefficient (ADC) and  $T_2^*$  in 37 Chronic Kidney Disease (CKD) patients [8]. This was confirmed by Zhao *et al*, who found a strong correlation between ADC of both the renal cortex and medulla and histopathological fibrosis score on 25 more CKD patients [9]; this study used a more comprehensive histopathology protocol. Feng *et al* also found a correlation between glomerulosclerosis, fibrosis, Fractional Anisotropy (FA) and ADC in CKD subjects [10]. Friedli *et al* found a significant correlation between cortical-medullary differences in  $T_1$  and ADC and fibrosis, this was first found in rats, including histology of whole organs rather than just biopsy samples [11]. The same group then validated this finding in 164 human subjects, correlating with biopsy rather than whole organ [12].

Outside the renal community, work has been done with registered whole-mount histology and both in-vivo and ex-vivo MRI. Jafari *et al* have performed volume matched ex-vivo Quantitative Susceptibility Mapping (QSM) and  $T_2^*$  mapping with whole explant histopathology using the histopathology results to validate predictions of fibrosis using MRI [13]. The University of British Columbia group have carried out extensive work correlating histopathology of whole prostatectomy samples with in-vivo MRI [14, 15]. The same group have also made use of ex-vivo scanning techniques to correlate histopathology with 3T in-vivo data and 7T narrow-bore ex-vivo data [16]. The use of matched histology and MRI data is well established in the neuroimaging field [17] with studies correlating histopathology with diffusion measures [18–21], magnetisation transfer [22, 23], QSM [24, 25] and relaxometry measures [26, 27]. Additionally, post processing packages have been developed to enable accurate registration of whole mount histopathology and MRI data [28, 29].

Thus far, no work has been found comparing whole organ renal histology to in-vivo and ex-vivo MRI measurements. The ideal paradigm for this work

## **6.1. Introduction**

---

is to scan patients who are undergoing a nephrectomy as part of their standard clinical care. Briefly, this method would involve scanning a subject pre-operation to acquire a multi-parametric quantitative MRI dataset. The subject will then have part of their kidney removed, cancerous tissue will be sent for standard lab tests however, non-cancerous tissue will be immersion fixed in formalin. Equivalent scans assessing the same quantitative parameters as were collected in-vivo will be repeated ex-vivo, however these scans will be at a much higher resolution. Finally, the tissue will be sliced for multi-stain histopathology. This pipeline enables the comparison of tried and tested histological staining that clinicians are used to, albeit with larger sample sizes, with in-vivo quantitative MRI data; ex-vivo data acts as an intermediary between histology and in-vivo MRI data.

Given the purpose of this paradigm is to compare pre-existing histological analysis with newly developed, but previously documented renal MRI protocols, the area that will need the most development is the use of ex-vivo MRI to image renal tissue.

### **6.1.2 Assessment of Allograft Viability**

### **6.1.3 Ex-Vivo Protocol Aims**

To enable research into these topics, a range of ex-vivo acquisition techniques with matched in-vivo counterparts was developed with the following aims.

- Can be run on widely available hospital hardware
- Not take forever
- Not need custom coils etc
- Not time dependent i.e. can scan at any time in a 12 hour window

## 6.2 MRI Protocol Development

As one of the aims in this chapter is for the protocol developed to be able to be performed in a hospital environment, the decision to develop the protocol for use on human scanners rather than pre-clinical scanners was made. Although some hospitals are attached to research institutions with access to pre-clinical MRI scanners, this is not the norm. Imaging was performed on a 3T Philips Ingenia system as 3T scanners are available in most European/North American hospitals however some protocols were also developed for a 7T Philips Achieva system to assess the best case scenario ex-vivo images that could be acquired on human scanners, all in-vivo imaging was performed at 3T. All ex-vivo samples were scanned in 32 channel head coils, Figure 6.1, as these coils allowed for a whole organ to be imaged while also keeping array elements as close to the signal as possible. In-vivo imaging utilised a 16-channel anterior coil array and 16-channel posterior coil array.



Figure 6.1: A sample sat within the 32 channel 3T head coil.

One of the aims of the ex-vivo protocol is to minimise time outside the body as a confounding factor. This enables a greater degree of flexibility with regards to scan times and even order of scans within the protocol. Tissue degradation occurs relatively quickly after removal from the body and as such the tissue was fixed to minimise this process. Samples were transported in Phosphate-buffered Saline (PBS) then transferred into ten times the samples volume of 10% Neutral Buffered Formalin (NBF) for twenty four hours. After

## **6.2. MRI Protocol Development**

---

fixation the samples were washed and rehydrated with PBS and remain in this solution while being scanned to minimise susceptibility artefacts that would be too substantial if the sample were scanned either in air or the NBF. All samples were scanned at room temperature ( $\sim 20^{\circ}\text{C}$ ).

Development work was performed on porcine kidney samples as these are an excellent analogue for human kidneys. Initially, samples were acquired from a local slaughterhouse however these samples were of variable quality. This was largely due to the legislation surrounding animals destined to enter the human food chain. If any part of the animal is to be consumed by humans, the carcase must be thoroughly inspected before any tissue can be released. This causes two problems. As part of the inspection, the kidneys need to be examined for parasites, this is done by making an incision in the organ, however the quality of this incision can vary massively with some samples having a neat 20 mm slice cut into them while others are roughly cut in half. The second issue is caused by the variable time between slaughter and the tissue being released after inspection. No preservation techniques, such as storing the kidneys on ice, are employed during the wait for tissue release and as such, the tissue can begin to degrade in this variable and unknown time period.

These issues meant later samples were procured from University of Nottingham Veterinary Science department. The animals slaughtered here are not destined for human consumption and as such the kidneys can be placed into PBS and subsequently NBF far quicker, additionally the kidneys do not need to be sliced open for inspection. The difference in quality of samples acquired from the slaughterhouse and Veterinary Science can clearly be seen in Figure 6.2. The collaboration with Veterinary Science also enables the procurement of a more diverse range of samples such as kidneys from pigs of different ages and therefore different degrees of fibrosis or from animals with induced Acute Kidney Injury (AKI).

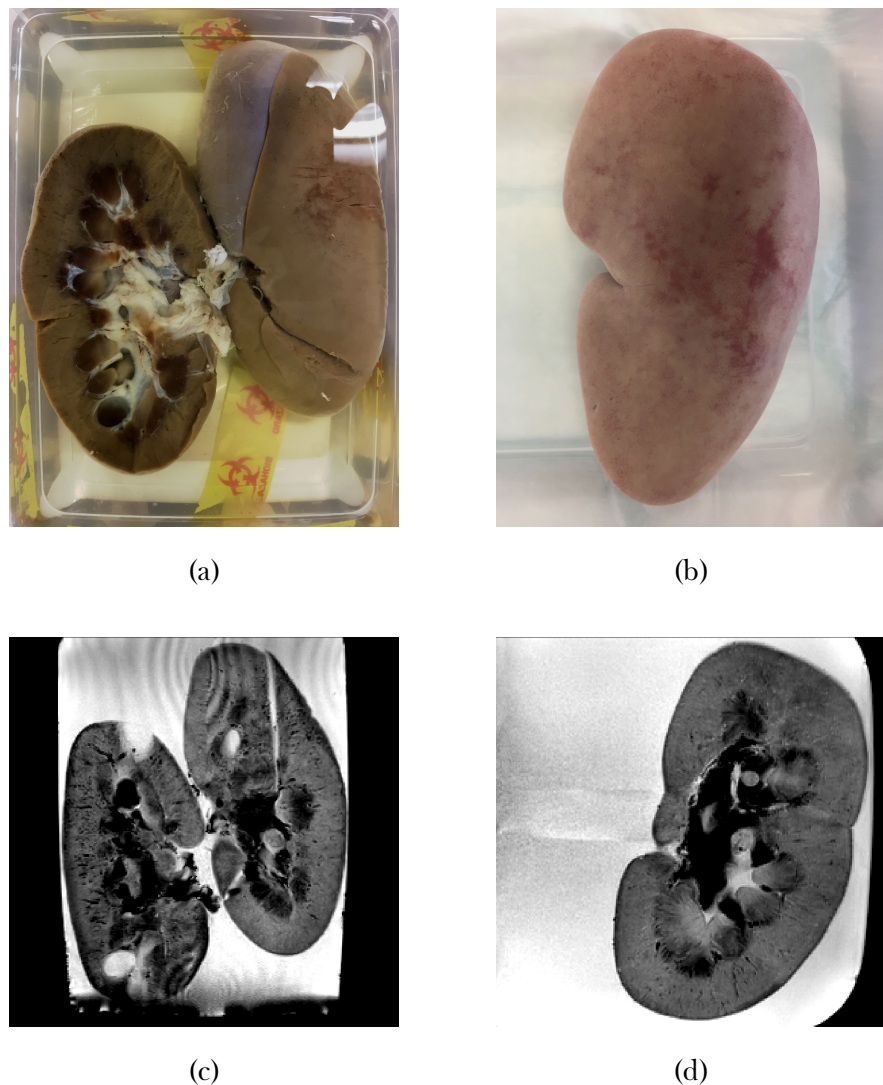


Figure 6.2: (a) An example of a sample procured from the slaughterhouse after it has been fixed. The left hand kidney has been sliced in half; the right hand kidney has the incisions from the meat inspector clearly visible. (b) An example of a sample procured from Veterinary Science post fixing. (c) An example of a  $T_2$  weighted Fast Field Echo (FFE) with TE = 40 ms of a kidney procured from the slaughterhouse. (d) An example of a  $T_2$  weighted FFE with TE = 40 ms of a kidney procured from Veterinary Science.

### 6.2.1 Anatomical Scans

To make use of the layer based analysis techniques outlined in Section 6.4 and calculate Total Kidney Volume (TKV) a high resolution, whole kidney

## 6.2. MRI Protocol Development

---

coverage anatomical scan is required to segment the kidney from surrounding tissue/PBS. In-vivo, the  $T_2$  weighted structural scan from Chapter 5 is used. The ex-vivo protocol is outlined in Table 6.1; this scan was also used to plan subsequent ex-vivo scans.

Parameter	3T Ex-Vivo	3T In-Vivo
Voxel Size	1 x 1 x 1	1.5 x 1.5 x 5
FoV	192 x 192 x 60	350 x 350 x 71
Acquisition Mode	3D	M2D
TE	3.7	60
TR	8.1	1300
Flip Angle	15	90
Bandwidth	191.5	792.3
NSA	1	1
Fold-over Suppression Oversampling	N/A	150
Sense	2 RL, 2AP	2.5
Halfscan	0.625	N/A
Fast Imaging Mode	TFE	TSE
TFE Factor	143	N/A
Shot Interval	4000	N/A
Acquisition Time	53 sec	17 sec (1 x BH)

Table 6.1: Acquisition parameters for anatomical scans.

### 6.2.2 $T_1$ Mapping

$T_1$  mapping protocols were developed for both 3T and 7T systems using an ultrafast gradient echo inversion recovery scheme. The basics of this sequence and  $T_1$  mapping are outlined in Section 2.2.1. An example of the acquisitions at each inversion time is shown in Figure 6.3. The sequence parameters at both 3T and 7T are shown in Table 6.2.

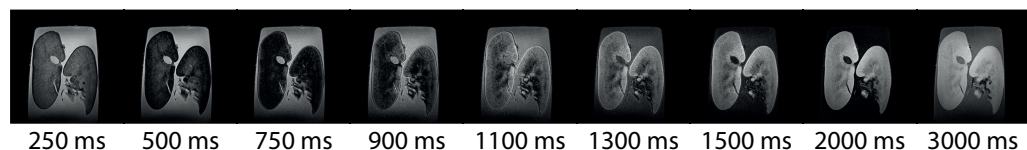


Figure 6.3: Acquisitions at each of the Inversion Time (TI) at 7T.

## 6.2. MRI Protocol Development

---

Parameter	3T Ex-Vivo	7T Ex-Vivo	3T In-Vivo
Voxel Size	0.7 x 0.7 x 1.0	0.6 x 0.6 x 0.6	3 x 3 x 5
FoV	160 x 160 x 50	192 x 170 x 24	288 x 288 x 25
Acquisition Mode	3D	3D	MS
TE	5.1		27
TR	11		5000
TI	400, 500, 750, 900, 1100, 1300, 1500, 2000, 2600	250, 500, 750, 900, 1100, 1300, 1500, 2000, 3000	0, 100, 200, 300, 400, 500, 600, 700, 800, 900, 1000, 1100, 1300
Flip Angle	8	8	90
Bandwidth	134.4		39.3
NSA	1	2	1
Fold-over Suppression Oversampling	75	N/A	N/A
Sense	2.5 RL, 1 AP	2 RL, 1.5 AP	2.3
Halfscan	N/A	N/A	0.851
Fast Imaging Mode	TFE	TFE	EPI
TFE Factor	64	240	N/A
Shot Interval	3000	8000	N/A
Acquisition Time	1 hr 20 min 20 sec		1 min 10 sec (Trig)

Table 6.2:  $T_1$  mapping protocols and 3T and 7T.

After a  $180^\circ$  inversion, the signal sampled at each inversion time is proportional to the modulus of the true longitudinal magnetisation, as such, the true dynamic range of the inversion recovery is not sampled. This factor means there is ambiguity as to the polarity of signals near the null point (zero crossing) and can lead to a decreased accuracy when fitting for  $T_1$  as any algorithm is essentially having to fit an extra parameter in the form of the null point.

If the phase of the signal has been saved, the polarity of the magnitude can be corrected using the methods of Szumowski *et al* [30] thus increasing accuracy by increasing dynamic range and removing ambiguity as to the location of the null point for each voxel. Phase data is only accurate if partial Four-

## 6.2. MRI Protocol Development

---

ier acquisition acceleration techniques (Section 2.3.2), known as halfscan, are not utilised however, because these acceleration methods result in a decreased Signal to Noise Ratio (SNR) they would not be used ex-vivo anyway.

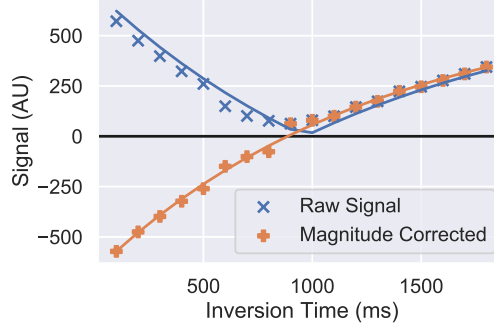


Figure 6.4: The raw signal recorded from a single voxel and the magnitude corrected signal with increased dynamic range.

Once the data has been polarity corrected, a voxel by voxel, least squares trust region reflective method is used to fit the data from each voxel to Equation (6.1) to estimate the  $T_1$  and  $M_0$  of the tissue and an uncertainty in the fit [31].

$$S(TI) = M_0 \left( 1 - 2 \cdot e^{-TI/T_1} \right) \quad (6.1)$$

Using these techniques, the  $T_1$  of ex-vivo samples could be calculated at both 3T and 7T, Figure 6.5. For in-vivo acquisitions, halfscan was used and as such magnitude correction could not be employed. As such, in-vivo data was fit to the modulus of Equation (6.1).

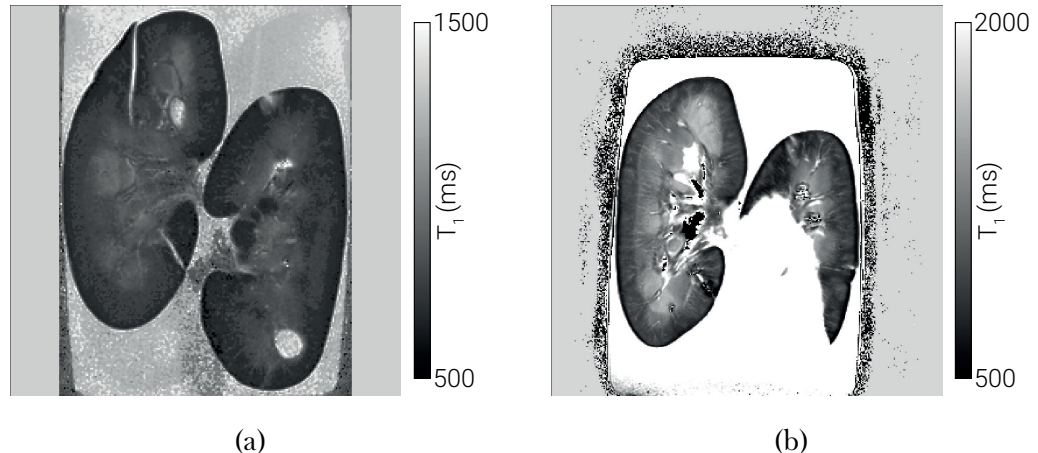


Figure 6.5: Example  $T_1$  maps generated at both 3T (a) and 7T (b).

### 6.2.3 $T_2$ Mapping

$T_2$  mapping makes use of the Gradient Spin Echo (GrASE) sequence developed in Chapter 3. This sequence was only implemented at 3T, an example of the acquisitions at each Echo Time (TE) is shown in Figure 6.6 and the sequence parameters are shown in Table 6.3. The very wide range of TE sampled ex-vivo will enable future multi-exponential analysis of the data allowing for a more accurate quantification of the long  $T_2$  components of the tissue [14, 32].

## 6.2. MRI Protocol Development

---

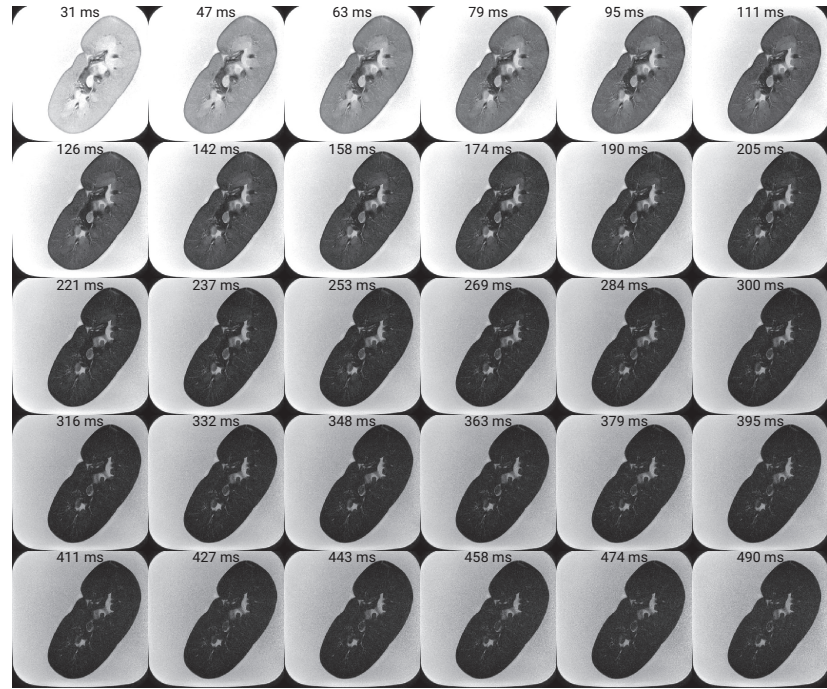


Figure 6.6: Acquisitions of an ex-vivo sample at each of the TE.

Parameter	3T Ex-Vivo	3T In-Vivo
Voxel Size	0.7 x 0.7 x 1.0	3 x 3 x 5
FoV	160 x 160 x 20	288 x 288 x 25
Acquisition Mode	MS	MS
TE	31:15.8:489.9	11:5.6:179
TR	3000	3000
Flip Angle	90	90
Bandwidth	118.9	427.9
NSA	2	1
Fold-over Suppression Oversampling	75	66
Sense	2.55	2.55
Halfscan	N/A	N/A
Fast Imaging Mode	GraSE	GraSE
TFE Factor	30	30
EPI Factor	3	3
Startup Echoes	1	1
Acquisition Time	30 min 30 sec	3 min 9 sec (Trig)

Table 6.3:  $T_2$  mapping sequence parameters.

$T_2$  maps are generated on a voxel by voxel basis using a least squares trust region reflective methods to fit the data to Equation (6.2) to estimate  $T_2$  and

## 6.2. MRI Protocol Development

---

$M_0$ .

$$S(TE) = M_0 \cdot e^{-TE/T_2} \quad (6.2)$$

As outlined in Section 3.3.1 multiple methods of estimating  $T_2$  were compared with the basic two parameter fit delivering the most desirable results. Using this pipeline,  $T_2$  maps could be generated, an example of which is shown in Figure 6.7. While partial voluming has been minimised by keeping voxel sizes small, the use of multi-exponential fitting models should be explored in future. This would allow the long  $T_2$  components of the signal, such as the signal from PBS to be modelled separately to the renal tissue, thus increasing accuracy.

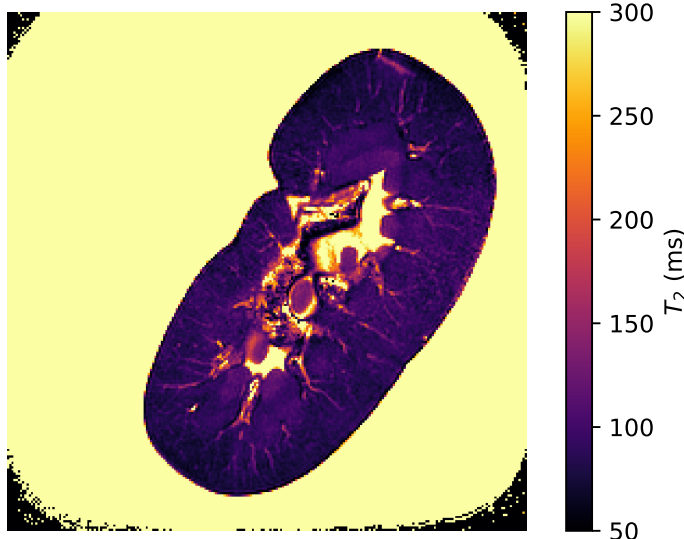


Figure 6.7: An example ex-vivo  $T_2$  map acquired using the scheme above. This sample had been formalin fixed and stored in PBS for multiple months, hence the lack of contrast between cortical and medullary tissue.

### 6.2.4 $T_2^*$ Mapping

$T_2^*$  acquisition is performed using a simple multi-slice gradient echo sequence as outlined in Section 2.2.2 and was developed at both 3T and 7T. The acquisition parameters are shown in Table 6.4. In addition to the magnitude data saved for  $T_2^*$  mapping, the phase data is also saved to allow a QSM

## 6.2. MRI Protocol Development

---

pipeline to be developed in future.

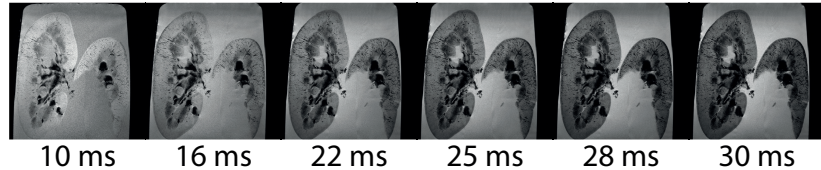


Figure 6.8: Acquisitions at each of the TE at 7T.

Parameter	3T Ex-Vivo	7T Ex-Vivo	3T In-Vivo
Voxel Size	0.7 x 0.7 x 1.0	0.5 x 0.5 x 1	1.5 x 1.5 x 5
FoV	160 x 160 x 25	145 x 145 x 10	288 x 288 x 25
Acquisition Mode	MS	MS	MS
TE	15:5:50	10, 13, 16, 19, 22, 25, 28, 30	5:3:38
TR	697		79
Flip Angle	38	38	25
Bandwidth	35 - 56		1328.6
NSA	1	3	1
Fold-over Suppression Oversampling	75	N/A	144
Sense	2	2	2
Halfscan	N/A	N/A	N/A
Fast Imaging Mode	None	None	None
Acquisition Time	46 min 25 sec		47 sec (3 x BH)

Table 6.4: Acquisition parameters for  $T_2^*$  mapping sequences at 3T and 7T.

Estimation of  $T_2^*$  can be performed via two different methods, fitting to a two parameter exponential (Equation (6.3)) or performing a weighted linear fit to the natural logarithm of the signal. The latter of these methods is far less computationally intensive and as such, runs much quicker.

$$S(TE) = M_0 \cdot e^{-TE/T_2^*} \quad (6.3)$$

The acquisition parameters of the 3T ex-vivo protocol were simulated to

## 6.2. MRI Protocol Development

---

compare the two fitting methods using Monte Carlo techniques. The linear fit produces a slightly greater Coefficient of Variation (CoV) than the exponential fit at lower  $T_2^*$ , Figure 6.9a. Additionally, the relative error, defined by Equation (6.4), has a greater magnitude below 20 ms when fitting with the linear fit than the exponential fit, Figure 6.9b. The  $T_2^*$  we expect from the kidneys at 3T is greater than 20 ms so in the interests of computational efficiency, the linear fitting method was used.

$$\text{Relative Error} = \frac{t_{2 \text{ fit}}^* - t_{2 \text{ simulated}}^*}{t_{2 \text{ simulated}}^*} \quad (6.4)$$

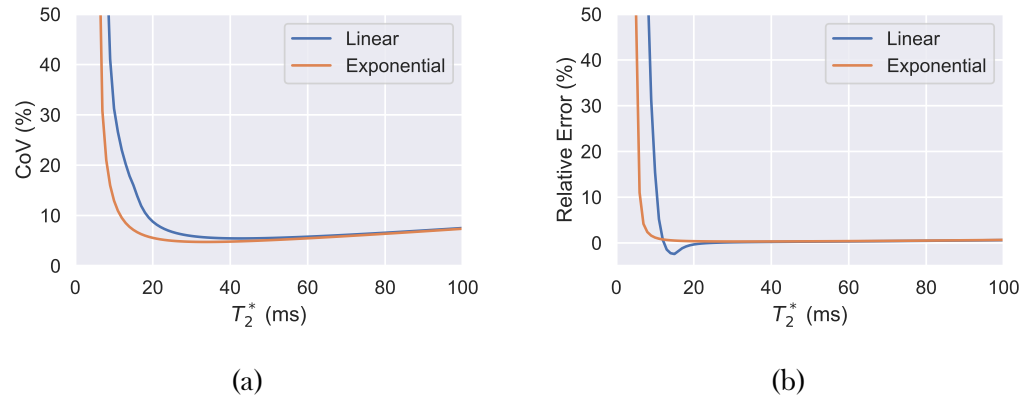


Figure 6.9: Simulations to ascertain the accuracy of each  $T_2^*$  fitting algorithm over a range of  $T_2^*$ .

Using the acquisition and post processing steps above,  $T_2^*$  maps can be generated, examples of which are shown in Figure 6.10.

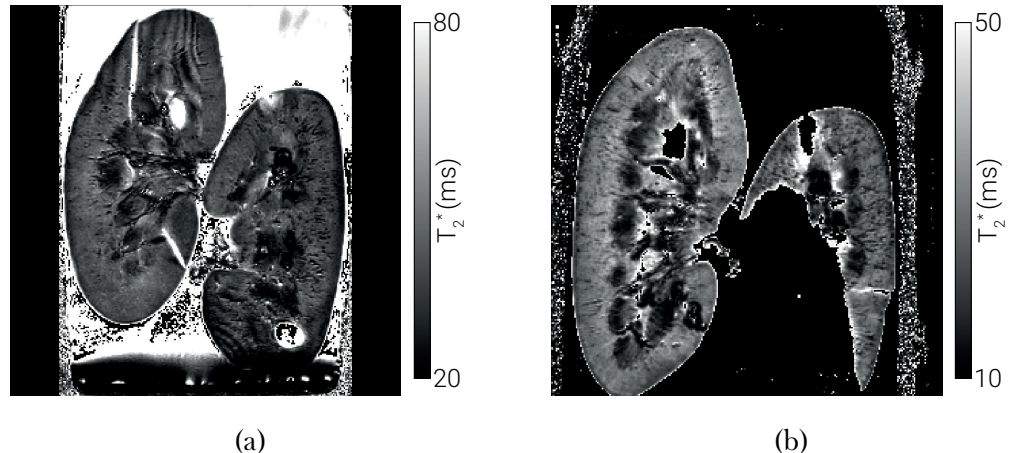


Figure 6.10: An example  $T_2^*$  map acquired at 3T (a) and 7T (b) fit using the weighted fit to the natural logarithm of the signal.

### 6.2.5 Apparent Diffusion Coefficient Mapping

The underlying principles of diffusion imaging are outlined in Section 2.2.4, here Diffusion Weighted Imaging (DWI) is performed using a single shot Spin Echo (SE)-Echo Planar Imaging (EPI) sequence over a range of b-values applied in three orthogonal directions. By acquiring diffusion gradients in three different directions and calculating the mean, the effects of diffusion anisotropy can be minimised. The sequence was developed for 3T systems with a schematic of the sequence shown in Figure 6.11 and the sequence parameters summarised in Table 6.5.

## 6.2. MRI Protocol Development

---

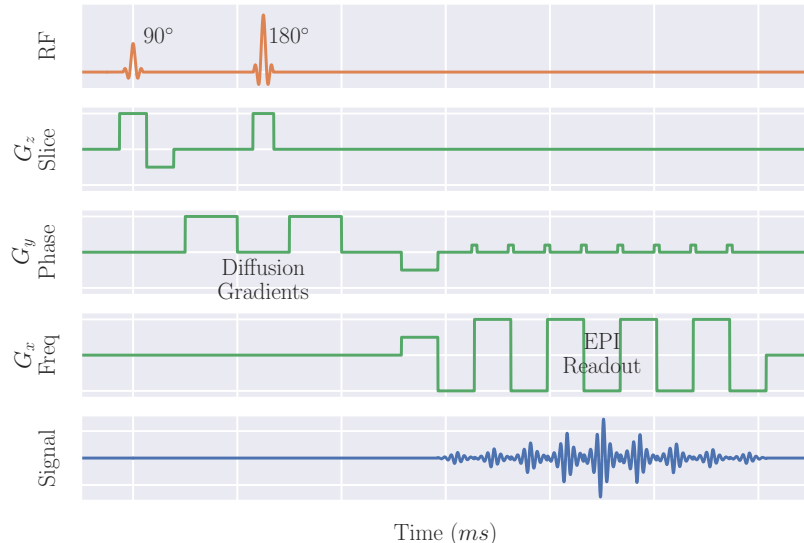


Figure 6.11: A schematic of the SE-EPI sequence used for ADC mapping. This block is repeated multiple times with diffusion gradients applied in different directions and with different strengths.

Parameter	3T Ex-Vivo	3T In-Vivo
Voxel Size	1.5 x 1.5 x 1.5	1.5 x 1.5 x 5
FoV	160 x 160 x 51	288 x 288 x 25
Acquisition Mode	MS	MS
TE	72	71
TR	1800	1800
b-values	0, 5, 15, 30, 45, 60, 75, 90, 105, 120, 135, 150, 175, 200, 300, 400, 500, 600	0, 5, 15, 30, 45, 60, 75, 90, 105, 120, 135, 150, 175, 200, 300, 400, 500, 600
Flip Angle	90	90
Bandwidth	13.2	13.7
NSA	1	1
Fold-over Suppression Oversampling	75	N/A
Sense	2.3	2.3
Halfscan	0.676	0.676
Fast Imaging Mode	EPI	EPI
EPI Factor	91	83
Phase Encode Direction	L then R	L then R
Acquisition Time	9 min 44 sec	2 min 42 sec (Trig)

Table 6.5: ADC mapping acquisition parameters.

## 6.2. MRI Protocol Development

---

The diffusion sensitising block of the pulse sequence is time consuming and as such necessitates the use of fast image techniques, EPI is the simplest to implement however is not without drawbacks. It suffers from geometric distortions, particularly in the phase encode direction, due to inhomogeneities in the  $B_0$  field cause by susceptibility differences. These geometric distortions can be problematic for this paradigm as the ability to correlate, on a voxel by voxel basis, parameters acquired with different sequences is at the core of multiparametric MRI. Geometric distortions make this impossible. The susceptibility of PBS and renal tissue is similar however there is a very large difference between the PBS and surrounding air and as such, distortions can be problematic.

As the distortions are predominantly in the phase encode direction, by inverting the direction of the phase encode blips, the direction of the distortion can be reversed, Figure 6.12a. By acquiring images with both phase encode directions the underlying field map can be estimated and used to undistort the data [33]. This process can be carried out using fMRI Software Library (FSL) “topup” however, as this tool was designed for work in the brain, a custom configuration to perform more iterations of the field estimation algorithm with a greater degree of regularisation is required.

Although in some cases it is possible to acquire only the b0 image in both phase encode directions, calculate the displacement field, then apply this field to other b-values, it was decided that the  $\sqrt{2}$  SNR increase of acquiring two volumes and averaging them is beneficial. Additionally if, in the case of in-vivo data, there are issues with motion in the b0 volumes, then another diffusion weighting can be used to estimate the displacement, thus adding inherent redundancy to the pipeline.

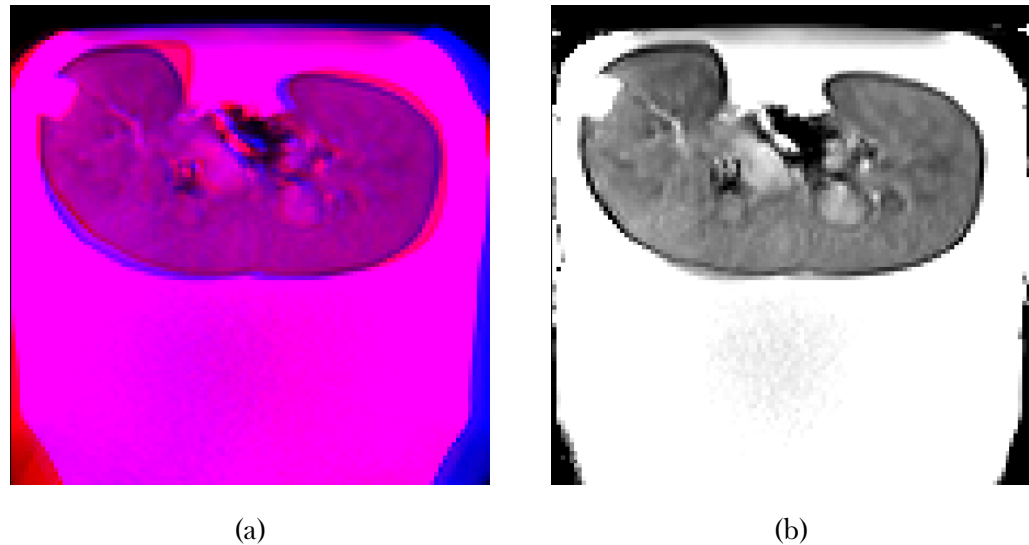


Figure 6.12: (a) b0 images collected with opposing phase encode directions overlay in red and blue. (b) A composite image with EPI distortions corrected using topup.

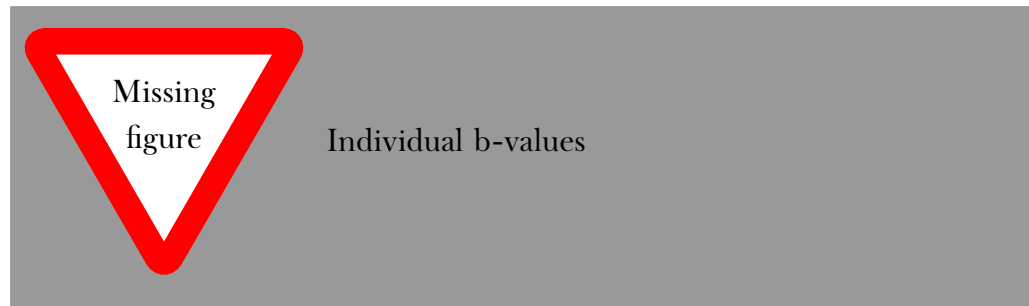


Figure 6.13: Distortion corrected images at each b-value.

The average of the three directions at each b-value and phase encode direction is calculated. EPI distortion correction is performed on both ex-vivo and in-vivo data using topup to enable accurate voxel by voxel comparison of ADC to other quantitative parameters. The natural logarithm of the distortion corrected signal from each voxel over each b-value is taken and a linear least squares fit performed. This enables a quick estimation of ADC and an uncertainty in the fit.

Using these techniques, the ADC of both in-vivo and ex-vivo renal tissue can be calculated, Figure 6.14 with no geometric distortions. Although not

## 6.2. MRI Protocol Development

---

implemented here, the large number of low b-values sampled should make estimations of more advance diffusion parameters possible such as fitting the data to an Intravoxel Incoherent Motion (IVIM) model [34].

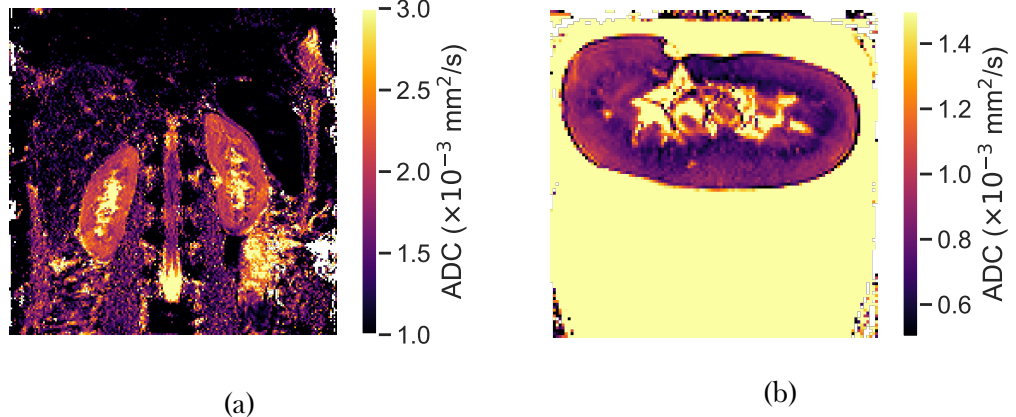


Figure 6.14: ADC maps acquired of both an in-vivo subject (a) and ex-vivo sample (b).

### 6.2.6 Diffusion Tensor Imaging

ADC maps provide an understanding as to how readily molecules can diffuse through a tissue, however they do not provide any information as to what directions the molecules are travelling, to measure this, Diffusion Tensor Imaging (DTI) is used. The renal group at Sir Peter Mansfield Imaging Centre (SPMIC) had no existing high resolution in-vivo (or ex-vivo) DTI protocol, as such this was specifically developed for this paradigm.

The acquisition scheme used is very similar to that in Section 6.2.5, a single shot SE-EPI scheme with monopolar diffusion gradients. The difference lies in the fact that, rather than acquiring a large range of b-values over three different directions, only a  $b_0$  and one other b-value are acquired over a minimum of six directions although in practice, many more. This is known as a single shell DTI scheme. As the diffusivity in, for example, the positive  $x$  direction is the same as the negative  $x$  direction most DTI schemes acquire a hemisphere of directions, however, to apply additional image deformation

## 6.2. MRI Protocol Development

---

correction techniques outlined below, diffusion vectors were acquired over a full sphere, Figure 6.15.

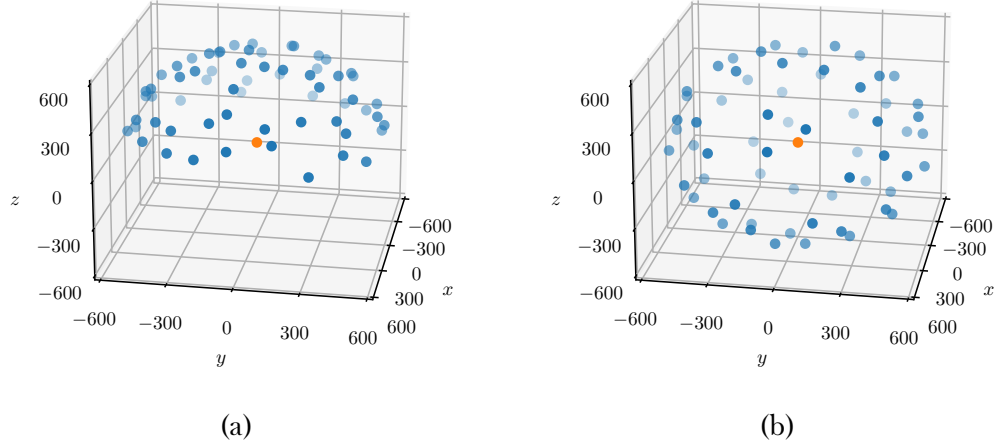


Figure 6.15: (a) 64 diffusion directions acquired over a hemisphere (b) 64 diffusion directions acquired over a full sphere as used in this chapter.  $b_0$  is shown in orange with subsequent  $b$ -values shown in blue.

Mathematically, DTI is estimating the tensor,  $\mathcal{D}$  in equation (6.5) where  $D_{xx}$ ,  $D_{yy}$  and  $D_{zz}$  represent diffusivity along the  $x$ ,  $y$  and  $z$  directions in the lab frame and are equivalent to the three directions sampled in Section 6.2.5.  $D_{yx}$ ,  $D_{zx}$  and  $D_{zy}$  represent diffusivity between the principle axis of the lab frame, as  $\mathcal{D}$  is symmetric,  $D_{yx} \equiv D_{xy}$ ,  $D_{zx} \equiv D_{xz}$  etc, hence DTI can be performed by only sampling a hemisphere of diffusion vectors.

$$\mathcal{D} = \begin{bmatrix} D_{xx} & D_{xy} & D_{xz} \\ D_{yx} & D_{yy} & D_{yz} \\ D_{zx} & D_{zy} & D_{zz} \end{bmatrix} \quad (6.5)$$

Like the ADC sequence, a full dataset is acquired with both opposing phase encode directions to assist with geometric distortion correction. A summary of the sequence parameters is shown in Table 6.6.

## 6.2. MRI Protocol Development

---

Parameter	3T Ex-Vivo	3T In-Vivo
Voxel Size	2.3 x 2.3 x 2.3	3 x 3 x 3
FoV	160 x 160 x 51	288 x 288 x 60
Acquisition Mode	MS	MS
TE	85	82
TR	5100	5100
b-values	0, 600	0, 600
Directions	128	64
Flip Angle	90	90
Bandwidth	17.1	30.5
NSA	2	1
Fold-over Suppression Oversampling	100	N/A
Sense	2	2
Halfscan	0.609	0.609
Fast Imaging Mode	EPI	EPI
EPI Factor	79	47
Phase Encode Direction	L then R	L then R
Acquisition Time	52 min 42 sec	8 min 10 sec (Trig)

Table 6.6: DTI acquisition parameters.

The large number of diffusion directions sampled makes additional geometric distortion possible. The rapidly switching fields of the diffusion sequence induce eddy currents in the sample, which in turn induce an opposing magnetic field. This leads to off-resonance distortions in the image. To combat this FSLs “eddy” can be used [35]. This tool was developed with the brain data from the Human Connectome Project in mind however [36], here it is successfully used to reduce geometric distortions in ex-vivo and in-vivo DTI data and subject motion in the in-vivo data. The tools performance is optimal when b-vectors are distributed over a full sphere as this results in approximately opposing eddy current distortions and as such, makes estimation of the deformation more accurate.

Once the raw data has been processed with topup and eddy, quantitative maps can be generated. Eigenvalues ( $\lambda_1, \lambda_2, \lambda_3$ ) and eigenvectors ( $\epsilon_1, \epsilon_2, \epsilon_3$ ) are calculated for each diffusion tensor,  $\mathcal{D}$ . FA maps can be calculated from equation (6.6). Here it can be seen that if  $\lambda_1 = \lambda_2 = \lambda_3$ , as is the case

## 6.2. MRI Protocol Development

---

for isotropic diffusion, FA tends to 0. An example renal FA map is shown in Figure 6.16a where bright areas represent areas of higher FA and therefore more anisotropic diffusion.

$$FA = \sqrt{\frac{(\lambda_1 - \lambda_2)^2 + (\lambda_2 - \lambda_3)^2 + (\lambda_1 - \lambda_3)^2}{2(\lambda_1^2 + \lambda_2^2 + \lambda_3^2)}} \quad (6.6)$$

FA can also be used to create fibre direction maps as shown in Figure 6.16b. Here the colour is determined by the direction of the principal eigenvector,  $\epsilon_1$ , the primary direction of diffusion, and the brightness is modulated by FA. As the name suggests, these maps provide a visual indication as to the direction diffusion is occurring in a tissue and how strongly it is constrained to that single direction.

The final voxel based map produced using the DTI data is an ADC map, often called Mean Diffusivity (MD) in DTI literature. This is calculated using equation (6.7) and an example is shown in Figure 6.16c. All three of these voxel based maps are generated using FSL.

$$MD = \frac{(\lambda_1 + \lambda_2 + \lambda_3)}{3} \quad (6.7)$$

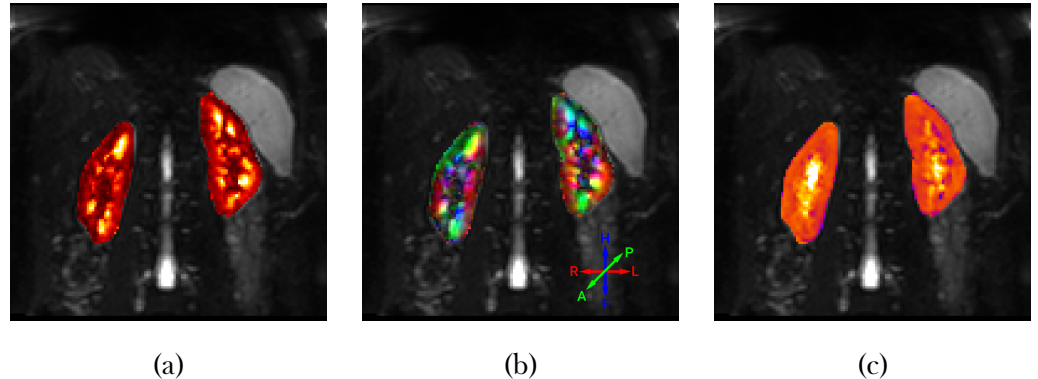


Figure 6.16: FA (a), fibre direction (b) and MD (c) maps generated from the same in-vivo DTI data.

## 6.2. MRI Protocol Development

---

An extension of the fibre direction map is tractography, a technique that can remove the simplification that a voxel has a single direction of diffusion. Even at the highest resolutions achievable with MRI, the biological structures dictating diffusion are orders of magnitude smaller than the resolving power of MRI and as such multiple mechanisms can occur in a single voxel e.g. crossing of neurons or microvascular. In the brain this technique is used to visualise nerve tracts and connectivity within the brain; in the kidneys it can be used to visualise the coherent motion of renal processes. Tractography calculations are performed using the open-source python package Dipy [37] and the resulting tracts were visualised using TrackVis [38].

To model multiple fibres entering and exiting a voxel, a more sophisticated model than simply looking at the principle eigenvector is required. This takes the form of an Orientation Distribution Function (ODF) which can be thought of as the probability a fibre will enter or exit a voxel through a specific solid angle. ODFs can be visualised as isosurfaces where the surface represent all points of equal probability, example ODFs are shown in Figure 6.17. Techniques such as Q-ball imaging [39, 40] and diffusion spectrum imaging [39] can be used to estimate the ODF however these methods tend to require high b-values and as such a lower SNR acquisition making them less suitable to abdominal imaging. Instead a constrained spherical deconvolution method is used [41–43].

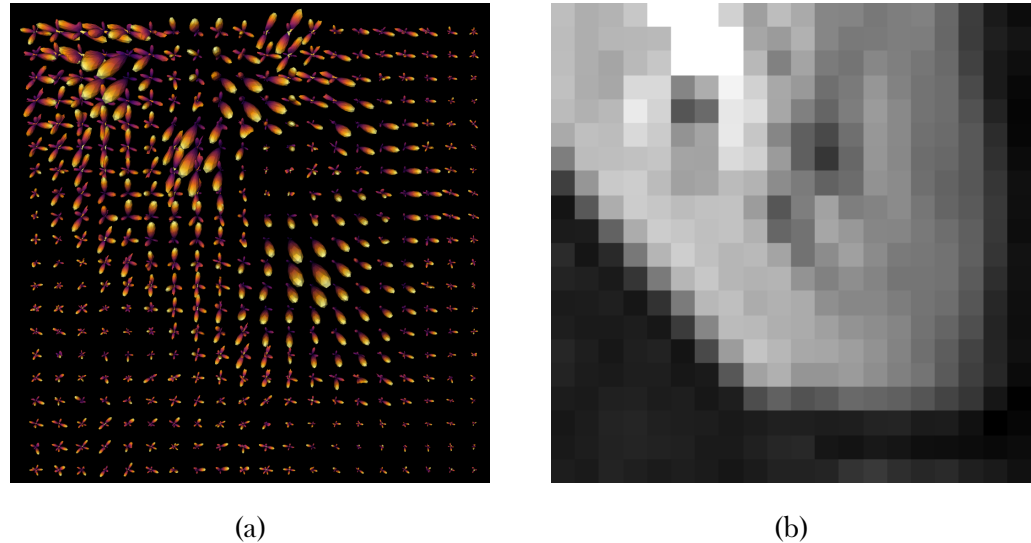


Figure 6.17: The ODFs for a small number of voxels of renal tissue (a) and the corresponding b0 image to help visualise the part of the kidney the data is coming from (b).

The peak values of ODFs are calculated and used to generate streamlines which represent the tracts of coherent diffusion. The calculation of streamline paths is performed using the Euler Delta Crossings (EuDX) method [44]. This tractography pipeline and its many hyper-parameters are best summarised in code form and as such are included in Appendix A. The results of this processing pipeline are tractograms as shown in Figure 6.18.

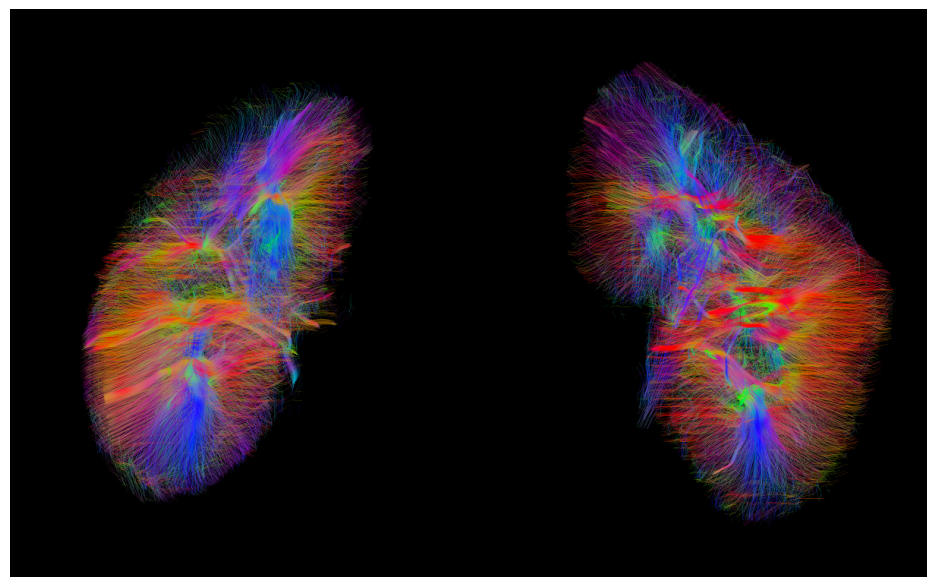


Figure 6.18: Example tractography generated using the above protocol.

## 6.2. MRI Protocol Development

---

As this tractography protocol was developed from scratch, both acquisition and the post processing pipeline were verified in the brain. Tractography is a far more mature technique in neuroimaging and as such, verification that the pipeline produces reasonable results on a more familiar anatomy lends confidence to the tractograms produced of the kidneys. The FOV of the acquisition was adjusted to cover the whole brain but all other parameters were kept constant. The resulting maps and tractogram were all as expected, an example tractogram of the brain produced using this pipeline is shown in Figure 6.19.

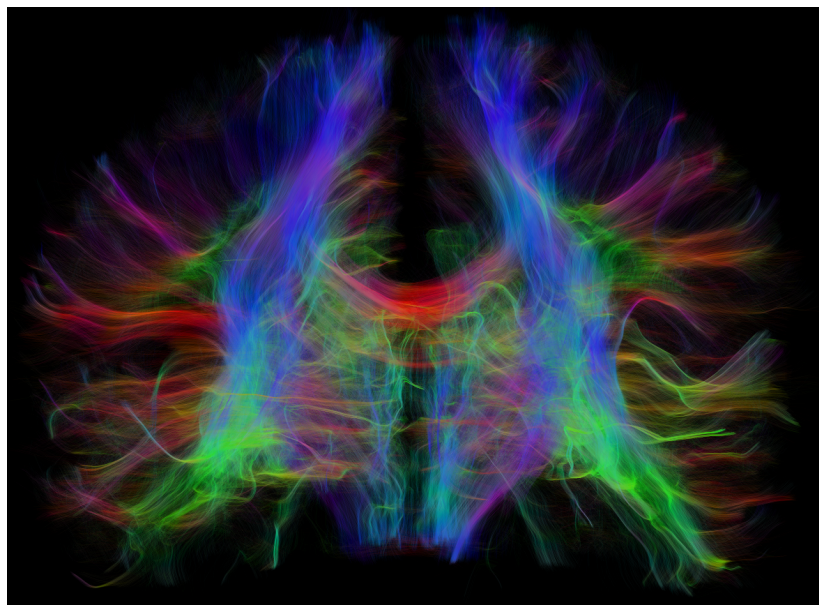


Figure 6.19: A tractogram of the brain produced to verify the DTI acquisition and post-processing scheme developed for the kidneys produces expected results within a structure more commonly the subject of tractography.

Renal in-vivo results were compared to those in literature and found to be in agreement [45–47]. Additionally, renal features with a known structure can be observed in the tractograms such as the radial structure of the medullary pyramids, Figure 6.20.

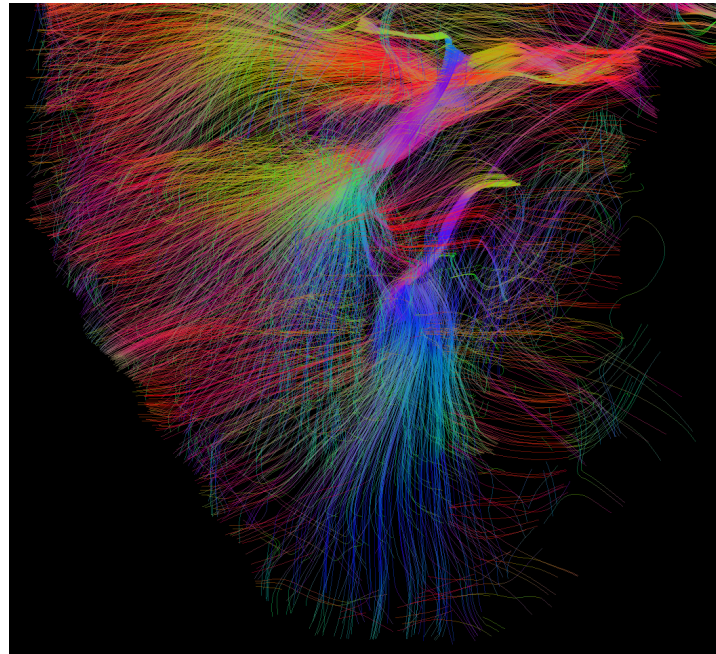


Figure 6.20: The medullary pyramids observed in tractography.

An area that still needs further development is the ex-vivo DTI protocol. There are promising early results however ex-vivo diffusion imaging poses additional difficulties. During the fixation process, methyl bridges cross link with proteins within the tissue stiffening it and causing a small amount of shrinkage [48]. This combined with the lower temperatures of ex-vivo samples ( $\sim 20^{\circ}\text{C}$  room temperature rather than  $\sim 37^{\circ}\text{C}$  body temperature) leads to a reduced degree of diffusion, seen in Figure 6.14. While this results in a higher SNR of diffusion sensitised volumes for a given b-value, the underlying diffusion signal being measured is much smaller i.e. there is less of a difference between  $b_0$  and  $b-600 \text{ sec/mm}^2$  and thus the accuracy of the quantitative maps, Figure 6.21, and tractography, Figure 6.22 is reduced.

## 6.2. MRI Protocol Development

---

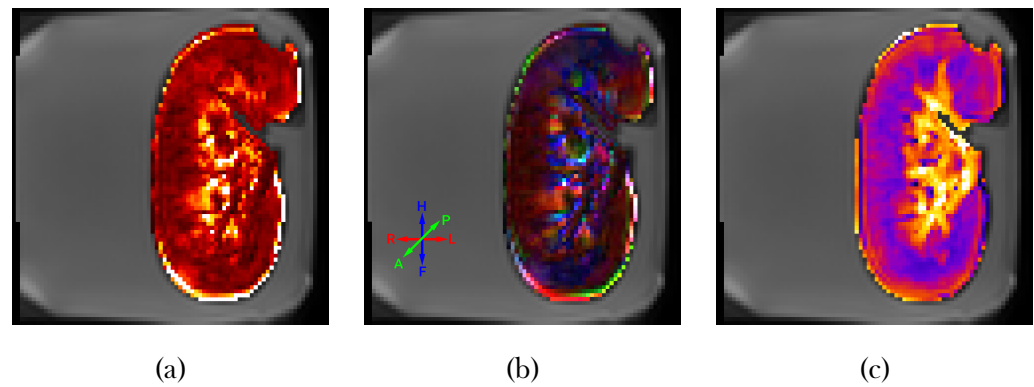


Figure 6.21: FA (a), fibre direction (b) and MD (c) maps of an ex-vivo sample.

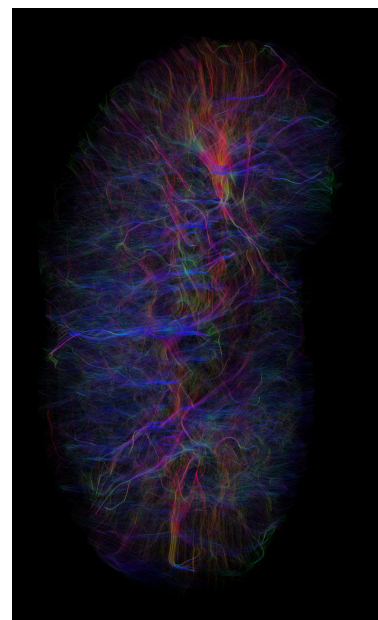


Figure 6.22: Tractography of an ex-vivo kidney sample.

### 6.3 Monitoring Changes in MR Parameters Post Fixation

As outlined already, fixation is a necessity step to ensure a consistent protocol and minimise logistical hurdles in having scanners available at specific times when, by the nature of ex-vivo samples, the acquisition process can be somewhat flexible in timings. The effects of fixation on brain tissue have already been reported [49–51] however no literature on the effects of fixation of renal tissue is available. Here we characterise the stability of  $T_1$  and  $T_2^*$  in renal tissue post fixation to ascertain how stringent the timings of the ex-vivo protocol need to be.

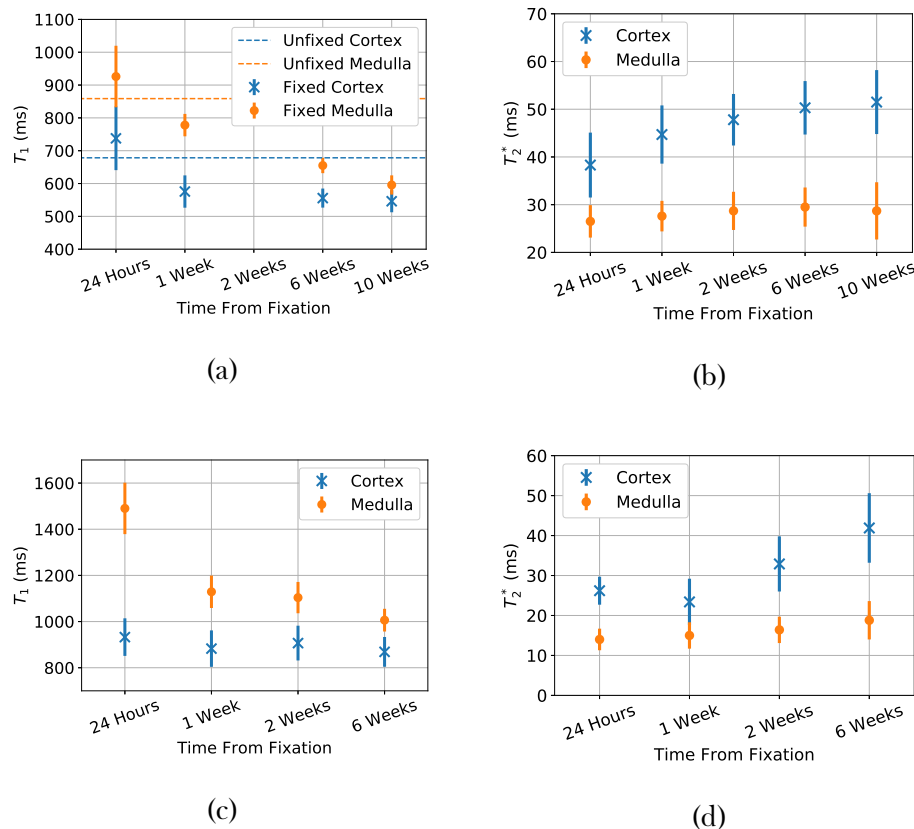


Figure 6.23: (a) Variation in  $T_1$  as a function of time after fixation measured at 3T (b) Variation in  $T_2^*$  as a function of time after fixation measured at 3T (c) Variation in  $T_1$  as a function of time after fixation measured at 7T (d) Variation in  $T_2^*$  as a function of time after fixation measured at 7T.

### 6.3. Monitoring Changes in MR Parameters Post Fixation

---

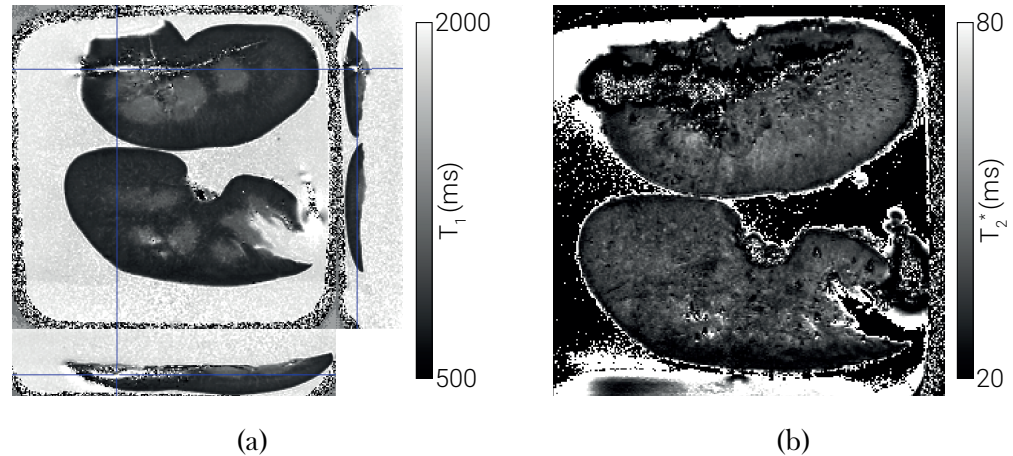


Figure 6.24: (a) An example of the  $T_1$  map collected from the short time scale kidney (b) An example of the  $T_2^*$  map collected from the short time scale kidney.

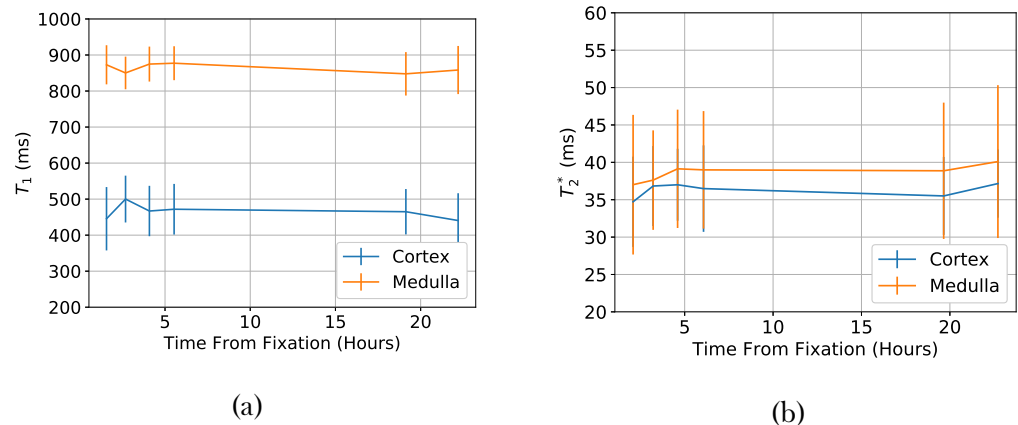


Figure 6.25: (a) Variation in  $T_1$  as a function of time after fixation measured at 3T (b) Variation in  $T_2^*$  as a function of time after fixation measured at 3T.

#### 6.4. Layer Based Analysis of Renal Data

---

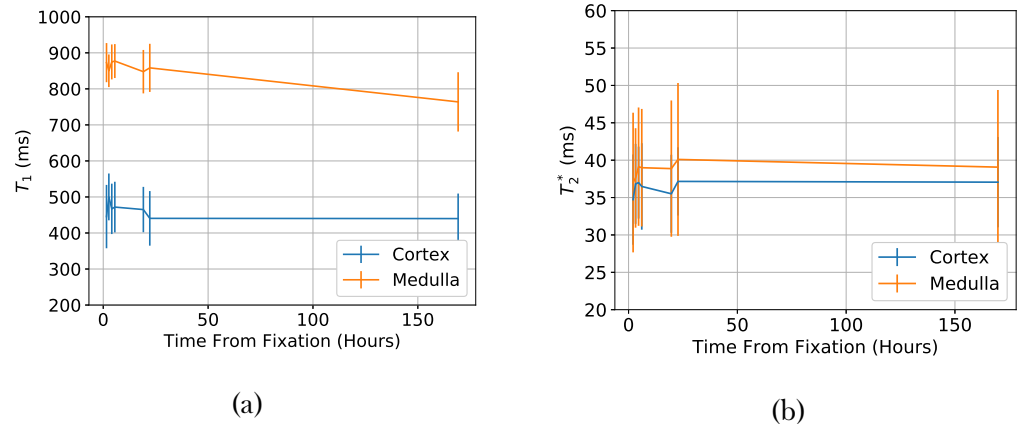


Figure 6.26: (a) Variation in  $T_1$  as a function of time after fixation measured at 3T (b) Variation in  $T_2^*$  as a function of time after fixation measured at 3T.

## 6.4 Layer Based Analysis of Renal Data

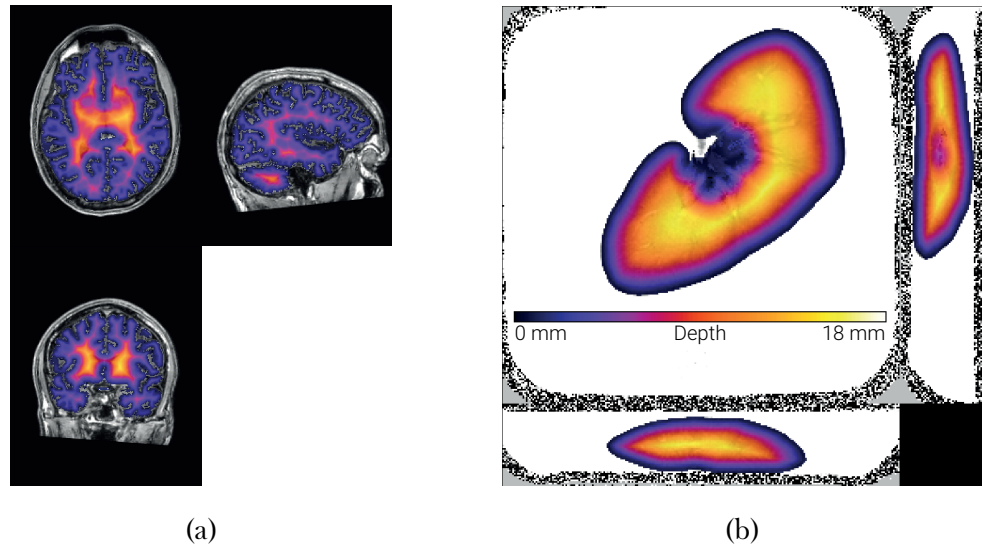


Figure 6.27: (a) A depth mask of the brain. Lighter areas are deeper inside the brain. (b) A depth mask applied to a quantitative  $T_1$  map.

## 6.5 Correlating MRI Measures with Histopathology in Aged Kidneys

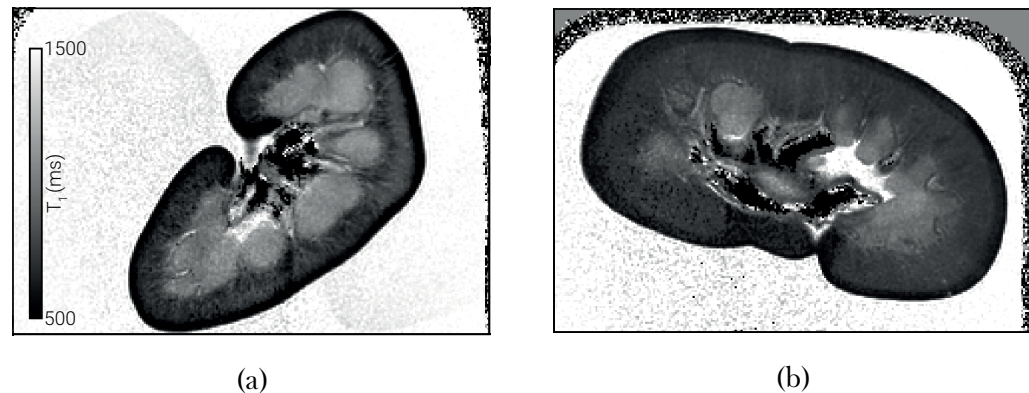


Figure 6.28: (a)  $T_1$  map of a 0.5 year old pig kidney. (b)  $T_1$  map of a 2.5 year old pg kidney.

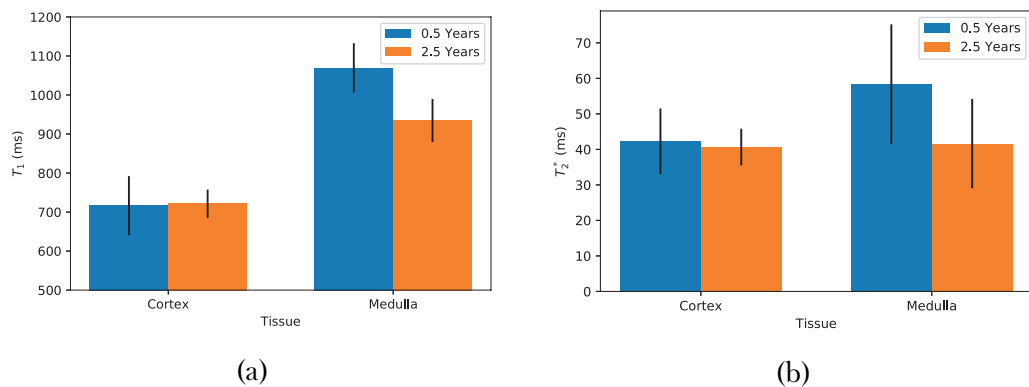


Figure 6.29: (a) The  $T_1$  of the renal cortex and medulla of the two samples.  
(b) The  $T_2^*$  of the renal cortex and medulla of the two samples.

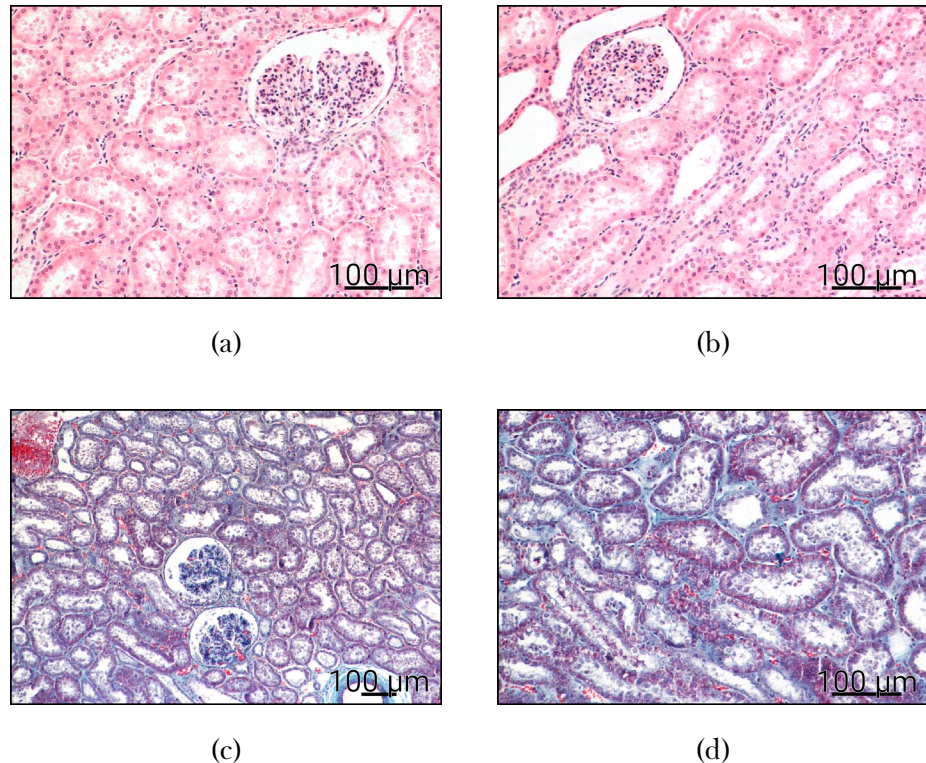


Figure 6.30: (a) A sample of renal cortex from a 0.5 year old pig stained with Haematoxylin and Eosin (H and E). (b) A sample of renal cortex from a 2.5 year old pig stained with H and E. (c) A sample of renal cortex from a 0.5 year old pig stained with Masson's trichrome. (d) A sample of renal cortex from a 2.5 year old pig stained with Masson's trichrome.

## 6.6 Conclusion

## 6.7 Acknowledgements

We are grateful for access to the University of Nottingham's Augusta high performance computing service. We also thank Prof David Gardner of University of Nottingham Veterinary Science for his assistance with sample acquisition, histopathological processing of samples and general renal physiology expertise.

## 6.8 References

1. Daniel, A. J., Buchanan, C., Kazmi, I., Cox, E., Selby, N., Gardner, D. & Francis, S. *The Effects of Fixation and Age on Relaxometry Measurements of Ex-Vivo Kidneys* in *Proc. Intl. Soc. Mag. Reson. Med.* 27 International Society of Magnetic Resonance in Medicine Annual Meeting (Montreal, 13th May 2019).
2. Kazmi, I., Daniel, A. J., Buchanan, C., Francis, S., Taal, M. & Selby, N. *Determining Optimal Technique for Tissue Fixation for Ex-Vivo MRI Imaging of Porcine Kidneys* in. United Kingdom Kidney Week (Brighton, 6th May 2019).
3. Nery, F., Daniel, A. J., Sousa, J. & Buchanan, C. *UKRIN Kidney Analysis Toolbox* version v0.1.0. UK Renal Imaging Network, Dec. 2020.
4. Daniel, A. J. et al. *UKRIN Kidney Analysis Toolbox (UKAT): A Framework for Harmonized Quantitative Renal MRI Analysis* in *Proc. Intl. Soc. Mag. Reson. Med.* 28 International Society of Magnetic Resonance in Medicine Annual Meeting. **29** (Online, May 2021), 2379.
5. Rathod, K. R., Popat, B. A., Pandey, A., Jamale, T. E., Hase, N. K. & Deshmukh, H. L. Safety and Effectiveness of Transjugular Renal Biopsy: A Single Center Study. *Indian Journal of Nephrology* **27**, 118–123 (2017).
6. Mal, F., Meyrier, A., Callard, P., Altman, J. J., Kleinknecht, D., Beaugrand, M. & Ferrier, J. P. Transjugular Renal Biopsy. *Lancet (London, England)* **335**, 1512–1513 (23rd June 1990).
7. Leung, G., Kirpalani, A., Szeto, S. G., Deeb, M., Foltz, W., Simmons, C. A. & Yuen, D. A. Could MRI Be Used To Image Kidney Fibrosis? A Review of Recent Advances and Remaining Barriers. *Clinical Journal of the American Society of Nephrology* **12**, 1019–1028 (7th June 2017).
8. Inoue, T. et al. Noninvasive Evaluation of Kidney Hypoxia and Fibrosis Using Magnetic Resonance Imaging. *Journal of the American Society of Nephrology: JASN* **22**, 1429–1434 (Aug. 2011).
9. Zhao, J., Wang, Z. J., Liu, M., Zhu, J., Zhang, X., Zhang, T., Li, S. & Li, Y. Assessment of Renal Fibrosis in Chronic Kidney Disease Us-

## 6.8. References

---

- ing Diffusion-Weighted MRI. *Clinical Radiology* **69**, 1117–1122 (Nov. 2014).
10. Feng, Q., Ma, Z., Wu, J. & Fang, W. DTI for the Assessment of Disease Stage in Patients with Glomerulonephritis - Correlation with Renal Histology. *European Radiology* **25**, 92–98 (1st Jan. 2015).
  11. Friedli, I. *et al.* New Magnetic Resonance Imaging Index for Renal Fibrosis Assessment: A Comparison between Diffusion-Weighted Imaging and T1 Mapping with Histological Validation. *Scientific Reports* **6**. doi:10.1038/srep30088. pmid: 27439482 (21st July 2016).
  12. Berchtold, L. *et al.* Validation of the Corticomedullary Difference in Magnetic Resonance Imaging-Derived Apparent Diffusion Coefficient for Kidney Fibrosis Detection: A Cross-Sectional Study. *Nephrology Dialysis Transplantation* **35**, 937–945 (1st June 2020).
  13. Jafari, R., Hectors, S. J., González, A. K. K. de, Spincemaille, P., Prince, M. R., Brittenham, G. M. & Wang, Y. Integrated Quantitative Susceptibility and R2\* Mapping for Evaluation of Liver Fibrosis: An Ex Vivo Feasibility Study. *NMR in Biomedicine* **34**, e4412 (2021).
  14. Sabouri, S., Fazli, L., Chang, S. D., Savdie, R., Jones, E. C., Goldenberg, S. L., Black, P. C. & Kozlowski, P. MR Measurement of Luminal Water in Prostate Gland: Quantitative Correlation between MRI and Histology. *Journal of Magnetic Resonance Imaging* **46**, 861–869 (2017).
  15. Dhatt, R. *et al.* MRI of the Prostate With and Without Endorectal Coil at 3 T: Correlation With Whole-Mount Histopathologic Gleason Score. *American Journal of Roentgenology* **215**, 133–141 (11th Mar. 2020).
  16. Uribe, C. F., Jones, E. C., Chang, S. D., Goldenberg, S. L., Reinsberg, S. A. & Kozlowski, P. In Vivo 3 T and Ex Vivo 7 T Diffusion Tensor Imaging of Prostate Cancer: Correlation with Histology. *Magnetic Resonance Imaging* **33**, 577–583 (1st June 2015).
  17. Lazari, A. & Lipp, I. Can MRI Measure Myelin? Systematic Review, Qualitative Assessment, and Meta-Analysis of Studies Validating Microstructural Imaging with Myelin Histology. *NeuroImage* **230**, 117744 (15th Apr. 2021).

## 6.8. References

---

18. Peters, J. M. *et al.* White Matter Mean Diffusivity Correlates with Myelination in Tuberous Sclerosis Complex. *Annals of Clinical and Translational Neurology* **6**, 1178–1190 (2019).
19. Moll, N. M. *et al.* Multiple Sclerosis Normal-Appearing White Matter: Pathology–Imaging Correlations. *Annals of Neurology* **70**, 764–773 (2011).
20. Howard, A. F., Mollink, J., Kleinnijenhuis, M., Pallebage-Gamarallage, M., Bastiani, M., Cottaar, M., Miller, K. L. & Jbabdi, S. Joint Modelling of Diffusion MRI and Microscopy. *NeuroImage* **201**, 116014 (1st Nov. 2019).
21. Mollink, J. *et al.* White Matter Changes in the Perforant Path Area in Patients with Amyotrophic Lateral Sclerosis. *Neuropathology and Applied Neurobiology* **45**, 570–585 (2019).
22. Mottershead, J. P. *et al.* High Field MRI Correlates of Myelincontent and Axonal Density in Multiple Sclerosis. *Journal of Neurology* **250**, 1293–1301 (1st Nov. 2003).
23. Seewann, A. *et al.* Diffusely Abnormal White Matter in Chronic Multiple Sclerosis: Imaging and Histopathologic Analysis. *Archives of Neurology* **66**, 601–609 (1st May 2009).
24. Hametner, S. *et al.* The Influence of Brain Iron and Myelin on Magnetic Susceptibility and Effective Transverse Relaxation - A Biochemical and Histological Validation Study. *NeuroImage* **179**, 117–133 (1st Oct. 2018).
25. Stüber, C. *et al.* Myelin and Iron Concentration in the Human Brain: A Quantitative Study of MRI Contrast. *NeuroImage* **93**, 95–106 (1st June 2014).
26. Bagnato, F. *et al.* Untangling the R2\* Contrast in Multiple Sclerosis: A Combined MRI-Histology Study at 7.0 Tesla. *PLOS ONE* **13**, e0193839 (21st Mar. 2018).
27. Reeves, C. *et al.* Combined Ex Vivo 9.4T MRI and Quantitative Histopathological Study in Normal and Pathological Neocortical Resections in Focal Epilepsy. *Brain Pathology* **26**, 319–333 (2016).

## 6.8. References

---

28. Huszar, I. N. *et al.* Tensor Image Registration Library: Automated Non-Linear Registration of Sparsely Sampled Histological Specimens to Post-Mortem MRI of the Whole Human Brain. *bioRxiv*, 849570 (26th Nov. 2019).
29. Huszar, I. N. *et al.* Automated Slice-to-Volume Registration between Histology and Whole-Brain Post-Mortem MRI in *Proc. Intl. Soc. Mag. Reson. Med.* 27 International Society of Magnetic Resonance in Medicine Annual Meeting (Montreal, 16th May 2019).
30. Szumowski, J., Durkan, M. G., Foss, E. W., Brown, D. S., Schwarz, E. & Crawford, D. C. Signal Polarity Restoration in a 3D Inversion Recovery Sequence Used with Delayed Gadolinium-Enhanced Magnetic Resonance Imaging of Cartilage (dGEMRIC). *Journal of Magnetic Resonance Imaging* **36**, 1248–1255 (1st Nov. 2012).
31. Branch, M., Coleman, T. & Li, Y. A Subspace, Interior, and Conjugate Gradient Method for Large-Scale Bound-Constrained Minimization Problems. *SIAM Journal on Scientific Computing* **21**, 1–23 (1st Jan. 1999).
32. Bjarnason, T. A. & Mitchell, J. R. AnalyzeNNLS: Magnetic Resonance Multiexponential Decay Image Analysis. *Journal of Magnetic Resonance* **206**, 200–204 (1st Oct. 2010).
33. Andersson, J. L. R., Skare, S. & Ashburner, J. How to Correct Susceptibility Distortions in Spin-Echo Echo-Planar Images: Application to Diffusion Tensor Imaging. *NeuroImage* **20**, 870–888 (1st Oct. 2003).
34. Le Bihan, D., Breton, E., Lallemand, D., Aubin, M. L., Vignaud, J. & Laval-Jeantet, M. Separation of Diffusion and Perfusion in Intravoxel Incoherent Motion MR Imaging. *Radiology* **168**, 497–505 (1st Aug. 1988).
35. Andersson, J. L. R. & Sotiroopoulos, S. N. An Integrated Approach to Correction for Off-Resonance Effects and Subject Movement in Diffusion MR Imaging. *NeuroImage* **125**, 1063–1078 (15th Jan. 2016).
36. Andersson, J. L. R. & Sotiroopoulos, S. N. Non-Parametric Representation and Prediction of Single- and Multi-Shell Diffusion-Weighted

## 6.8. References

---

- MRI Data Using Gaussian Processes. *NeuroImage* **122**, 166–176 (15th Nov. 2015).
37. Garyfallidis, E., Brett, M., Amirbekian, B., Rokem, A., Van Der Walt, S., Descoteaux, M. & Nimmo-Smith, I. Dipy, a Library for the Analysis of Diffusion MRI Data. *Frontiers in Neuroinformatics* **8**. doi:10 . 3389 / fninf . 2014 . 00008 (2014).
  38. Wang, R., Benner, T., Sorensen, A. G. & Wedeen, V. J. *Diffusion Toolkit: A Software Package for Diffusion Imaging Data Processing and Tractography* in *Proc. Intl. Soc. Mag. Reson. Med.* 15 International Society of Magnetic Resonance in Medicine Annual Meeting (Aug. 2007), 3720.
  39. Descoteaux, M., Angelino, E., Fitzgibbons, S. & Deriche, R. Regularized, Fast, and Robust Analytical Q-Ball Imaging. *Magnetic Resonance in Medicine* **58**, 497–510 (2007).
  40. Hess, C. P., Mukherjee, P., Han, E. T., Xu, D. & Vigneron, D. B. Q-Ball Reconstruction of Multimodal Fiber Orientations Using the Spherical Harmonic Basis. *Magnetic Resonance in Medicine* **56**, 104–117 (2006).
  41. Tournier, J. -D., Calamante, F., Gadian, D. G. & Connelly, A. Direct Estimation of the Fiber Orientation Density Function from Diffusion-Weighted MRI Data Using Spherical Deconvolution. *NeuroImage* **23**, 1176–1185 (1st Nov. 2004).
  42. Tournier, J.-D., Calamante, F. & Connelly, A. Robust Determination of the Fibre Orientation Distribution in Diffusion MRI: Non-Negativity Constrained Super-Resolved Spherical Deconvolution. *NeuroImage* **35**, 1459–1472 (1st May 2007).
  43. Tax, C. M. W., Jeurissen, B., Vos, S. B., Viergever, M. A. & Leemans, A. Recursive Calibration of the Fiber Response Function for Spherical Deconvolution of Diffusion MRI Data. *NeuroImage* **86**, 67–80 (1st Feb. 2014).
  44. Garyfallidis, E. *Towards an Accurate Brain Tractography* Ph.D. (University of Cambridge, 2013).
  45. Gürses, B., Kılıçkesmez, O., Taşdelen, N., Firat, Z. & Gürmen, N. Diffusion Tensor Imaging of the Kidney at 3 Tesla MRI: Normative Values

## 6.8. References

---

- and Repeatability of Measurements in Healthy Volunteers. *Diagnostic and Interventional Radiology (Ankara, Turkey)* **17**, 317–322 (Dec. 2011).
46. Jaimes, C., Darge, K., Khrichenko, D., Carson, R. H. & Berman, J. I. Diffusion Tensor Imaging and Tractography of the Kidney in Children: Feasibility and Preliminary Experience. *Pediatric Radiology* **44**, 30–41 (1st Jan. 2014).
  47. Notohamiprodjo, M., Dietrich, O., Horger, W., Horng, A., Helck, A. D., Herrmann, K. A., Reiser, M. F. & Glaser, C. Diffusion Tensor Imaging (DTI) of the Kidney at 3 Tesla—Feasibility, Protocol Evaluation and Comparison to 1.5 Tesla. *Investigative Radiology* **45**, 245 (May 2010).
  48. Thavarajah, R., Mudimbaimannar, V. K., Elizabeth, J., Rao, U. K. & Ranganathan, K. Chemical and Physical Basics of Routine Formaldehyde Fixation. *Journal of Oral and Maxillofacial Pathology : JOMFP* **16**, 400–405 (2012).
  49. Birkl, C., Langkammer, C., Golob-Schwarzl, N., Leoni, M., Haybaeck, J., Goessler, W., Fazekas, F. & Ropele, S. Effects of Formalin Fixation and Temperature on MR Relaxation Times in the Human Brain. *NMR in Biomedicine* **29**, 458–465 (1st Apr. 2016).
  50. Schmierer, K. et al. Quantitative Magnetic Resonance of Postmortem Multiple Sclerosis Brain before and after Fixation. *Magnetic Resonance in Medicine* **59**, 268–277 (1st Feb. 2008).
  51. Shatil, A. S., Uddin, M. N., Matsuda, K. M. & Figley, C. R. Quantitative Ex Vivo MRI Changes Due to Progressive Formalin Fixation in Whole Human Brain Specimens: Longitudinal Characterization of Diffusion, Relaxometry, and Myelin Water Fraction Measurements at 3T. *Frontiers in Medicine* **5**. doi:10.3389/fmed.2018.00031 (2018).

# **Chapter 7**

## **Conclusion**

Science happened

# Appendix A

## Tractography Pipeline

```
1 import numpy as np
2 import nibabel as nib
3 from dipy.tracking.eudx import EuDX
4 from dipy.tracking import utils
5 from dipy.tracking.streamline import Streamlines
6 from dipy.reconst import peaks
7 from dipy.reconst.csdeconv import \
8     ConstrainedSphericalDeconvModel, recursive_response
9 from dipy.core.gradients import gradient_table_from_bvals_bvecs
10 from dipy.io.streamline import save_trk
11
12 if __name__ == '__main__':
13     print('Ingesting Data')
14     img = nib.load('data.nii.gz')
15     mask = nib.load('mask.nii.gz')
16     bvals = np.loadtxt('bvals')
17     bvecs = np.loadtxt('bvecs')
18     data = img.get_fdata()
19
20     mask_data = mask.get_fdata()
21     mask_data = (mask_data>0)
22
23     gtab = gradient_table_from_bvals_bvecs(bvals.T, bvecs.T)
24
25     print('Estimating Fibre Response Function')
```

---

```
26     response = recursive_response(gtab, data,
27                                     mask=mask_data, sh_order=8,
28                                     peak_thr=0.01, init_fa=0.08,
29                                     init_trace=0.0021, iter=8,
30                                     convergence=0.001, parallel=False)
31
32     print('Generating CSD Model')
33     csd_model = ConstrainedSphericalDeconvModel(gtab, response,
34                                                   sh_order=6)
35
36     print('Getting Peaks From Model')
37     csd_peaks = peaks.peaks_from_model(model=csd_model,
38                                         data=data,
39                                         sphere=peaks.default_sphere,
40                                         relative_peak_threshold=.8,
41                                         min_separation_angle=45,
42                                         mask=mask_data)
43
44     print('Generating Seeds')
45     seeds = utils.seeds_from_mask(mask_data, density=1)
46
47     print('Propogating From Seeds')
48     streamline_gen = EuDX(csd_peaks.peak_values,
49                            csd_peaks.peak_indices,
50                            odf_vertices=peaks.default_sphere.vertices,
51                            a_low=.05, step_sz=.5, seeds=seeds)
52
53     print('Generating Streamlines')
54     streamlines = Streamlines(streamline_gen, buffer_size=512)
55
56     print('Saving Output For Your Perusal')
57     save_trk('tracts.trk', streamlines,
58               shape=mask.shape, vox_size=data.header.get_zooms(),
59               affine=data.affine)
```